LIGHT HARVESTING AND ENERGY EFFICIENCY IN PEROVSKITE SOLAR CELLS AND THEIR APPLICATIONS

Guillermo MARTÍNEZ-DENEGRI SÁNCHEZ

ICFO – Institut de Ciències Fotòniques

UPC – Universitat Politècnica de Catalunya

Barcelona, 2021

LIGHT HARVESTING AND ENERGY EFFICIENCY IN PEROVSKITE SOLAR CELLS AND THEIR APPLICATIONS

Guillermo MARTÍNEZ-DENEGRI SÁNCHEZ

Under the supervision of

Prof. Jordi MARTORELL

submitted this thesis in partial fulfilment

of the requirements for the degree of

DOCTOR

by the

UNIVERSITAT POLITÈCNICA DE CATALUNYA

BARCELONA, 2021

To my beloved family and friends

Agradecimientos

Hace ya más de cinco años, se me presentó la oportunidad de hacer un doctorado en ICFO, concretamente en el grupo de Jordi Martorell. Siempre había sido algo que esperaba poder hacer, pero no estaba seguro si llegaría a lograrlo. Por ello, primero quiero agradecer a mis padres por su esfuerzo para poder proporcionarme la oportunidad de formarme en diferentes instituciones lejos de casa, y a Jordi, por acogerme en su grupo, ya que en su conjunto son quienes lo han hecho posible.

También estoy muy agradecido a mis compañeros de grupo, en especial a Silvia Colodrero, quien fue mi maestra mano a mano, siempre a mi disposición y con quien empecé a "pipetear" a pesar de mi pulso. Ella me enseñó mucho de lo que no sabía (que no era poco) tanto en el ámbito de laboratorio como a nivel conceptual, y sin ella todo hubiese sido mucho más difícil. Todo esto sin dejar atrás al resto de compañeros con los que he convivido día a día, a los que ya no están, y a los que continúan en el grupo, especialmente a Catarina Ferreira, Mariia Kramarenko y Johann Toudert, así como a Gregory Kozyreff, por sus valiosas aportaciones en mi investigación.

Gracias a ICFO como institución por abrirme las puertas, pero también gracias al resto de equipos que hacen posible que todos los grupos puedan llevar a cabo la labor investigadora. En especial, gracias a Vittoria Finazzi por su continuo soporte y las numerosas conversaciones para tratar de solventar problemas experimentales, así como su paciencia para enseñarme a usar el codiciado "dicer". También, gracias al equipo de mantenimiento por su eficacia

y atención ante cualquier problema y a los diferentes workshops por buscar soluciones que nos permitan amoldar los experimentos a lo que necesitamos en todo momento. También gracias a las personas del equipo de gerencia que me han ayudado con la gestión administrativa durante estos años.

Gracias a Ulrich W. Paetzold, jefe de grupo de investigación en el KIT, por permitirme hacer una estancia con él en momentos tan delicados como los que hemos vivido debido a la pandemia. Gracias a todo su grupo en general y, en concreto, a Paul Fassl, por acogerme haciéndome sentir integrado en todo momento aun habiendo pasado sólo un par de meses con ellos, además de por gestionar los dispositivos necesarios para nuestra colaboración. Con ellos tuve la oportunidad de entender otra manera de trabajar e investigar en grupo.

Por último, gracias al resto de mi familia por el apoyo y el interés que han mostrado en todo momento por saber cómo estaba y cómo iba el desarrollo de mi trabajo. De la misma manera, quiero agradecer a todos mis amigos y amigas, que tanto estando cerca o lejos, aportan cachondeo y felicidad a mi vida, a la vez que actúan como pilar fundamental de apoyo en mi día a día.

List of Publications

Publications related to this thesis

1. *Design and fabrication of an energy efficient broadband polarizing half-cylinder photonic plate incorporating perovskite solar cells for light recycling back into electricity*. G. Martínez-Denegri, C. G. Ferreira, Paul Fassl, M. A. Ruiz-Preciado, J. Toudert, U. W. Paetzold & J. Martorell. In progress.

2. *Light recycling using perovskite solar cells in a half cylinder photonic plate for an energy efficient broadband polarized light emission.* C.G. Ferreira, G. Martínez-Denegri, M. Kramarenko, J. Toudert & J. Martorell. **Advanced Photonics Research**, Accepted. (2021)

3. *Ergodic light propagation in a half-cylinder photonic plate for optimal absorption in perovskite solar cells.* G. Martínez-Denegri, S. Colodrero, Q. Liu, J. Toudert, G. Kozyreff, & J. Martorell. **Advanced Optical Materials**, *7*(10), 1900018. (2019)

4. *All-nanoparticle SnO_2/TiO_2 electron-transporting layers processed at low temperature for efficient thin-film perovskite solar cells*. G. Martínez-Denegri, S. Colodrero, M. Kramarenko, & J. Martorell. **ACS Applied Energy Materials**, 1(10), 5548-5556. (2018).

Other publications

5. *The Perovskite Database Project: Releasing the Power of the Crowd with FAIR Data Management.* J. Jacobson, A. Hultqvist, A. García-Fernández, …, G. Martínez-Denegri, …, E. Unger. Submitted.

6. *Stabilization of the JV characteristic of a perovskite solar cell using an intelligent control loop.* C. R. Bheesayagari, G. Martínez-Denegri, A. Orpella, J. Pons-Nin, S. Bermejo, R. Alcubilla, J. Martorell & M. Domínguez-Pumar. **Electronics**, 10(2), 121. (2021)

7. *Relation between fluorescence quantum yield and open-circuit voltage in complete perovskite solar cells*. M. Kramarenko, C.G. Ferreira, G. Martínez-Denegri, C. Sansierra, J. Toudert, & J. Martorell. **Solar RRL**, 4(4), 1900554. (2020).

8. *Formamidinium incorporation into compact lead iodide for low band gap perovskite solar cells with open-circuit voltage approaching the radiative limit*. H. Zhang, M. Kramarenko, G. Martínez-Denegri, J. Osmond, J. Toudert, & J. Martorell. **ACS Applied Materials & Interfaces**, 11(9), 9083-9092. (2019).

9. *Water splitting of hydrogen chemisorbed in graphene oxide dynamically evolves into a graphane lattice.* L. Ciammaruchi, L. Bellucci, C.G. Castillo, G. Martínez-Denegri, Q. Liu, V. Tozzini, & J. Martorell. **Carbon**, 153, 234-241. (2019).

10. *Inverse optical cavity design for ultrabroadband light absorption beyond the conventional limit in low-bandgap nonfullerene acceptor–based solar cells.* Q. Liu, J. Toudert, T. Li, M. Kramarenko, G. Martínez-Denegri, L. Ciammaruchi, X. Zhang & J. Martorell. **Advanced Energy Materials**, 9(20), 1900463. (2019).

11. *High open-circuit voltage and short-circuit current flexible polymer solar cells using ternary blends and ultrathin Ag-based transparent electrodes.* Q. Liu, J. Toudert, L. Ciammaruchi, G. Martínez-Denegri & J. Martorell. **Journal of Materials Chemistry A**, 5(48), 25476-25484. (2017)

Abstract

The environmental issues associated with the use of conventional fuels necessitates the utilisation of renewable energy sources, as well as the implementation of energy efficient designs, in order to decrease electricity consumption. Photovoltaic (PV) technology can be employed for both approaches by converting not only natural but, also, artificial light into electricity. Among the different emerging PVs, perovskites achieve the highest power conversion efficiency, providing a widely tuneable bandgap with minimum open circuit losses. Moreover, their fabrication uses readily available materials, and does not necessarily require either the use of high temperature processes or vacuum deposition techniques. In this thesis, we enhance light harvesting in perovskite solar cells, and approach the energy efficiency concept through their optimised fabrication and integration in light selective structures. This is accomplished by the implementation of optical and material strategies applied to specific perovskite solar cell designs. The results prove that such strategies provide enhanced light absorption and optimal PV performance in low temperature devices, and enable the recycling of light into electricity for alternative photonic applications. The approaches presented could be utilised in future procedures to decrease the amount of Pb employed in perovskite solar cells, and to reduce the energy consumption during fabrication and the operation of other optoelectronic devices.

The thesis is organised into four chapters. Chapter 1 serves as an introduction, where the current energy situation and PV technology are analysed, together with an insight into light harvesting and energy efficiency in perovskite

solar cells. In Chapter 2, we demonstrate the employment of a periodic structure to propagate ergodic light in order to increase light absorption in perovskite solar cells, as would happen by employing randomly textured surfaces. This structure serves as a tool to decrease the Pb content used in perovskite solar cells, since 30% less material can be used to obtain a solar cell with equal performance. Then, in Chapter 3, the same periodic configuration with a thin film structure deposited on its surface is applied as a waveguide, which is also able to transmit polarised light. Moreover, two perovskite solar cells integrated on the sides recycle the non-transmitted light into electricity, increasing the energy efficiency of the optical process, with further application in liquid crystal displays (LCDs). Finally, in Chapter 4, we demonstrate the suitable application of a nanoparticle bilayer made of one layer of SnO_2 and another of TiO_2 as n-type materials in perovskite solar cells. These types of devices, based on low temperature processes, are proven to perform better than those containing one type of nanoparticles, especially in semi-transparent devices. In such devices we achieved an enhancement in performance of up to 30% for solar cells based on extremely thin active layers.

Resumen

Los problemas medioambientales asociados al uso de combustibles convencionales requieren del uso de fuentes de energía renovables, así como de la implementación de diseños eficientemente energéticos para reducir el consumo de energía. La tecnología fotovoltaica puede emplearse para cubrir ambas estrategias convirtiendo no sólo la luz natural, sino también la artificial, en electricidad. De entre las diferentes tecnologías fotovoltaicas emergentes, las perovskitas alcanzan la más alta eficiencia en conversión de potencia, al mismo tiempo que proporcionan una banda de energía prohibida ampliamente ajustable con pérdidas mínimas de tensión de circuito abierto. Además, su fabricación usa materiales abundantemente disponibles, y no requiere necesariamente de procesos a alta temperatura ni de técnicas de deposición en vacío. En esta tesis, mejoramos la colección de luz en celdas de perovskitas, a la vez que abordamos el concepto de eficiencia energética a través de una fabricación optimizada y su integración en estructuras selectivas de luz. Esto es conseguido gracias a la implementación de estrategias ópticas y materiales aplicadas a diseños específicos de celdas solares de perovskita. Los resultados demuestran que tales estrategias proporcionan una colección de luz y un rendimiento fotovoltaico mayor aplicable a dispositivos fabricados a baja temperatura, y permiten el reciclaje de luz en electricidad para aplicaciones fotónicas alternativas. Las técnicas presentadas podrían ser utilizadas en procedimientos futuros para disminuir la cantidad de Pb empleado en celdas solares de perovskita, y para reducir el consumo de energía durante su fabricación y el funcionamiento de otros dispositivos optoelectrónicos.

La tesis está organizada en cuatro capítulos. El Capítulo 1 sirve como una introducción, donde la actual situación energética y la tecnología fotovoltaica son analizadas junto a una descripción de la recolección de luz y la eficiencia energética en celdas solares de perovskita. En el Capítulo 2, demostramos el uso de una estructura periódica para propagar luz ergódicamente y así aumentar la absorción de luz en las celdas solares de perovskita, de manera equivalente a lo que se obtendría usando superficies aleatoriamente texturizadas. Esta estructura sirve como herramienta para reducir el contenido de Pb empleado en celdas solares de perovskita, ya que se puede utilizar 30% menos de material para obtener una celda solar con un rendimiento equivalente. En el Capítulo 3, la misma configuración periódica con una estructura de capa fina depositada en su superficie es empleada como guía de luz, la cual es, además, capaz de transmitir luz polarizada. Además, dos celdas de perovskita integradas en sus laterales reciclan la luz no transmitida en electricidad, incrementando la eficiencia energética del proceso óptico, lo cual podría tener futura aplicación en pantallas de cristal líquido. Finalmente, en el Capítulo 4, demostramos la aplicación de una bicapa de nanopartículas hecha de una capa de SnO_2 y otra de TiO_2 como materiales de tipo n en celdas solares perovskita. Este tipo de dispositivos, basados en procesos a baja temperatura, funcionan mejor que los que integran un único tipo de nanopartículas, especialmente en dispositivos semitransparentes. En tales dispositivos conseguimos un funcionamiento hasta 30% mejor para celdas solares basadas en capas activas extremadamente finas.

Table of Contents

List of Figures

List of Schemes

List of Tables

List of Abbreviations

$\propto$	Absorption coefficient
$\propto_o$	Angle of incidence with respect to the horizontal axis of the h-CPP
AFM	Atomic force microscopy
AVT	Average transmittance
CDF	Cumulative distribution function
CIGS	CuInGaSe2
E_g	Bandgap energy
EQE	External quantum efficiency
ETL	Electron transport layer
ETM	Electron transport material
FAI	Formamidinium iodide
FF	Fill factor
h-CPP	Half-cylinder photonic plate
HTL	Hole transport layer
ITO	Indium tin oxide
J_{sc}	Short circuit current density
J-V	Current density-voltage
l	Thickness of the material

λ_B	Wavelength in the blue spectrum
λ_G	Wavelength in the green spectrum
λ_R	Wavelength in the red spectrum
LCD	Liquid crystal display
MABr	Methylammonium bromide
n	Refractive index
NIR	Near infrared
PCE	Power conversion efficiency
PDMS	Polydimethylsiloxane
PTAA	poly[bis(4-phenyl)(2,4,6-trimethylphenyl)amine]
PV	Photovoltaic
RGB	Red, green and blue
SEM	Scanning electron microscopy
Spiro-OMeTAD	2,2',7,7'-Tetrakis[N,N-di(4-methoxyphenyl)amino]-9,9'-spirobifluorene
Tp	p-polarised light transmittance
Tp/Ts	polarisation ratio
Ts	s-polarised light transmittance
UV	Ultra-violet
V_{oc}	Open circuit voltage
XRD	X-Ray diffraction

Chapter 1

Introduction

1.1 Situation, concerns and improvements related to the current energy demand

1.1.1 Current situation and issues

The current global demand for energy is growing at a pace that requires appropriate approaches and policies in order to reduce its impact on the environment and our lives. Primary energy consumption has increased 45% in the last 20 years and there is no indication that this trend is going to decrease significantly over the coming decades.[1,2] The principal issue regarding such high levels of consumption is related to the effect on the environment and global climate change, mainly due to the greenhouse gasses emitted. Most of these emissions are linked to the energy source and its transformation into usable energy. For this reason, energy supplies must be efficient, secure and technologically viable, while at the same time contributing to the reduction of emissions and minimising the impact on the environment. In this thesis, the core of the research is based on an emerging PV technology known as perovskite PVs, in which much effort is being invested to fulfil all these requirements, as we will see later in this chapter.

Nevertheless, the solution to the environmental problem cannot only be approached by choosing renewable sources over conventional fuels. Current energy consumption trends have led to an unsustainable world model, whose effects may entail a threat to the planet and lead to future damage for which it may never be possible to compensate. Even if the level of energy consumption is somehow linked to the human development index,[3] this argument must not be used as evidence of being on the correct path regarding our consumption practices. The correlation of both concepts is controversial and, even if real, must not be adopted as a cause and effect relationship in simple terms.[4–6] Therefore, as technology advances and the world relies on it more and more, which implies an increased use of energy, we must guide such technological development towards reducing the negative side effects of larger energy consumption.

1.1.2 Energy efficiency in engineering and technology

In order to reduce the impact of energy consumption, it is important to rely on environmentally friendly sources but, at the same time, to make use of the energy we consume in a responsible manner. In order to do this, we must think of energy as a limited and valuable resource and make an effort to reduce the quantity we consume in our daily lives. Certainly, we are responsible for the amount of energy we use and inappropriately waste, but it is also important to have access to optimised designs in which the energy is correctly managed. For instance, energy efficient buildings have been established as a milestone for living in sustainable developed cities.[7] The energy efficiency of a building is rated depending on its ability to save the most energy required by its residents going about their daily lives within the building.

In this thesis, we differentiate between energy efficiency (understood to be the ability of a system to efficiently exploit the energy invested in such a system)

and the efficiency strictly related to the energy transformation or conversion processes. For instance, in order to create indoor illumination in an energy-efficient manner, one could consider complementing the artificial light source with natural light provided from daylight. The efficiency of the light source itself (luminous power output versus electrical power input) would be seen as a particular parameter, considered to be independent of the whole energy efficiency concept. Both concepts are important in order to reduce the side effects of energy consumption and, throughout this work, we will demonstrate some approaches for using perovskite PVs as a technology for optimised PV energy production and innovative energy efficient designs. In particular, we will cover energy efficiency related to the fabrication process of perovskite solar devices and to their employment of light management in polarisation selective designs with a potential application in display technology.

The concept of energy efficiency not only covers the operation of a system or a technology, but also refers to all the processes involved in making its application and its manufacture possible. Although in many cases fabrication processes might not be considered with regard to energy efficiency, it is, nevertheless, a key aspect. In order to be as energy efficient as possible, fabrication processes cannot be energy intensive. Many industrial manufacturing processes rely on intense energy procedures, which considerably increase the energy cost of production, an example being concrete used in construction. The fabrication of the concrete alone, which requires high processing temperatures, implies a consumption of between 12% and 15% of energy from all industrial activities, and, therefore, much effort is being directed towards processing it in a less energy intensive way.[8,9] In fact, fabrication processes involving high temperature requirements are often linked to manufacturing with the highest energy cost. Unfortunately, in material engineering, high temperatures are often

necessary in order to create materials with the desired characteristics to work effectively within their application, including PV materials. Temperature affects the properties of such materials in many ways, such as morphology, and optical and electronic properties among others, and further research is required to find alternatives so as to avoid the need for critical temperatures.

Energy efficiency related to illumination is a very relevant concept since we find luminous sources everywhere, from artificial indoor and outdoor lighting to all kinds of screens or displays. Specifically, display technology is found in almost all electronic devices and is often responsible for a considerable amount of the energy required by the device. For instance, in smartphones, display illumination can consume up to 75% of the battery usage.[10] The most common display technology is LCD since it is considered to be well-developed and to offer reliability and high resolution in a cost-effective way.[11–14] However, LCD might not always be energy efficient due to certain losses related to light manipulation processes, such as polarisation and spectrum selectivity.[15] In particular, for polarisation selectivity, when absorbing polarisers are employed, the non-transmitted light is absorbed and, therefore, lost in the device, accounting for at least a 50% loss in energy. Over the years, reflective polarisers (which reflect the non-transmitted light instead of absorbing it)[16–20] in combination with different optical management techniques have been applied to reduce such energy losses leading to greater energy efficiency. However, in practice, finding an innovative design able to transmit broadband polarised dispersed light from an unpolarised emitting source, avoiding overall light losses, still remains a challenge.

1.2 Photovoltaic energy

1.2.1 The sun as a source of energy

With the aim of meeting environmental policy demands, it is unarguable that the implementation of renewable energies must be a main contributor in electricity production. There are various different renewable energy sources, mainly derived from different events that occur naturally on our planet. Of these, the sun is by far the most important source, as shown in Figure 1.1. Using the amount of primary energy supplied in 2017 as an example (162,494 TWh),[21] if we were able to capture all of the sun's energy that reaches the Earth in just one year, we would be able to cover global energy demands for 1,240 years. The key aspect when considering solar energy is how to collect the greatest amount of energy and efficiently transform it into electrical energy for distribution, storage or use.

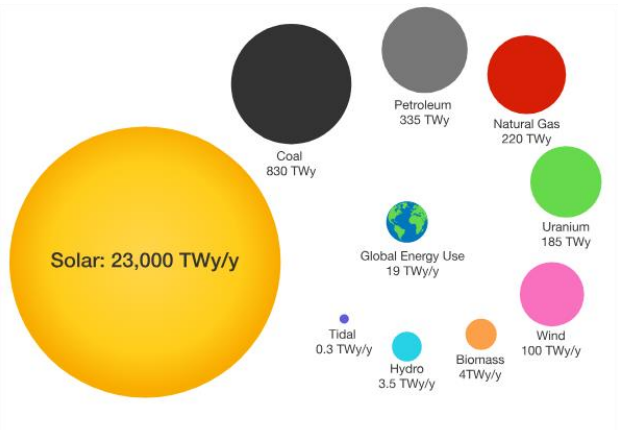

Figure 1.1 Energy sources in terms of availability. For the renewable sources, the number represents the potential energy they are able to offer over the course of one year.[22]

1.2 Photovoltaic energy

There are two main ways to convert solar energy into usable energy. The first utilises the thermal energy directly to provide heat or electrical energy through a thermal cycle. The second, known as PV energy, generates electricity due to the photovoltaic effect that occurs in semiconducting materials, and consists of the direct conversion of photons into electrical carriers. For electricity generation, the advantage of PV over thermal energy is that the former directly provides electricity, and the energy conversion process is more efficient. To apply this type of energy technology, solar cells have been in use for many years being silicon generally used as active material.

Silicon manufacturing technology has been improving over the years, providing reliable solar cells with relatively high efficiency and at accessible prices, that can be adapted to different consumer profiles. Nowadays, it is very common to find these devices not only in solar fields for bulk electricity production, but also for self-powering private residences and mobile homes. Nevertheless, although it is a successful technology, it has some associated drawbacks that may be overcome by finding alternative materials. Silicon is found in the Earth's crust, but rarely as a pure element, and it requires several extraction, purification and doping processes before it is used as a PV material. Also, the manufacturing process needed to fabricate monocrystalline solar cells is based on its growth, and requires temperatures of over 1,400 °C, implying very high fabrication energy costs. Moreover, this type of solar cell requires bulk materials with thicknesses of hundreds of microns, meaning that a considerable amount of Si is needed for a single device.

Over the past few decades, research in the field of PVs has considered new materials and production methods to make solar cell technology more efficient, more versatile and less expensive. Thin film solar cells are of particular interest due to the reduced amount of material that is needed. Unfortunately, when thin

film technology is applied to silicon, efficiency is limited by the absorption coefficient of this material. Alternative inorganic materials such as CdTe and $CuInGaSe_2$ (CIGS), however, have been proved to work better in devices with films that are only a few microns thick, although the availability of the materials involved is much more limited and their fabrication normally involves high temperature annealing. Recently, other organic or organic-inorganic materials, such as perovskites, have been studied. Active layers of only hundreds of nanometres are required, and the research has led to efficient PV devices at low-cost and via simpler and less energy intensive processes.

1.2.2 State-of-the-art perovskite solar cells

Organo-halide perovskites were first discovered as a potential PV material in 2009, when this material was applied as a dye sensitizer in liquid dye sensitized solar cells.[23] Later, it was discovered that photogeneration and free charge transport could occur in these types of crystalline perovskites, meaning that the main photoactive phenomena were taking place in the perovskite itself and not necessarily in the TiO_2 mesoporous layer.[24–27] This led to a rapid increase in research on this type of material, resulting in the latest high efficiency emerging solar cells. Organo-halide perovskite solar cells, combining high absorption and charge generation, large charge diffusion and an easily tuneable bandgap, have been widely studied in order to understand them and make improvements.[28–30] The power conversion efficiency (PCE) of a solar cell is determined by Equation 1.1:

$$PCE = \frac{P_{out}}{P_{in}} = \frac{V_{mpp}\, I_{mpp}}{P_{in}} = \frac{V_{oc}\, J_{sc}\, FF}{P_{in}} \qquad (1.1)$$

where P_{out} refers to the electrical power provided by the solar cell, P_{in} to the incident light power equivalent to 100 mW/cm^2 when a standardised AMG1.5-

sun illumination is considered, V_{oc} to the open circuit voltage, J_{sc} to the short circuit current density and *FF* to the fill factor. Perovskite solar cells are especially efficient due to the limited V_{oc} drop provided by the low recombination losses despite being an organic-inorganic material and the high J_{sc} given by the high external quantum efficiency (EQE), whose relationship is determined by Equation 1.2, as follows:

$$Jsc = q \int \frac{EQE(\lambda)\ \phi(\lambda)\lambda\ d\lambda}{hc} \tag{1.2}$$

where q corresponds to the electron charge, $\Phi(\lambda)$ to the standard AMG1.5 spectral sun irradiance, λ to the light wavelength, c to the velocity of light, and h to Plank's constant.

In solar cell devices, the perovskite active layer is typically sandwiched between two buffer layers, an electron transport layer and a hole transport layer (ETL and HTL, respectively). One of the most general perovskite solar cell classifications is related to whether the device is fabricated by depositing the ETL or the HTL first (n-i-p and p-i-n configuration, respectively). This aspect limits the materials that can be employed since, depending on the process and the solvents (if any) during the deposition of further layers, the first materials may or may not be suitable to be deposited below the other layers. Many different types of perovskite solar cell structures have been developed with the aim of achieving the most efficient and stable devices. Outstanding performances have been observed for both types of configurations,[31–34] but the n-i-p structure has achieved the highest published efficiencies with high stability.[35] Figure 1.2 shows the maximum reported efficiencies for both n-i-p and p-i-n structures from 2009 to 2019.

The strategies for improving the performance of perovskite solar cells range from modifying the perovskite composition and crystallisation,[31,36–38] to the

passivation of the interfaces[39–43] and finding the buffer layers that perform best in the device.[44–50] After little more than a decade since the first perovskite application in the field of PVs, an efficiency of over 25% has been achieved, as published by the NREL, an institution which records the efficiencies of different PV technologies.[51]

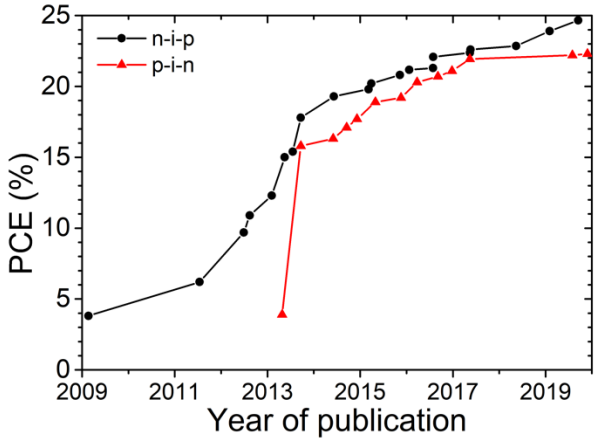

Figure 1.2 Maximum efficiencies for perovskite solar cells for n-i-p and p-i-n structures.

However, efficiency is not the only key parameter for the implementation of this technology. A good solar cell is also determined by its stability, its potential scalability to fabricate working devices in realistic dimensions, and the compatibility of its fabrication processes with today's industrial techniques and environmental standards at a low energy cost.

1.2.3 Challenges with perovskite solar cells

In order to make it worthwhile to produce and commercialise a solar cell, such a cell must be able to give a reliable performance for a sufficient amount of time. When perovskite solar cells were first developed, stability was one of the main issues as their lifetime could be as short as a few seconds.[23] Such stability issues were linked either to the perovskite material ionic bonding in its AXB_3

crystalline structure or to other aspects related to the performance of the device, such as ionic migration to the interfaces, or different phenomena due to environmental interaction (e.g. temperature, oxygen, moisture or irradiation).[52,53] Nowadays, the stability of perovskite solar cells has been improved to such a degree that very low loss of performance occurs under normal working conditions[54,55] and in outdoor environments,[56,57] even after thousands of hours.

In order to achieve rapid progress in the development of this technology and to understand the different physical mechanisms occurring in emerging solar cells, some aspects regarding their fabrication out of a laboratory environment have thus far been ignored. It is important that fabrication processes are always considered in terms of their feasibility for large scale production. Typically, solution-processed perovskite solar cells are fabricated by spin-coating the perovskite precursor, a technique which allows the deposition of the perovskite layer on rather small substrates through easy and rapid techniques. However, to increase the deposited area and, therefore, the size of the solar cell, alternative techniques are currently being studied.[58] Recently, different roll-to-roll processing methods that can be adapted to an industrial chain for large area production have been tested and have achieved very decent efficiencies.[59–64] Non solution-processed techniques may also be used to cover large areas, but these can greatly limit the roll-to-roll mechanism as they normally require some degree of vacuum for their deposition. Thermal evaporation is a technique that has been applied since the early stages of development of perovskite solar cells,[27,65] but the need for a high vacuum and a high deposition temperature considerably limits the ability of the cells to be fabricated in a cost-effective way. In fact, as explained previously, low temperature processes must be employed to make the fabrication of perovskite solar cells more energy efficient.

Energy efficiency is not the only consideration regarding the environmental impact of the fabrication of solar cells. In addition, the solvents and materials employed for their manufacture are of great importance. Although the toxicity of solvents used in fabrication is a relevant issue, more important is the content of Pb in high-efficiency perovskite solar cells, which has led to a central debate since it would be exposed to the open environment. Even if the true risk of Pb within properly fabricated solar cell modules remains unclear, just its leakage into the soil and water would mean a source of contamination that might become a threat to animal and human safety and health.[66,67] At the current time, eliminating Pb as the central atom (X position) in the crystal structure does not seem feasible for comparably efficient and stable perovskite solar cells. So far, alternatives that replace Pb with Sn, Ge and Bi, among others, do not perform as well, and also compromise the cell's stability due to issues related to the material bandgap and crystal lattice distortion, respectively, when these ions are introduced.[68,69] Given the current situation, an intermediate solution is to at least reduce the amount of Pb content in the device. The most straight forward approach to achieving this is to use low Pb formulations in the perovskite layer and/or to reduce the amount of material needed by increasing light absorption through proper optical and photonic management.

1.3 Light propagation applied to thin film solar cells

1.3.1 Light absorption in thin film materials

The absorption coefficient of a material ($\propto$) determines the amount of light that is absorbed as it passes through the material at a given wavelength. In general terms, the relation between the relative absorption, *A*, and $\propto$ is given by Equation

1.3 below, where I_0 and I_1 are the intensities entering and transmitted out of the material, respectively, and l is the thickness of the material.

$$A = 1 - \frac{I_1}{I_0} = 1 - e^{-\propto l} \tag{1.3}$$

Given this relation, the simplest way of increasing absorption would be to increase the thickness of the material. However, this is not always possible, especially in thin film applications, since it might be limited by other thickness-dependent parameters, such as the efficient charge extraction in the case of semiconductors. When the goal is to obtain maximum absorption but there is a particular limitation on the film thickness, enhanced absorption is possible with proper photon management, without the need to alter the absorber thickness. Light trapping techniques are designed to avoid loss of light from a structure by trapping the entering light and eluding its dissipation, but it is important to keep in mind the maximum possibilities in this respect. For this analysis, some fundamental studies regarding the absorption limit for different light trapping approaches have been carried out. In a 1982 seminal work, Yablonovitch established a theoretical absorption limit based on a statistical approach to the ray optics of geometric light trapping structures. The analysis defines the boost of light intensity inside a light trapping structure with ergodic light propagation when it is immersed in a blackbody radiation environment. The study concludes that the absorption enhancement achievable with ray optics trapping structures is $4n^2$, with n being the local refractive index.[70] Further limits have been established for other light trapping mechanisms or more specific schemes, such as grating structures,[71] and plasmonic[72] or planar thin film[73] waveguides. For other conditions that are outside the parameters considered in Yablonovitch's analysis, where wave-optics must be considered, the limit has been overcome, although it provides only a narrowband absorption enhancement.[74,75]

Among the different techniques for trapping light, ergodic light propagation provides a broadband absorption enhancement that is of special interest for such a wide range spectrum of light as sunlight. The geometric effect provided by a randomly textured surface traps light once it is inserted inside the light trapping structure, by considerably reducing the likelihood of the light escaping.[76,77] The chaotic propagation of light in such schemes implies the homogeneous dispersion of the light within the light trapping boundaries. This effect, as well as being especially suitable for increasing light absorption in an absorbing material, can also act as a dispersion mechanism for homogeneous transmittance when it occurs in non-absorbing materials. Examples of both applications will be demonstrated in Chapter 2 and Chapter 3, respectively, by the employment of a geometric periodic structure as an ergodic light propagator.

1.3.2 Light trapping in thin film solar cells

Thin film solar cells are a good example of absorbing devices in which the absorption of the active layer is limited by the film thickness.[78,79] As defined previously in Equations 1.2 and 1.3, the EQE of a solar cell is directly connected to its PCE. The EQE is, basically, the number of electrons generated per number of photons that reach the solar cell. Therefore, the amount of light absorbed is relative to the generation of charge carriers, which directly affects the efficiency of the solar cell. After electron-hole photogeneration, charges need to separate and travel to their corresponding electrode without being recombined. For an efficient charge extraction, the thickness of the active material in a solar cell should not exceed the mean free path of these charges so as to avoid recombination. Given this requirement, in order to enhance light absorption a light trapping technique can be applied as an alternative to thickening the active material layer. Different techniques have been designed to trap light in solar cells,

and, depending on the optical effect that governs the different light trapping techniques, these can be classified into two different groups. Firstly, there are techniques that are ruled by geometric optical effects, such as reflection or refraction, in which the amount of light reflected and the direction of the transmitted light depend on the angle of incidence and the local refractive index of the travelling medium. On the other hand, there are methods based on wave optics, such as interference or plasmonics, in which mainly resonant modes are used to trap the light and enhance its absorption.

As discussed previously, geometric schemes could lead to an ergodic light trapping solution which is of special interest in solar cells due to the broadband light absorption enhancement. Although a theoretical limit in the absorption enhancement of $4n^2$ was established for this type of light trapping, it is only valid in the case of low absorption (for $\propto l << 1$).[70] However, in 4th generation solar cells, such as organic and perovskite devices, this parameter is higher, with values of approximately $\propto l \sim 1$[80,81] and $\propto l \in [1,5]$[82], respectively. Therefore, the absorption enhancement is more limited[83] and, in the case of perovskites, is expected to be in the near infrared (NIR) region.

Interest in enhancing light absorption in solar cells extends beyond finding maximum thickness limitations for optimal performance. In many cases, the approach may also be useful to help minimise the amount of material employed for an equally efficient solar cell. In the case of perovskites, the fact that most efficient solar cells include Pb in their composition is another reason to seek ways to reduce the quantity of active material. The lower the levels of Pb in the solar devices, the lower the potential risk given unexpected Pb leakage from the device, which could help to fulfil possible environmental standards for future perovskite solar cell applications.

1.4 Increasing light harvesting and improving energy efficiency through the application and fabrication of perovskite solar cells

1.4.1 Geometrical optics for light trapping in perovskite solar cells

Among the different techniques for trapping light within a solar cell, textures and geometrical structures that block the escape of light from the cell have been widely studied for the different types of PV materials.[84–90] Since the effectiveness of this approach is based on the geometry and the refractive index contrast at the interface, the technique is of special interest for perovskite since it can be easily applied to function at broadband wavelength ranges. However, the structure must be integrated in such a way as to avoid any consequent undesired side effect that might negatively affect the performance of the device. For instance, texturing or fabricating microstructures within the layers of the device could create certain defects or modify the inherent properties of the material. In order to avoid this, the application of the texture on the back surface of the transparent substrate is a common technique for trapping light while still maintaining the cell's electrical performance.[91–93]

Regarding the type of structure, the technique can be divided into random or periodic structures. Following Yablonovitch's work, a random surface is able to create ergodic light propagation and, therefore, act as an effective light trapping technique to enhance the power provided by the solar cell. Different studies consisting of texturing or incorporating random structures have been proposed to enhance perovskite solar cells absorption.[92,94,95] Periodic structures have also proved to be good candidates for effective light trapping techniques, achieving a

similar enhancement to that obtained by randomness.[93,96–98] When the two approaches from different experimental studies are compared, however, it is difficult to analyse the light trapping effect independently since the type of perovskite device that is normally applied varies significantly between the two.

The main aim of a light trapping structure is to achieve maximum light absorption, but the analysis towards achieving such a goal can often be complicated since the maximum absorption limit in an experimental environment is ambiguous. Theoretically, the amount of light lost in the different parts of the cell can be analysed and, basically, divided into losses from the reflection of light at the substrate interface, losses due to light escaping from the cell and parasitic losses at different layers from the active material. Some studies have been reported that simulate the application of different approaches to avoiding these losses, claiming an absorption gain close to the maximum.[97,99] However, those relying on experimental work alone are unable to make such claims, as the fabrication of a device with the necessary requirements could lead to complications and other negative side effects.[100]

1.4.2 Recycling light into electricity with perovskite solar cells to increase energy efficiency

As well as developing solar cells that are able to efficiently convert solar energy into electricity, it is important to also consider further applications for the technology. For instance, applying PV technology in electronic devices or indoor applications to better manage light consumption could be a good solution for collecting the energy that would otherwise be wasted and converting it back into electricity. Perovskite solar cells, for example, have already been shown to perform efficiently under indoor light irradiance, making them appropriate candidates to feed self-powered indoor devices such as those used within the

Internet of Things or rechargeable portable devices.[101–103] Also, the direct application of perovskite based solar cells in low voltage resistive or storage devices has been proved to work effectively. In the 2020 study developed by Sun et al.,[104] a digital thermometer and sodium battery were powered for 24 hours from the conversion of emitted light into electricity in the perovskite solar cells.

As discussed previously, a few ensembles designed to polarise, homogenise and recycle the non-transmitted light have recently been developed, but the research has been restricted to light polarisation management. However, adapted optical designs along with PV devices appear to be good candidates for achieving such demands. Currently, the use of PV devices for the purpose of producing polarised light emission is mainly limited to polymeric materials, which absorb polarised light and transform part of it into electricity, but, unfortunately, the output is not sufficient to efficiently recycle light.[105,106] Another study suggests the application of polarising absorbing dyes, which transversally transmit one type of polarisation and re-emit the rest into a different wavelength. The emission is performed parallel to the film, which seems appropriate for its further collection by a solar cell, as the authors suggest.[107] Unfortunately, there is a lack of current literature that studies the design of a complete opto-photovoltaic ensemble, reporting both the optical and electrical performance for an application and fulfilling the described requirements.

In terms of energy efficiency, it is equally important to produce electricity using high efficiency power conversion techniques and to operate opto-electronic devices through optimised energy management processes. In Chapter 2, the application of a periodic geometry is applied to a perovskite solar cell as a light trapping structure in order to enhance its light harvesting properties and delivery of the electrical current. Chapter 3 describes the design and operation of a similar optical structure able to transmit polarised light homogeneously and recycle the

non-transmitted light into electricity through the integration of perovskite solar cells.

1.4.3 Low temperature perovskite solar cells

To limit energy fabrication costs, the manufacture of perovskite solar cells seeks to find a complete low-temperature process. In the most common n-i-p configuration, a mesoporous and a compact TiO_2 layer that require annealing above 450 °C are frequently employed to exploit the performance of the standard ETL structure.[32,34,36,108–111] P-i-n structured perovskite solar cells do not require such high temperatures, but, unfortunately, their performance in terms of maximum efficiency has typically been lower than the n-i-p structures, as shown in Figure 1.2. Other n-i-p options involve changing the TiO_2 nature,[112–114] applying different deposition methods[115–118] or, basically, changing the material employed.[45,119–122]

High temperatures applied to the mesoporous layer are often applied to sinter the material and remove the organic binder of the original paste, creating the porosity. In order to simplify fabrication of the solar cell, mesoporous structures could be avoided without decreasing the performance of the solar cell if an efficient compact ETL were employed.[47,115,123,124] When small nanoparticles are used in a dispersed solution, they act as compact layers since the density of the stacked nanoparticles avoids percolation of the perovskite material within them during its deposition. The advantage of this type of ETL is that, in most cases, it can be annealed at low temperature to achieve the desired electronic properties and to remove the low evaporation point solvent within which such nanoparticles are dispersed. Different n-type nanoparticles have been applied to perovskite solar cells,[125–128] with the SnO_2 nanoparticles employed in the study of Jiang et al.[129] being of special relevance. These created a very efficient ETL and have

been used in numerous other publications related to high efficiency and stable perovskite solar cells.[38,39,48,130]

While the mesoporous structure might not be critical for the high performance of perovskite solar cells, the compact layer seems to be much more relevant in high performance structures. As well as for the transfer of electrons, the role of the ETL is to act as a hole blocking layer in order to effectively separate charges so that they can reach their corresponding electrode. Moreover, isolating the contact electrode from a possible shunting path from the HTL is also important since such a contact considerably affects the operation of a solar cell. This event is especially likely when the active layer is thin, as is usually the case when semi-transparent solar cells with some degree of transparency are used to produce electricity. In Chapter 4, the application of two layers of different nanoparticles is shown to create an improved electron transport material (ETM) in low temperature perovskite solar cells, the results being particularly suitable in the fabrication of semi-transparent perovskite solar cells.

1.5 Thesis Outline

In this thesis we approach light harvesting through ergodic light trapping in perovskite solar cells, as well as the concept of energy efficiency in the fabrication and application of these cells. The former is described in Chapter 2, where a periodic structure made of interconnected half-cylinders is demonstrated to propagate light ergodically. The periodic array applied on a perovskite solar cell causes a light trapping effect that is comparable to the one obtained with a randomly textured surface. The light harvesting is enhanced in the solar cell, providing a larger electrical current. Such an increase allows the fabrication of a

perovskite solar cell with an equal performance using 30% less material, thereby considerably decreasing the amount of Pb required.

In Chapter 3, the energy efficiency in the diffused emission of polarised light is approached through the recycling of light that might otherwise be wasted in such a process. We propose an innovative design to emit broadband polarised light, and in which two perovskite solar cells recycle the non-transmitted light back into electricity. The design is optimised to efficiently polarise light while keeping light losses to a minimum. Furthermore, an ensemble is fabricated based on this design in order to characterise its optical and PV performance, proving the polarisation and light recycling effects. The proposed strategy increases the energy efficiency during polarised light selectivity and can be employed as an energy saving tool in optoelectronic devices such as LCD.

Finally, energy efficiency during the manufacture of perovskite solar cells is approached in Chapter 4. A novel low temperature fabrication procedure is studied, with the application of two different layers of nanoparticles, SnO_2 and TiO_2. In this study, the performance of the solar cells when combining both layers is enhanced compared to when just one of the materials is employed. Such an enhancement is particularly notable in semi-transparent devices, where a 30% enhancement in performance can be reached in devices with ultra-thin perovskite layers.

Chapter 2

Application of a half-Cylinder Photonic Plate for Enhancing Light Absorption on Perovskite Solar Cells

As discussed in the previous chapter, an ergodic light propagation inside a solar cell leads to an effective light trapping, resulting in a broadband light absorption. Unfortunately, except for a handful of cases where the surface random texturing is inherent to the cell structure,[131–133] introducing such disorder may have a negative effect on the electrical performance of the solar cell device. However, such a random textured surface is not strictly necessary to achieve ergodicity. Indeed, a periodically corrugated optical medium composed of intercalated optical fibres forming a plate, called a photonic fibre plate, leads to a chaotic light ray propagation. This type of propagation was used to enhance light absorption from an evaporated organic solar cell fabricated on one side of such a photonic fibre plate.[134] Although the regularity of the periodic surface certainly simplified the thin film solar device fabrication, it also limited layer deposition to processes fully based on high vacuum evaporation or sputtering. Therefore, a simpler geometry compatible with solution processed solar cells would be more versatile and suitable as an ergodic light trapping technique.

In this chapter, we study a periodic structure made of interconnected half-cylinders, called a half-cylinder photonic plate (h-CPP), which is able to

propagate light ergodically when light is reflected on its opposite surface. This structure, which is easily manufacturable on ultra-violet (UV) light or temperature curable materials, can be placed onto the glass side of the solar cell, thereby transferring such ergodicity to a solar device. By employing a numerical model that combines geometrical and wave optics, we analyse the light dispersion inside an h-CPP and its effect when it is applied on a perovskite solar cell. Firstly, we are able to confirm ergodic light propagation after light enters through the periodic structure. Secondly, we calculate the spectral absorption variation and J_{sc} enhancement when the h-CPP is integrated on the perovskite solar cell. Finally, the fabricated ensemble is experimentally characterised and, in section 2.2.1, the results obtained are compared to those from the numerical simulation.

2.1 Theoretical model for light propagation and optimal current generation

To analyse the light propagation inside an h-CPP, we created a theoretical model that combines both ray tracing and wave optics. In this model, the h-CPP is situated on top of a glass substrate with an ideal reflector deposited on the opposite side. As the geometrical dimensions of the h-CPP are large compared to the wavelengths of interest, a ray picture is suitable to describe the light trapping. An examination of Figure 2.1 indicates that ray trajectories depend significantly on the initial conditions, which is where the ray is incident on the h-CPP. Between two refraction/reflection events, the photons follow a ballistic trajectory. Therefore, the ray paths are entirely encoded in the set incidence angle β_j made by the j^{th} segment of ray with the interface at which it refracts or reflects. To

confirm the ergodic character of the h-CPP geometry from a geometrical optics perspective, one must determine the fraction of incoming rays that will follow an unpredictable trajectory upon entering the h-CPP. Indeed, any ray travelling to a different cylinder from its original one will subsequently undergo reflection/refraction at an almost unpredictable angle. Such a fraction is given by:

$$f = 1 - \frac{2x}{p} \tag{2.1}$$

where, as shown in Figure 2.1, x corresponds to the smallest horizontal distance between the top of a given cylinder and a ray that, upon a reflection at the bottom interface, enters a neighbouring cylinder of the array, while p is the period of the h-CPP. Provided that x is small compared to p, it is straightforward to demonstrate that the fraction of incident rays that upon incidence will follow a quasi-unpredictable trajectory is:

$$f \approx 1 - \frac{nd}{4h} \tag{2.2}$$

where h is the separation between the corrugated and planar interfaces of the h-CPP, n its index of refraction and d the diameter of the cylinder, as indicated in Figure 2.1. When n = 1.45, d = 104 µm, and h=1.15 mm, one obtains a value of 97%.

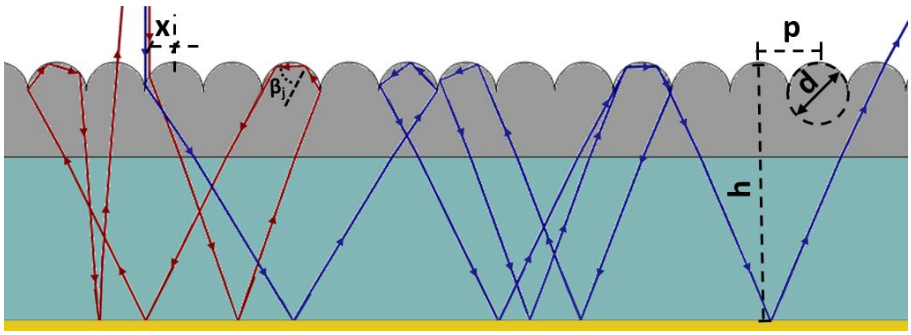

Figure 2.1 Ray trajectory simulation of two different rays upon an h-CPP on glass. The image is not at scale.

2.1 Theoretical model for light propagation and optimal current generation

In order to characterise the ray dynamics from a statistical point of view, it seems more useful to monitor not β_j but $\Delta\beta_j = \beta_j - \beta_{j-1}$. Indeed, rays bouncing on a circular boundary, and thus temporarily following a regular trajectory, satisfy $\Delta\beta_j = 0$. In Figure 2.2, we plot the cumulative distribution function (CDF) of $\Delta\beta$, which is the integral of the probability distribution of $\Delta\beta$. The CDF is computed as described in Ref. 134, by a ray tracing algorithm that generates a large sample of ray segments in the h-CPP, consecutive to a single ray impinging on the device. We keep track of the ray trajectories until the ray intensities have a very small value (0.0001 times the original value) in order to generate a sufficiently large statistical sample. We observe that we converge to the same CDF independently of the initial conditions, i.e., where the initial ray falls on the device and its incidence angle. In all our simulations we consider polarisations both parallel and perpendicular to the cylinder axes and take the average, and only a small difference is observed between the two polarisations, which we mainly attribute to the Fresnel coefficients at the air/h-CPP interface. We note that the CDF undergoes a finite jump at $\Delta\beta = 0$, indicating that a sizeable, finite probability is associated to that value. Hence, even though the ray trajectory is chaotic, a fraction of it is regular. This demonstrates that the ray chaos achieved by the h-CPP is of the intermittent type. Hence, independently of the initial conditions, any region of the phase space of the ray trajectories can be visited. This constitutes a numerical proof of ray ergodicity. Note that ergodicity is understood here in relation to the geometrical redistribution of the rays' segments inside the h-CPP and independently of their intensity, as in Ref. 70. The absorption of the intensity caused by a particular incoming ray does, of course, depend on its initial conditions, as described in Ref. 134.

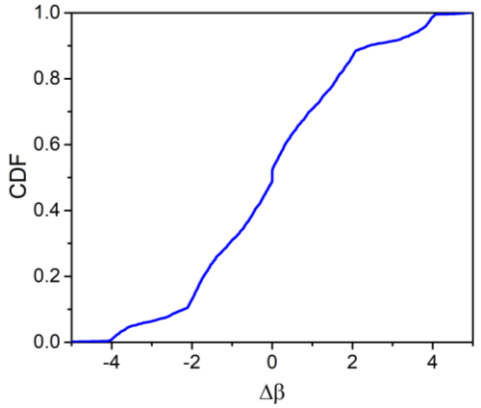

Figure 2.2 CDF related to the Δβ computed over a series of ray segments.

2.2 Ergodic light propagation and maximum electrical current generation.

2.2.1 h-CPP refractive index optimisation in order to maximise EQE and reduce Pb content

Given that ergodic light propagation occurs between an h-CPP and a reflective structure, it is expected that when a solar cell is placed after the h-CPP, its light absorption and, therefore, its current generation will increase. However, the boost in absorption will also depend on the optical parameters of the different elements and, therefore, a further analysis in this regard should be performed.

In order to take full advantage of the ergodic ray propagation, the refractive indexes of all layers, from the h-CPP to the cell active layer, should, in principle, be matched. However, increasing the refractive index of the h-CPP/substrate towards the higher index of the active layer would lead to an increased reflectivity at the air/h-CPP interface. Considering a 550 nm thick perovskite layer, the n and k of the perovskite solar cell layers included in Appendix A.1 and then, using a

numerical approach that combines ray optics propagation in the h-CPP/substrate structure with wave propagation in the multilayer cell structure, one can numerically compute the EQEs and corresponding integrated J_{sc} for different index values of the h-CPP/substrate ($n_{h\text{-}cpp}$). When a perovskite cell is considered, both magnitudes are shown as a function of the light incident wavelength in Figure 2.3 and Figure 2.4a, respectively. In Figure 2.3b, it can be seen that when $n_{h\text{-}cpp} \leq 1.4$, the EQE related to the visible range of the spectrum decreases as the $n_{h\text{-}cpp}$ is reduced, whereas the rest of the EQE increases slightly. Since the major contribution of the solar spectrum belongs in this range of wavelengths, the J_{sc} drops considerably, as shown in Figure 2.4. The reasons for this decrease are the lower absorption due to a higher mismatch between the refractive index of the cell and the structure, and the loss of the light trapping effect as the refractive index of the periodic array gets closer to n_{air} ($n_{air}=1$). On the other hand, analysing the effect of increasing the refractive index for $n_{h\text{-}cpp} \geq 1.45$, as shown in Figure 2.3c, one notices that as the n increases the curves flatten. This is translated into a slightly higher EQE for wavelengths between 450 nm and 600 nm, but lower for other wavelengths. Moreover, for $n_{h\text{-}cpp} \geq 1.65$ the whole EQE starts to decrease since the reflection of the incoming light is now considerable due to the refractive index contrast between the air and the h-CPP. The compensation of these effects determines the different light absorption and fixes the optimal index of refraction of the h-CPP/substrate structure between 1.4 and 1.65, as can be observed in Figure 2.4b. In summary, a maximum absorption is obtained when the correct balance between minimising reflectivity at the air/h-CPP interface and matching the indexes of the substrate and cell structure is reached.

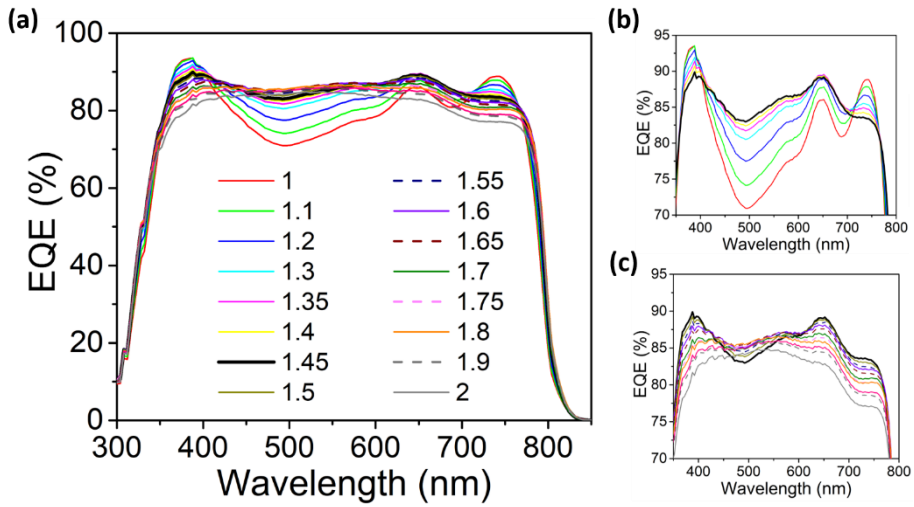

Figure 2.3 (a) Simulated EQE for devices with h-CPP considering different h-CPP refractive indexes. (b) Zoom in for the EQE curves for $n \leq 1.45$. (c) Zoom in for the EQE curves for $n \geq 1.45$.

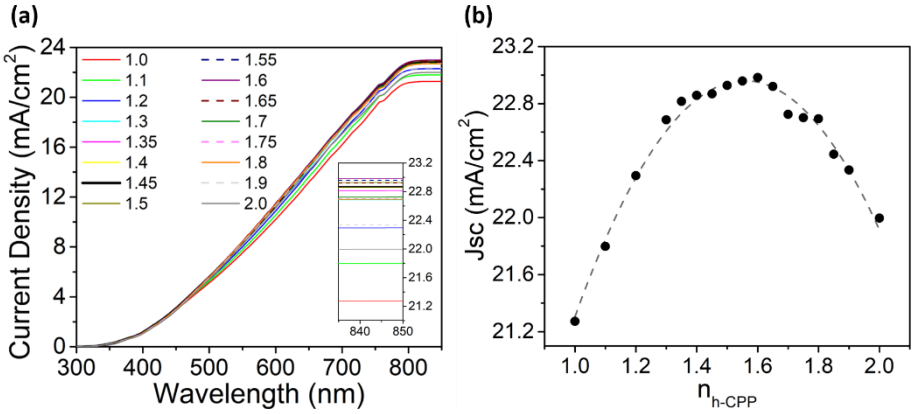

Figure 2.4 (a) Simulated accumulated current density obtained by integrating the EQE results for a device with an h-CPP, considering different h-CPP refractive indexes. The inset represents an amplification of the final wavelength area. (b) Short circuit current (solid dots) as a function of the index of refraction for the h-CPP/substrate structure. In this numerical computation we assumed that the index of refraction of the h-CPP and substrate are the same. The dotted line is a guide for the eye.

2.2 Ergodic light propagation and maximum electrical current generation.

Provided the h-CPP structure exhibits a 97% randomisation capacity, we may conclude that any other kind of regular or periodic[135–137] interface structuring would yield, at best, a similar enhancement achieved by the h-CPP. Rather than a different kind of interface structuring, a further enhancement of the light absorption percentage would require either a better back mirror to reduce parasite absorption or a thinner active layer, as shown in Figure 2.5. It is worth noting that for the h-CPP configuration and a 450 nm thick active layer, the short circuit current (J_{sc}=22.21 mA/cm^2) approaches that obtained with a 650 nm thick active layer in the standard planar configuration (J_{sc}=22.29 mA/cm^2). This means that the fabrication of the cell can provide the same current while using less material. In particular, the type of perovskite solar cell used in this study achieves the best performance with a perovskite thickness of between 600 and 700 nm.[36,129] Therefore, 30% less material could be employed by using this approach. By just adding a simple h-CPP at the light entering interface, this reduction in material translates to the same decrease in Pb for the fabrication of a perovskite solar cell that can achieve the same performance.

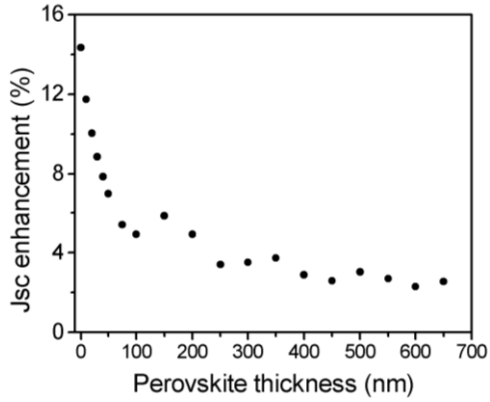

Figure 2.5 Simulated J_{sc} enhancement when an h-CPP structure is added for different perovskite solar cell thicknesses.

2.2.2 Experimental results and analysis of the optimal device configuration

Given the simulated results, polydimethylsiloxane (PDMS), whose refractive index is within the optimal range (n=1.45), seems to be a relevant choice as a material for the fabrication of an h-CPP. Moreover, it provides complete transparency, it is flexible and it can be cured and moulded easily. Therefore, the light trapping and harvesting configuration considered consists of an h-CPP deposited on one side of a 1 mm thick fused quartz glass substrate and a perovskite solar cell deposited on the opposite side of that same substrate. The overall structure and fabrication method that we implemented allow the integration of a light trapping element with a solar cell without having to impose any restrictions or limitations on the fabrication of the solar device. Such a light trapping structure can be implemented for perovskite solar cells provided that light absorption is never complete for the standard perovskite cell configuration,[138,139] especially in the NIR region of the sun spectrum, which is, in principle, the most interesting because it exhibits the largest photon flux.

The solar cell structure employed for this study, whose cross section scanning electron microscopy (SEM) image is shown in Figure 2.6a, was ITO (100nm)/SnO_2 (20 nm)/$(FAI)_x(MABr)_{1-x}PbI_2$ (550 nm)/Spiro-OMeTAD (200 nm)/Au (60 nm). This cell was fabricated following a low temperature process as described in Appendix B. As shown in Scheme 2.1, a freestanding h-CPP of PDMS was fabricated separately and subsequently deposited on the unused side of the glass substrate. First, a PDMS layer was deposited by spin coating on top of a 1″ × 1″ aluminium–nickel mould patterned with the negative h-CPP structure (Film Optics Ltd.). Then the PDMS was cured at 90 °C for 1 hour and removed from the mould, creating a flexible freestanding h-CPP, as shown in Figure 2.6b.

2.2 Ergodic light propagation and maximum electrical current generation.

The pattern geometry consists of 110 intersected semicylinders per cm, with diameters of 104 μm, 91 μm apart, centre to centre. The freestanding 1″ × 1″ h-CPP was deposited by simple physical contact on the bare glass substrate on the opposite side to where the perovskite cells had been previously grown.

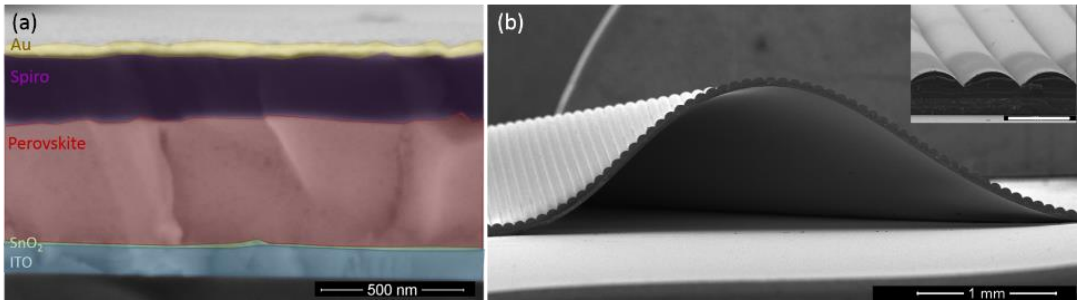

Figure 2.6 (a) Cross section SEM image of a perovskite solar cell. The layers have been tinted for clear identification. (b) Cross section SEM image of a freestanding h-CPP. The inset represents a closer view of the h-CPP; the scale bar in the inset corresponds to 100 μm.

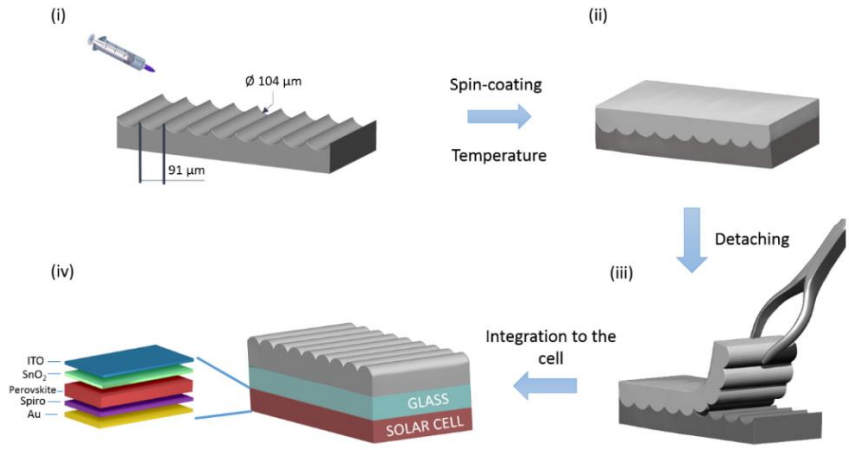

Scheme 2.1 H-CPP fabrication process: (i) Deposition of the PDMS on the mould. (ii) After spin-coating and annealing of the film, the PDMS is cured. (iii) Then the PDMS is detached from the mould, creating the h-CPP. (iv) The h-CPP is integrated into the solar cell by attaching it to the glass side.

To determine the effect of the h-CPP on the performance of the perovskite solar cells, we measured the current density-voltage (J-V) curve and determined the corresponding PV parameters. Since the h-CPP can be easily deposited and removed from the glass substrate without affecting the PV device operation, in order to analyse the h-CPP's contribution on the cell performance in a reliable manner, the PV parameters of the exact same solar cell were measured with and without the h-CPP. In Figure 2.7a one can observe how the J_{sc} of the perovskite solar cell is enhanced from 22 mA/cm^2 to 22.6 mA/cm^2 when the h-CPP is applied. As expected, the rest of the PV parameters, i.e., V_{oc} and FF, are essentially not affected when the h-CPP is applied to the solar cell. In other words, the increase in the photocurrent is the main factor that causes an increase in PCE from 18.1 % to 18.8% for the cell whose J-V curve is shown in Figure 2.7a. In total, 24 devices were analysed and their box plot diagrams for the corresponding PV parameters are shown in Figures 2.7b-e. Therefore, it is confirmed that, essentially, the only parameters modified by the application of the h-CPP were the J_{sc} and, consequently, the PCE, whilst the V_{oc} and the FF remained almost unaltered. From Table 2.1, one may note that the average gain in J_{sc} caused by the h-CPP is 0.58 mA/cm^2, corresponding to a 2.7% photocurrent enhancement, leading to a maximum PCE of 19.8% for the cells incorporating the h-CPP.

2.2 Ergodic light propagation and maximum electrical current generation.

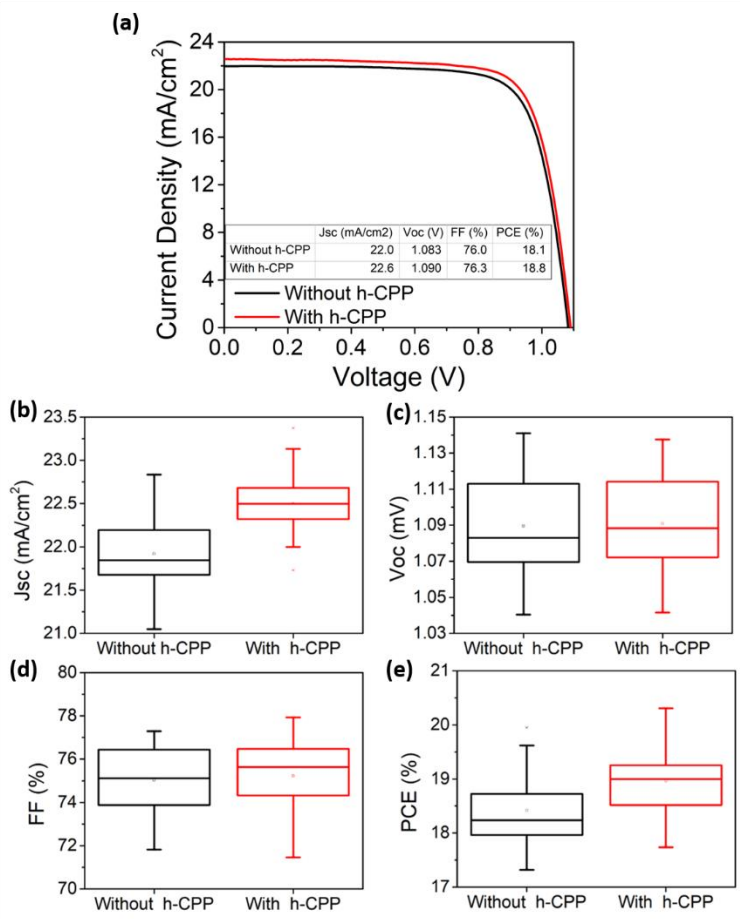

Figure 2.7 (a) J-V curves of a representative device with and without h-CPP. (b) J_{sc}, (c) V_{oc}, (d) FF and (e) PCE statistical analysis of 24 different perovskite solar cells with and without the h-CPP.

Table 2.1 Average PV parameters and gains obtained for 24 devices with and without an h-CPP.

	J_{sc} (mA/cm^2)	V_{oc} (V)	FF (%)	PCE (%)	Best PCE (%)
Without h-CPP	21.81 ± 0.53	1.088 ± 0.03	75.07 ± 1.5	17.82 ± 0.72	19.44
With h-CPP	22.39 ± 0.54	1.089 ± 0.03	75.28 ± 1.8	18.36 ± 0.74	19.81
Gain	0.58 ± 0.12	0.001 ± 0.006	0.21 ± 0.67	0.54 ± 0.19	

The PV parameter study above confirms that the use of an h-CPP in perovskite solar cells leads to an overall enhancement in light absorption and cell performance. To gain further insight into such an enhancement, we computed the EQE for perovskite solar cells with and without the h-CPP and then compared them to the experimentally measured results. From the numerically computed EQEs shown in Figure 2.8a, one can clearly distinguish two very distinct features. On the one hand, the h-CPP structure contributes to an enhanced absorption in spectral regions where the absorption coefficient of the perovskite is weaker. An example of this is in the NIR, where a clear enhancement, peaking at the perovskite absorption edge, can be seen in Figure 2.8a. On the other hand, the h-CPP structure has a tendency to flatten the EQE, pushing it close to the corresponding internal quantum efficiency, by compensating for the destructive interference between the forward and backward propagating light waves. Valleys in the EQE of the cell without an h-CPP, which are distinguishable at around 500 nm and 725 nm, are likely to be the result of such destructive interference, provided that they do not equate to any decrease in the perovskite extinction coefficient, as shown in Figure 2.9. The destructive interference is a consequence of the multilayer dielectric structure inherent to any PV thin film device.[140,141] In the cases of both weak absorption and destructive interference, the ergodic light propagation caused by the h-CPP structure has the effect of effectively increasing the length of the light path in the perovskite layer. The main features observed in the numerically computed EQE enhancement curve are, to a large extent, reproduced in the experimentally determined curve, as shown in Figure 2.8b. Indeed, the peak of the enhancement curve at the absorption edge and the tendency to broadly flatten the EQE are also confirmed experimentally. Nonetheless, one should not expect a perfect matching between theory and experiment if large variations are observed in the complex refractive indexes of

different perovskite layers, caused by uncontrollable alterations in the growth procedure of such layers.

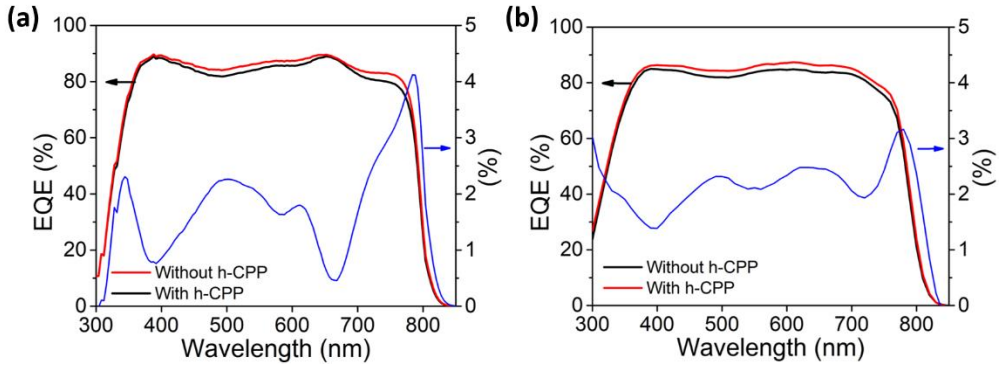

Figure 2.8 (a) Simulated and (b) experimental EQE for solar cells with (red curve) and without (black curve) an h-CPP. Blue curves represent the EQE gain depending on the wavelength.

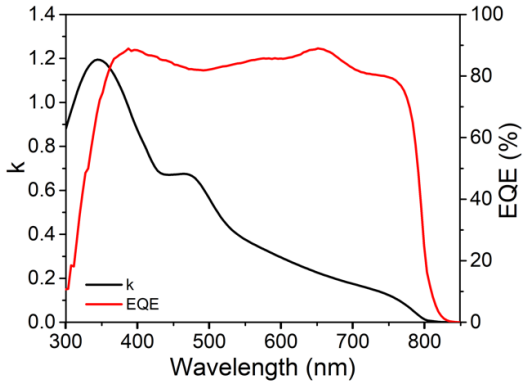

Figure 2.9 Comparison between the simulated EQE curve for a planar device and its perovskite extinction coefficient (k).

2.3 Conclusions

It has been demonstrated that a one-sided simple ordered cylindrical structure is able to propagate light chaotically and randomise it. This structure

can be easily fabricated and integrated on any surface for use in a diverse range of photonic applications. For instance, if a thin film absorber is placed between the h-CPP and a reflective surface, the ergodic light propagation causes an absorption enhancement comparable to the absorption achievable by a randomly textured surface.

When an h-CPP is placed on the glass side of a perovskite solar cell, the numerical simulation carried out to study its light diffusion is able to predict the increase in the current generation of the solar device induced by the ergodic light trapping mechanism. Once the h-CPP material has been optimised and applied to a perovskite solar cell, the photogenerated current is enhanced close to the maximum achievable for any kind of regular or periodic structuring at the light entering interface. Such an enhancement can equal the current generated by a device with an active layer of an optimised thickness but containing 30% less material, considerably decreasing the amount of Pb necessary in the fabrication.

The same conditions as the theoretic analysis were replicated experimentally and the PV parameters of a set of solar cells were analysed with and without the h-CPP. The experimental results showed good agreement with those obtained in the theoretical simulations along the broad solar cell absorption range. All these results confirm that the proper design of a periodic structure at a light entering surface is able to create ergodic light propagation in the same way as on a random surface. In addition, we have demonstrated the application of such a simple structure as light trapping mechanism to enhance light harvesting in perovskite solar cells, in agreement with one of the approaches laid out for this thesis. This type of ordered structure can easily be superficially tuned if necessary, as will be presented in the next chapter, while the opposite face can be kept flat to allow for its integration on any type of surface.

Chapter 3

Light Recycling Using Perovskite Solar Cells Incorporated in an h-CPP for Polarised Light Emission

In Chapter 2, we demonstrated how a simple and periodic geometry such as the one found in an h-CPP is able to ergodically propagate light and enhance light harvesting in perovskite solar cells when it is placed on its light entering surface. Such randomisation of light could also be useful in other environments in which a precisely homogeneous emission of diffused light is required.[142–144]

In this chapter, we propose the novel design of an efficient light recycling structure with the ability to emit polarised light from its top surface while guiding the rest of the light to the edges to be recycled into electricity by two perovskite solar cells. We are able to separate the polarised light by depositing a reduced number of nanometric layers on the h-CPP top surface using widely applied fabrication methods. The structure is optically characterised and compared to the expected results obtained by the simulated performance. Finally, an ensemble equivalent to the proposed design is constructed to demonstrate the ability of perovskite solar cells to recycle the non-transmitted light into electricity in such a design.

3.1 Light propagation inside an h-CPP and its polarisation capability

3.1.1 Ray optics for light inside an h-CPP

In Chapter 2, we described a theoretical model to account for light propagation in an h-CPP structure. The amount of light transmitted or reflected when a ray hits one of the half-cylinders in such a structure will depend on two parameters: the refractive index contrast of the materials at the interface and the angle of incidence of the ray. For rays travelling inside the h-CPP, the effect of the total reflectance for angles of incidence higher than the critical angle can only be modified by changing the n of either the two media at the interface. If an ideal reflector is considered on the bottom of the h-CPP, light reflected on the periodic array will either end up being transmitted from the top in subsequent incidences or guided to one of the plate edges. Figure 3.1 shows a ray tracing diagram, representing one ray travelling inside the h-CPP with $n_{h\text{-}CPP}$=1.52 and n_{air}=1, the critical angle in this case being 41.1°.

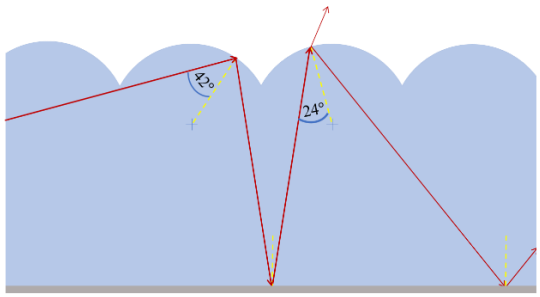

Figure 3.1 Ray tracing inside the h-CPP with $n_{h\text{-}CPP}$=1.52. The image is not to scale.

For incidence angles lower than the critical angle, the fraction of light that is transmitted or reflected can be managed by optically modifying the structure surface. This can be achieved by depositing a set of alternating nanometric layers

of two different materials with a certain refractive index contrast. Indeed, the interference will be polarisation-dependent in such a way that if it is applied properly, polarisation selectivity of light can be achieved. If this effect is combined with proper light diffusion, it is possible to transmit polarised light homogeneously from the h-CPP.

3.1.2 Light dispersion

In order to emit light homogeneously across the guide, the light inside the h-CPP should be evenly dispersed, which means that approximately the same quantity of light needs to move towards the right and the left sides. Therefore, light should start to be randomly dispersed at the middle of the h-CPP. To achieve this, light is inserted from one of the sides and pointed through the reflector so that it hits roughly the centre of the periodic array. In general terms, given a certain h-CPP length and a specific distance between the reflector and the periodic array, there is an appropriate angle range that ensures a generally homogeneous emission.

Assuming that light enters from the centre with respect to the vertical position of the guide (*t/2* in Figure 3.2), the angle that provides a reflection towards the middle of the top h-CPP can be obtained from:

$$x = \frac{1.5t}{\tan(\propto_o)} \qquad (3.1)$$

where *x* is the horizontal position, *t* the distance between the reflector and the top of the h-CPP and $\propto_o$ the angle of the light source with respect to the horizontal axis of the h-CPP (or to the reflector surface) pointing towards it. In order to study how the angle affects the emission and dispersion, for this and further analyses we will assume the h-CPP length to be 31 mm and *t*=2.2 mm. Following Equation 3.1, in order to reflect the light onto the top middle part of the h-CPP

(x=15.5 mm), the light source should be pointing towards the bottom reflector at an angle $\propto_o$=12°.

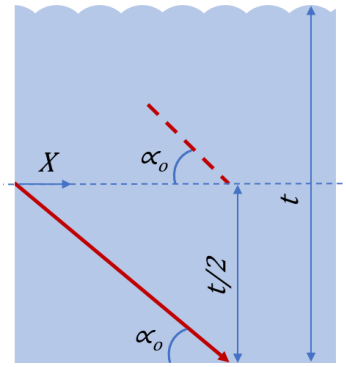

Figure 3.2 Diagram of light coupling into the structure. The red arrow represents the light beam considered. The image is not to scale and only a portion of the guide is considered.

3.1.3 Surface modification for light emission management

After the light hits the top of the h-CPP, it will be randomly dispersed along the guide in further bounces due to the effects of ergodic light propagation. Due to the same ergodic effects, the angles of incidence could also be considered random. At this point, the amount of transmitted light can be managed by optically modifying the surface of the h-CPP. To create photonic surface effects, dielectric multilayers have been widely employed in a lot of optical applications, such as mirrors, wavelength selecting filters, polarisers and many others.[145–150] When the effect pursued is monochromatic, an 1D photonic crystal can be employed by alternating high and low refractive index nanolayers in a periodic configuration. However, if the optical effect has to be reached for several different wavelengths of a broadband spectrum, this periodicity is usually unsuitable, so a more complex analysis or design needs to be carried out to find the optimal configuration.

Taking into consideration the geometry of the structure, an inverse design approach has been followed in order to apply this technology to light polarisation. This has been achieved by using a reflectivity-based selection for specific wavelengths and to give sufficient transmittance. We have calculated the optimal thickness for each layer, composing a multilayer that works for three different wavelengths in the red (λ_R), green (λ_G) and blue (λ_B) parts of the visible spectrum. We have considered these three particular wavelengths because, by tuning the relative intensities of their light sources, one may obtain any colour from the visible spectrum. The simulation has been carried out using WO_3 and LiF as the materials of high and low refractive index, respectively, and their parameters are described in Appendix A.2. These two materials are non-absorbing (k=0) in the visible spectrum and, therefore, all non-transmitted light hitting the multilayer interface will be reflected. To account for certain losses that might be generated on the flat reflective surface opposite to the half-cylinders, which would affect the results considerably, a non-ideal structure was considered. In this case, a multilayer made of TiO_2 and SiO_2, with a total of eight alternating layers, was incorporated on top of a silver layer to ensure ultra-high reflectivity with minimal absorption losses. The configuration of the reflective structure is described in Appendix A.3.

Figure 3.3a shows that, for a given source angle with respect to the reflector $\propto_o$=12°, the transmittance of s-polarised light (Ts) decreases, while the p-polarised light transmittance (Tp) remains more or less constant as the number of layers composing the stack rises. This means that the value of the polarisation ratio (Tp/Ts) seems to stop rising after a certain number of layers. The Tp/Ts ratio shown in the image is an average of the results found for the red, green and blue (RGB) wavelengths for which the multilayer stack was designed.

3.1 Light propagation inside an h-CPP and its polarisation capability

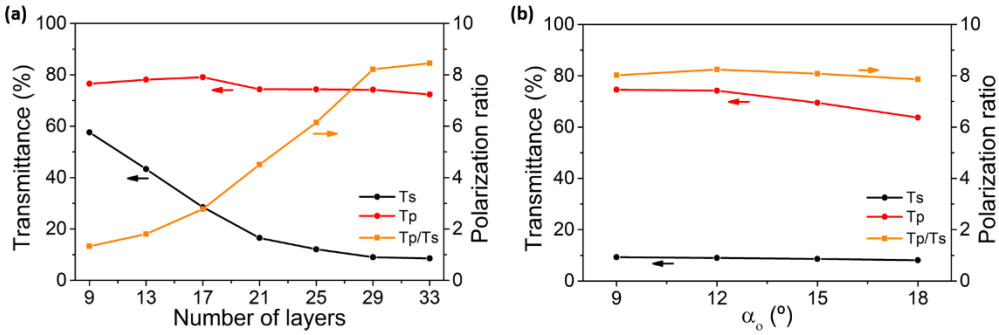

Figure 3.3 Ts, Tp and polarisation ratio as a function of (a) the number of layers in the stack, with a source angle of $\propto_o$=12°, and (b) the source angle $\propto_o$ using 29 layers in the stack

Another important factor to consider and analyse is the effect of the angle of the light source with respect to the reflector on the amount and type of transmitted light. To this end, the same simulation was performed with the number of layers fixed at 29 and changing $\propto_o$ within a range in which the first light impingement is centred relatively close to the top of the plate (15.5 mm ± 5 mm). The configuration of the 29 multilayer stack is described in Appendix A.3. This analysis is shown in Figure 3.3b, where no significant difference can be seen.

Since the overall light transmitted through the top decreases as the number of layers in the stack increases, it is expected that more light will reach the edges. Figure 3.4 shows that it does, indeed, occur evenly on both sides of the photonic plate for all the stacks considered, in the exact way that it was designed to operate. Figure 3.5 represents the share of light that reaches each of the edges as a function of $\propto_o$. When $\propto_o$ is increased or decreased from the angle that induces the light source to hit the middle of the h-CPP top surface, light reaching the left or the right edge, respectively, increases. This effect is more prominent when the angle is lowered instead of increased, as can be seen in Equation 3.1, since the position where the ray first hits the h-CPP surface is inversely proportional to tan($\propto_o$).

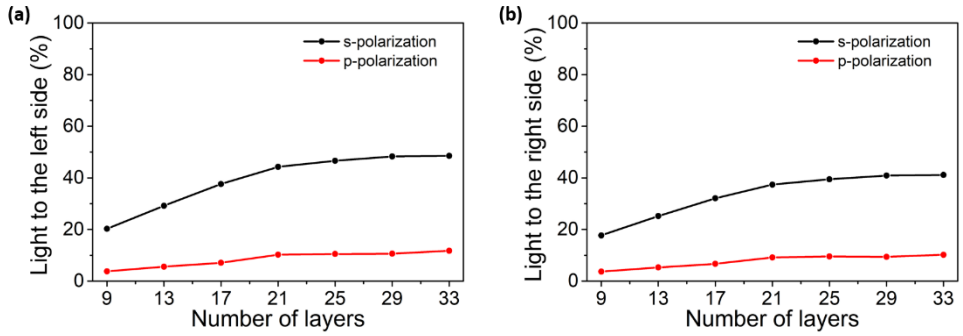

Figure 3.4 s- and p-polarised light guided to (a) the left and (b) the right side, assuming an angle of incidence $\propto_o$=12°.

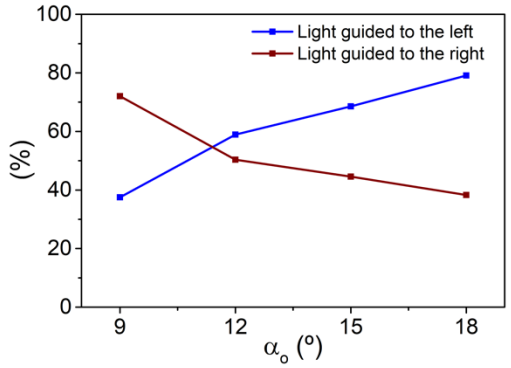

Figure 3.5 Relative amount of light guided to each side as a function of the light source angle of incidence $\propto_o$, when 29 layers are considered.

3.2 Description of a light recycling guiding plate to efficiently emit polarised light

The type of light propagation that occurs inside an h-CPP might be suitable in opto-photonic devices in which light needs to be selectively transmitted, while the rest is rejected. However, discarding the rejected light lowers the energy efficiency of the opto-photonic device and, therefore, an appropriate light management mechanism should be employed. Scheme 3.1 shows the design of an ensemble able to transmit polarised light, while the rejected light is recycled

by a pair of PV devices placed on its sides, where the non-transmitted light is converted into electricity. In this device, the light coupled from a light source enters the h-CPP at a particular angle, $\propto_o$ (1) and first hits the bottom reflector (2) where it is reflected towards the top part of the h-CPP. On the top part, there is a multilayer polarising stack comprising alternating layers of two different materials with contrasting refractive indexes (3). Here, the light is polarised and a certain amount of the total p-polarised light is transmitted while the rest of the light is reflected down. The remaining light inside the h-CPP will follow this same propagation process until it reaches one of the perovskite solar cells (4 and 5) on both sides of the device, where the light is then recycled by converting it back into electricity. In this design, almost all of the light will be either transmitted from the top or absorbed into the perovskite solar cells. As we will see below, this is the optimal type of PV device for the presented application.

As a proof of concept, the different elements described in Scheme 3.1 have been fabricated in order to analyse them independently and, also, all together, with a similar arrangement to the one described previously. The main goal is to prove the viability of the design by demonstrating the reflective polarisation at the same time as showing that the non-transmitted polarised light is being converted back into electricity with a higher s-polarised light contribution. Further work would need to be carried out in order to achieve the best performance of such a device based on the previous concepts.

Firstly, we will look at the different elements, discussing their potential performance and suitability for the proposed application.

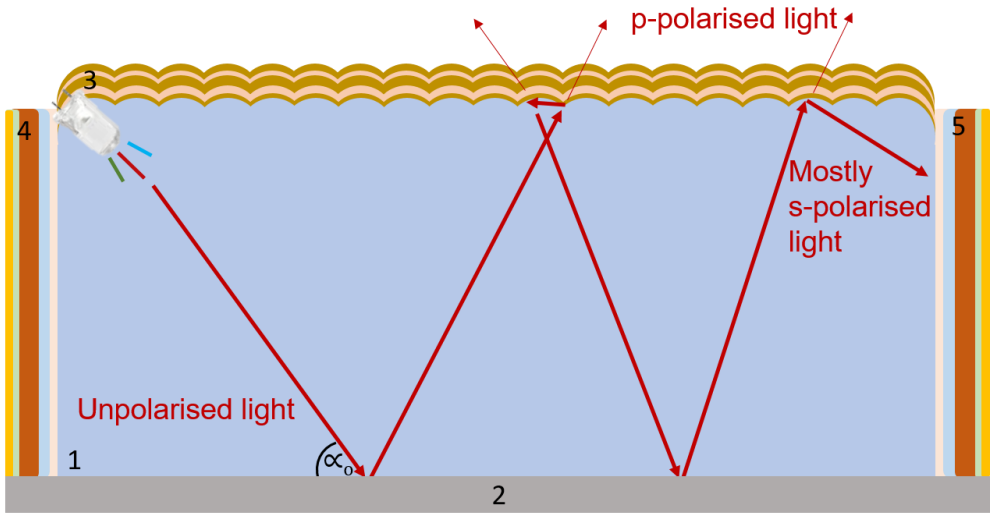

Scheme 3.1 Polarised light emitting ensemble with light recycling. (1) h-CPP, (2) reflector, (3) multilayer polariser stack, (4) and (5) perovskite solar cells.

3.2.1 An h-CPP as a light-guiding element

Light propagation inside an h-CPP has been already widely discussed throughout Chapter 2. Homogeneous light emission with respect to the horizontal position depends mainly on the point along the plate where light randomisation starts. Moreover, the top geometry will not only act as an element to force a chaotic light propagation, but will also contribute to the outcoupling of light since, for many light incidence events, the angle of incidence with respect to the surface is likely to be lower than the critical angle. Choosing the correct material to achieve a balance between outcoupling and a fair polarisation selectivity needs to be considered. Other important considerations are the availability of materials and the processing methods that will be compatible with the deposition of the polarising structure on the h-CPP corrugated surface. Several polymeric materials are available for patterning, using a mould with the geometry of the h-CPP. For this application, we chose OrmoComp®, a UV curable hybrid polymer

that offers high stability under thermal stress. This material is completely transparent in the visible spectrum and presents a refractive index of n=1.52, which is similar to the borosilicate standard glass used as its substrate. The fabrication process is simple. Firstly, the polymer is spin-coated on the mould and a glass substrate is placed on top of the coated master. Then a couple of clips are placed to sandwich both elements and ensure contact before the sample is placed under UV light for 10 minutes. Next, the glass substrate with the patterned polymer is separated from the mould and is placed under UV light for a further 10 minutes. Finally, the patterned sample is placed in an oven for 3 hours at 150 °C to increase its thermal and environmental stability.

3.2.2 Reflective element

The bottom reflector is an important element that needs to be designed carefully. An ideal reflector reflects all of the light with no losses, but actual reflective materials may have certain absorption or transmission that can compromise the quality of the reflection. Although an improved reflector can be fabricated by combining a Bragg reflector with a metal layer below, as proposed in Section 3.1.3, for the sake of simplicity during fabrication in our experimental ensemble, we will use a high-quality metallic layer as a simple mirror. Standard metals such as aluminium and silver are often employed to act as reflective surfaces. Given that reflectance should be as high as possible for the RGB spectra, silver seemed to be the most appropriate material since it is a common material and its reflective capability will produce low losses in this wavelength range.

A 150 nm silver layer was deposited by thermal evaporation and characterised by ellipsometry, and its refractive index is described in Appendix A.2. Figure 3.6 shows the different spectra of the silver reflectance based on

simulations and experimental measurements. Two type of simulations were performed, one using the refractive index obtained by fitting the ellipsometry characterisation, and the other using the refractive index described by Palik,[151] whose calculations are taken to be the standard optical parameters for silver. The simulated reflectance obtained using the refractive index from the silver deposited in our lab showed higher reflectivity than the simulated one obtained from Palik's refractive index. This means that the silver we were able to deposit had a higher reflective potential than the more common version, minimising losses. The experimental measurements of the layer reflectance are also included, and show a good matching with the simulated measurements, with only minor discrepancies.

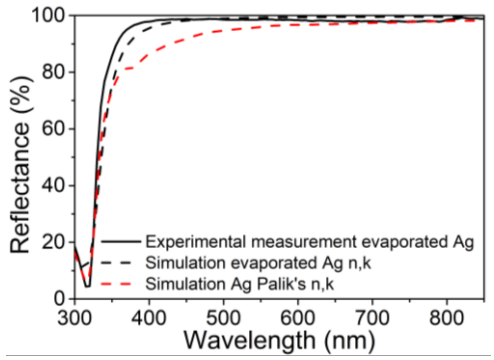

Figure 3.6 Reflectance of a 150 nm Ag layer, experimentally measured and simulated, based on the refractive index obtained by ellipsometry and described in literature.

In order to evaluate the difference in reflection between a simple silver layer and a more complex reflective structure made using a Bragg reflector, the effects of both were analysed by comparing the simulated losses when each was placed on the bottom of a polarising h-CPP. As shown in Table 3.1, when just a simple layer of evaporated silver is included, the loss caused by the reflective element after the complete light propagation is, on average, 8.73%, whereas if a Bragg reflector is added, there is only a 2.15% loss.

Table 3.1 Calculated light absorption in the reflective structure of the device when an evaporated silver layer and a Bragg reflector together with a silver layer are considered.

Reflective element	Wavelength (nm)	Absorbed s-polarised light (%)	Absorbed p-polarised light (%)	Total absorbed light (%)
Ag layer	466	15.7	11.3	13.50
	560	8.4	5.9	7.15
	630	6.8	4.3	5.55
Bragg reflector + Ag layer	466	1.6	4.9	3.15
	560	1.5	2.2	1.85
	630	1.4	1.5	1.45

3.2.3 Perovskite solar cells as light-to-electricity converters

A light recycling element should be a PV device that efficiently converts light into electricity, otherwise part of the light absorbed will be lost, affecting the overall device performance. Solar cell electrical losses, mainly governed by charge recombination, can be estimated by the difference between the bandgap energy (E_g) of the active material in eV and the characteristic V_{oc} of the solar cell under illumination. From the different alternatives available in PV devices, perovskite solar cells seem to be the best option for our application since they offer high efficiencies and a tuneable bandgap with high absorption in the visible spectrum. Moreover, during the past few years, perovskite solar cells have been improved, and are now better able to minimise recombination and achieve differences between the E_g and V_{oc} in the range 0.32-0.41 eV, depending on the bandgap of the perovskite.[152]

Another important aspect when considering the proposed application is the need to employ solar devices with wide bandgaps that are as close as possible to the longest wavelength of the light they are designed to absorb. In the case of the

RGB wavelengths, this corresponds to λ_R, which is 635 nm (1.95 eV). Bandgap modification is already a topic of interest in perovskite solar cells, especially in tandem applications with other PV materials.[41,153,154] Nevertheless, trying to achieve a higher energetic bandgap together with a high efficiency is not a straight forward process, since changing the composition of perovskite also affects its crystallinity and the number of possible defects in the material. For this reason, there needs to be a compromise between a bandgap as close as possible to the edge absorption and an efficient solar cell with low V_{oc} losses.

In our experiments, an efficient perovskite solar cell with low losses was used to convert the non-transmitted light into electricity. The bandgap of the employed solar cell was 1.53 eV, even though this is not the most suitable bandgap, given its difference with respect to the λ_R energy. In order to prove the ability of our device to efficiently recycle light into electricity, our experiments were based around employing a standard perovskite solar cell. However, in reality, a wide bandgap perovskite would be more appropriate to study the scope of our application. Further work is being developed in order to obtain improved light-to-electricity conversion in this respect.

3.2.4 Polarising multilayer stack

As previously described, in our device the transmission of polarised light is carried out by a multilayer stack, while the rest of the light stays trapped inside the guiding structure. The phenomenon behind this effect is ruled by the Brewster's angle at each of the interfaces in the multilayer. For any given refractive index contrast between two materials, Brewster's angle is the angle of incidence for which the reflectance of p-polarised light at that interface is zero. For other angles, the difference in the reflectance between both polarisations decreases. When this phenomenon is combined with the high reflectance of s-

polarised light for a wide range of angles and the wavelengths of interest, the polarisation ratio obtained for the transmitted light can be large, being an effective and non-absorbing polarisation selectivity mechanism.

The objective is to create a multilayer stack that is simultaneously able to reflect all or almost all of the s-polarised light without absorption, while also transmitting a large fraction of the p-polarised light. It is widely known that such an effect can be produced for a narrow wavelength range using a periodic multilayer stack that fulfils Bragg's condition. In this case, adding layers to the periodic structure will better increase the reflectivity on that wavelength range. However, when pursuing this same effect for several wavelengths relatively far from each other, the design of the multilayer is less straightforward. For this reason, prior to fabrication, an optimised multilayer structure should be calculated by applying, for instance, an inverse design approach. Beforehand, however, the materials to be deposited need to be defined, taking into consideration the suitability of a given deposition method with the h-CPP material and surface properties.

3.3 Fabrication and characterisation of a multilayer polariser stack on an h-CPP

3.3.1 Deposition techniques for the fabrication of a multilayer polarisation stack

When analysing the fabrication of our multilayer polariser stack, two deposition methods, thermal evaporation and magnetron sputtering, were studied in order to compare their suitability and performance. Both techniques present

different characteristics that make them suitable for depositing the multilayer on the h-CPP surface, with both methods offering good performance and controllable material characteristics in an acceptable time frame.

Table 3.2 Summary of the characteristics of the relevant deposition techniques for the fabrication of a multilayer polarising stack.

		Thermal Evaporation	**Magnetron Sputtering**
Materials	**High n (Avg. n)**	WO_3 (2)	TiO_2 (2.37)
	Low n (Avg. n)	LiF (1.35)	SiO_2 (1.45)
Average deposition rate (nm/min)		3-4	1
Position of the material source		Parallel to the sample	Tilted
Kinetic atom energy		Lower	Higher
Heat transfer		Higher	Lower

Table 3.2 summarises the different characteristics of both deposition techniques tested, along with the materials required for each technique. Each method offers certain positive characteristics that make it a good choice. On the one hand, thermal evaporation is often faster than magnetron sputtering. Even if one employs reactive sputtering deposition, this technique remains between 3 and 4 times slower than the thermal evaporation deposition rate. Also, the thermal evaporation material source points towards the sample perpendicularly to its surface, which, considering that the deposition surface has a periodic corrugation, seems to be more appropriate for a homogeneous deposition, in order to avoid shadowing by the structure itself. On the other hand, sputtering materials show a

higher refractive index contrast, which means that better polarisation performance may be achievable with fewer layers. Moreover, the stack fabricated by magnetron sputtering could be more robust, since the adhesion of the layers is normally better due to the higher kinetic energy of the species during deposition, while the temperature of the substrate is kept lower than in thermal evaporation processes.[155]

3.3.2 Results and discussion for the multilayer deposition: thermal evaporation vs magnetron sputtering

To test the suitability of each deposition technique, different stacks were deposited on h-CPP samples and their optical performance and morphology were analysed. First, the optical performance was analysed on a stack of five layers deposited using the two different techniques. For this study, a flat glass substrate was included during each of the deposition stages, together with the h-CPP substrates. Once the layers were deposited, the flat samples were measured by ellipsometry and their spectra were fitted to obtain the corresponding thickness for each of the layers in both multilayers. At the same time, with an optical setup schematically shown in Figure 3.7, the h-CPP samples were characterised by measuring their total transmittance when either s- or p-polarised light was introduced at normal incidence through the glass side of the substrate. Then a simulation replicating the measurements was performed on the h-CPP surface with stacks of the thicknesses obtained by the ellipsometry fitting spectra. Figure 3.8 shows the comparison between the measured and simulated total transmittance of a polarising h-CPP for the different deposition techniques.

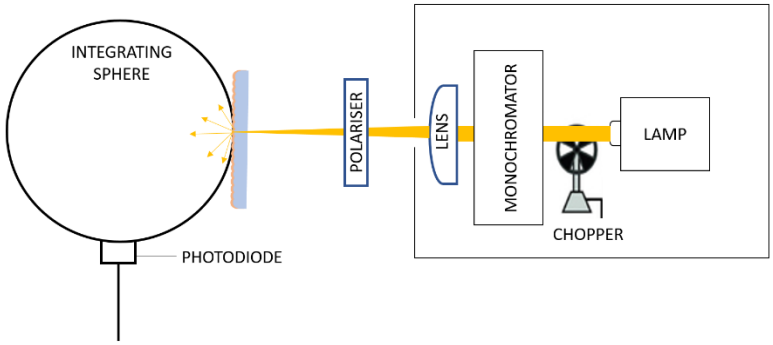

Figure 3.7 Optical set-up for total transmittance measurements.

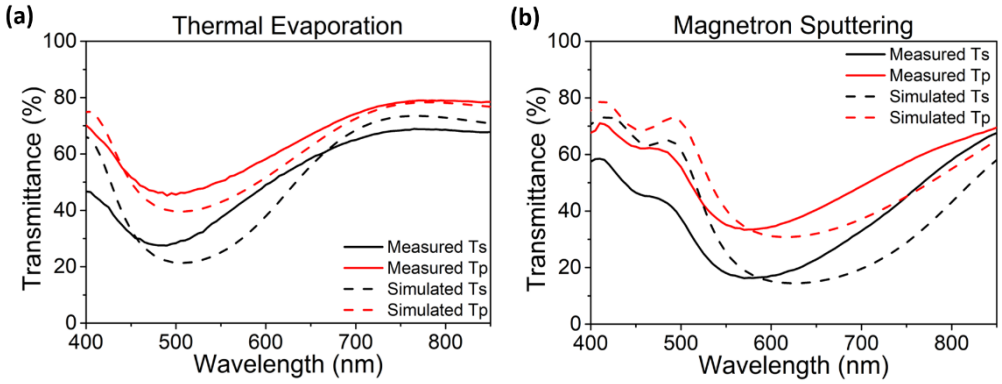

Figure 3.8 Measured (solid) and simulated (dashed) total transmittance when light is introduced in the h-CPP at normal incidence through the glass side for samples fabricated by (a) thermal evaporation and (b) magnetron sputtering.

As previously explained, the multilayer needs to be highly reflective in order that polarisation occurs efficiently while the non-transmitted light is guided to the sides to be recycled into electricity. Therefore, the structure must be able to reproduce its minimum transmittance (maximum reflectance) point as precisely as possible. When comparing both techniques, magnetron sputtering shows a higher fidelity to the simulations than thermal evaporation in this respect, with the difference in transmittance between the measurements and simulations at the minimum point being 2.1% and 6.2% for magnetron sputtering and thermal

evaporation, respectively. Another important consideration is the difference between the simulated and measured results with respect to the wavelength at the minimum transmittance point. Here, the evaporated sample better matches the simulation than the sputtered one does. However, this result should be analysed in a complete multilayer stack since such a shift might be wavelength dependent.

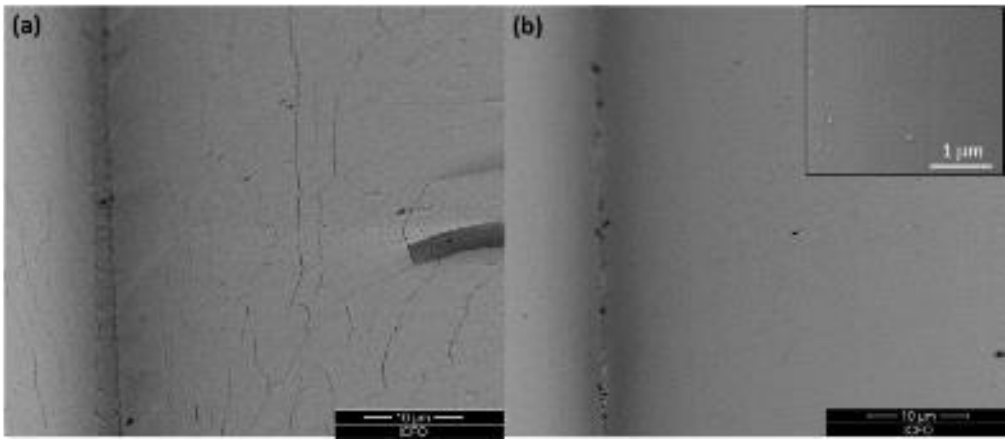

Figure 3.9 SEM images of a multilayer deposited by (a) thermal evaporation and (b) magnetron sputtering. The inset shows a higher magnification where no small cracks can be seen.

The morphology of the deposited layers was analysed through optical and scanning electron microscopy. After SEM inspection, it could be seen that the thermal evaporated samples had cracked at the h-CPP surface, as shown in Figure 3.9. Moreover, an evaporated sample, despite having no cracks when observed under the optical microscope directly after fabrication, then showed cracks with the optical microscope after being observed under the SEM. This can be seen in Figure 3.10. The cause of the surface cracking seems to be the pressure gradient over the samples during the vacuum process of the chamber during SEM examination. As previously highlighted, evaporated layers may suffer from a certain lack of adhesion that could promote cracking under certain stress, such as rapid pressure changes. This experiment demonstrates a considerable brittleness

in the evaporated samples, and suggests that, if samples were to be fabricated through thermal evaporation, they should be deposited continuously, without venting the chamber until they are finished. However, this could complicate the fabrication process when material sources need to be refilled, and also when some characterisation is required prior to processing the final structure

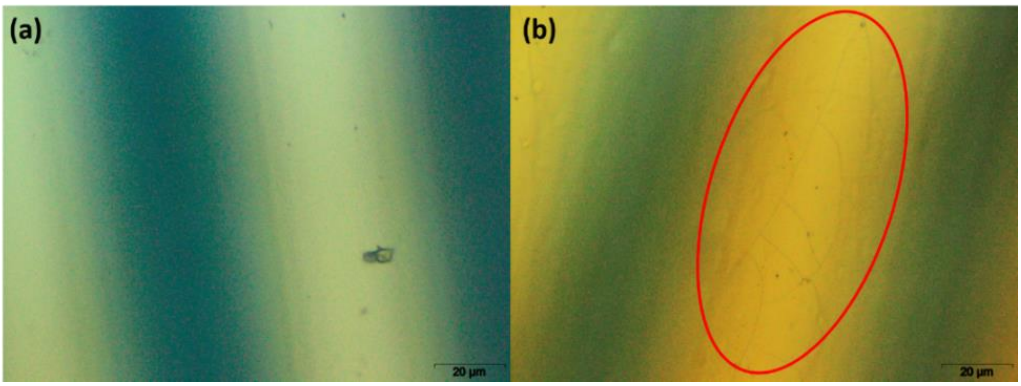

Figure 3.10 Optical microscope images of the h-CPP surface with a thermally evaporated stack deposited on top (a) before and (b) after being exposed to a vacuum process (SEM chamber). Small cracks can be seen in the area within the red oval.

Since the layers need to be deposited following the h-CPP pattern, it is important that the deposition and thickness are homogeneous. For this reason, a cross view SEM inspection was performed on a more complex multilayer stack. Figure 3.11 depicts a complete multilayer structure sputtered on an h-CPP, showing the different layers deposited following the pattern geometry, with their thicknesses remaining constant at different points on the half-cylinder.

Having considered the results of both types of characterisation, we decided to fabricate the final structure using magnetron sputtering deposition. Although this technique requires more deposition time due to its slower deposition rate, it seems to be more reliable with regard to the stiffness of the structure during and after deposition of the materials. As previously discussed, given the materials that will be employed, an inverse design approach was applied in order to find the

best solution for a multilayer structure, i.e., one that offers the best polarising performance for the RGB range. Different multilayer polarising stacks can be obtained depending on the number of layers of the structure, and this is directly related to the degree of light polarisation. However, as demonstrated in Figure 3.2, there is a maximum number of layers after which there is no significant increase in the polarisation ratio by adding more layers.

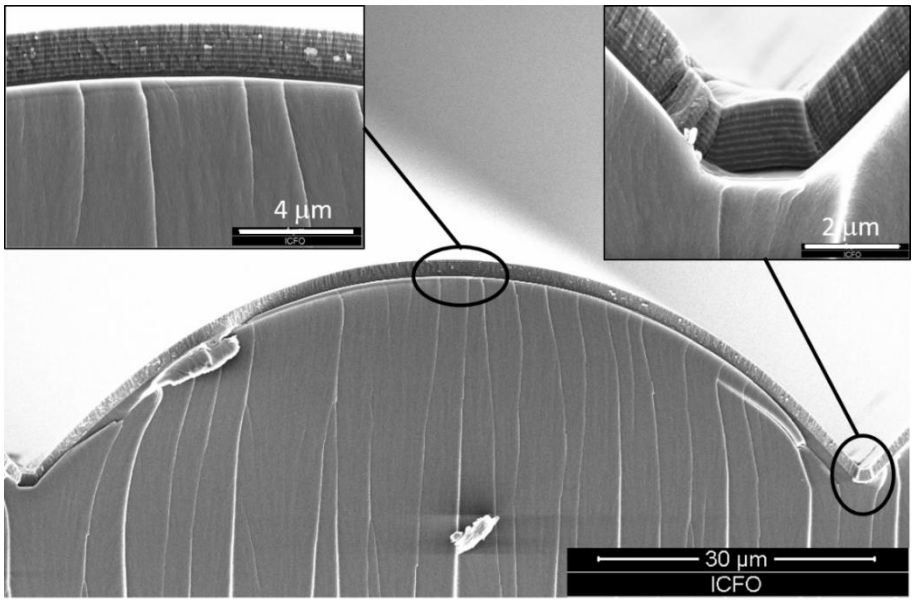

Figure 3.11 SEM image of the cross section of a complete multilayer structure on top of an h-CPP.

3.3.3 Polarised transmittance and recycling of light into electricity with the integration of perovskite solar cells

15 layers were deposited through magnetron sputtering, while attempting to match the thicknesses provided by the inverse design solution. As with the 5-layer structure discussed in Section 3.3.2, during the deposition process of the polarising multilayer, a flat substrate was included together with the h-CPP in order to characterise the thickness of each of the layers by ellipsometry. The

thickness of each layer within the stack are included in Appendix A.3. Figure 3.12 shows the different transmittance values measured on the flat glass substrate for the two polarisation modes at different angles of incidence. These measurements are compared with a simulation, replicating the same structure with the layer thicknesses obtained by ellipsometry, and the match in the range of interest is particularly good, confirming that the thicknesses obtained for the flat sample were correctly characterised.

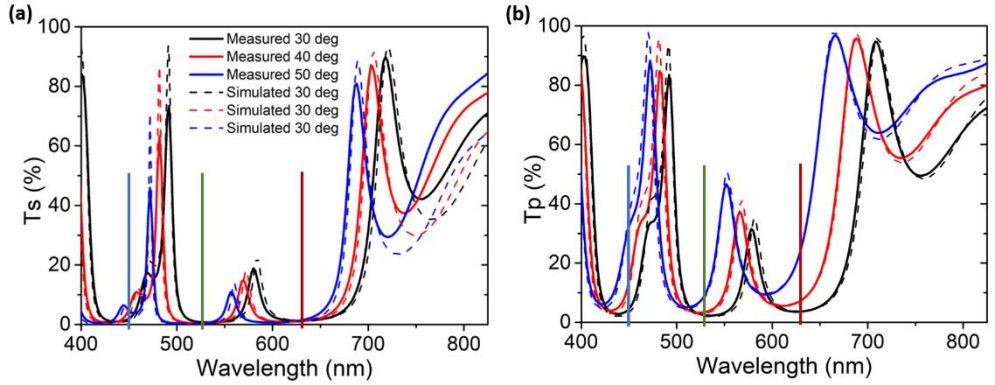

Figure 3.12 Simulated and measured (a) Ts and (b) Tp of the multilayer polarising structure deposited on flat substrates for different angles of incidence (30°, 40° and 50°). The coloured bars indicate the wavelengths for which the structure was designed to operate.

Next, in order to optically study the polarising multilayer on the h-CPP, we measured the total transmittance of this sample when illuminated from its glass face at normal incidence and compared this to the equivalent simulated structure. Figure 3.13 shows the spectra of the measurement in the integrating sphere, together with its corresponding simulation. The simulated spectrum of the s-polarised transmittance shows minima close to 0% at the RGB wavelengths while the p-polarisation mode shows certain transmittance. In the experimental measurements, the general trend for the spectrum follows that obtained in the simulation. The Ts at the λ_B and λ_G is close to the minimum (~8%), which

represents a good sample for polarising and reflecting light. However, the Ts at the λ_R is higher than we expected. The results of this characterisation represent an average of the transmittances for the different angles of incidence that occur when the light is perpendicularly incident to the sample. Therefore, the mismatch of the spectra may be related to a small inhomogeneity deposition over the different points of the half-cylinders, which may occur due to the effect of the deposition on the corrugated surface from two different tilted sources. This small inhomogeneity can become relevant when several layers are deposited, affecting the averaged transmittance. The Tp and Ts values of both simulated and experimental polarising structures are presented in Table 3.3.

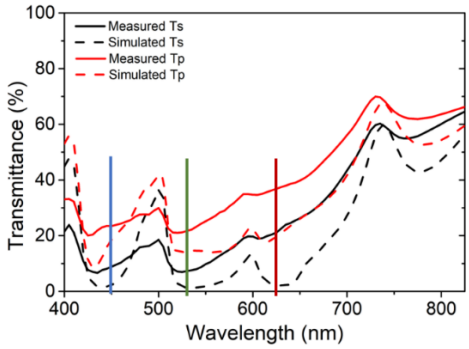

Figure 3.13 Simulated and measured total transmittance of a multilayer polarising structure deposited on an h-CPP. The coloured bars indicate the wavelengths for which the structure was designed to operate.

Table 3.3 Simulated and experimental s- and p-polarised total transmittance for a 15-layer multilayer polarising structure on an h-CPP at normal light incidence.

	Wavelength (nm)	Ts (%)	Tp (%)	Tp/Ts ratio
Simulation	450	2.1	18.6	8.7
	532	1.3	14.5	11.2
	635	2.2	22.2	10.1
Experimental	450	8.9	23.4	2.6
	532	7.4	22	3
	635	24	37	1.5

To prove the ability of such a design to recycle light, two types of characterisation were performed. First, a perovskite device was illuminated by three different low power light sources corresponding to the RGB wavelengths, as described in Appendix B. The light emitted by the sources was focused to achieve a similar light intensity to the illumination from one sun (100 mW/cm^2). Figure 3.14a shows the J-V curves and PV parameters of a perovskite solar cell under each of the chromatic sources. As shown in Figure 3.14b, a solar cell under this type of illumination demonstrates a high PCE due to the high EQE of the device at the sources' wavelengths. This is why the PCE of the solar cell under the illumination of chromatic sources is higher than that obtained under simulated sunlight. Some small differences related to the V_{oc} and the FF were found between the performances under both types of illumination, which may be due to the smaller area of illumination relative to the size of the solar cell (0.24 cm^2), creating "shadow" effects, as has been previously reported.[156]

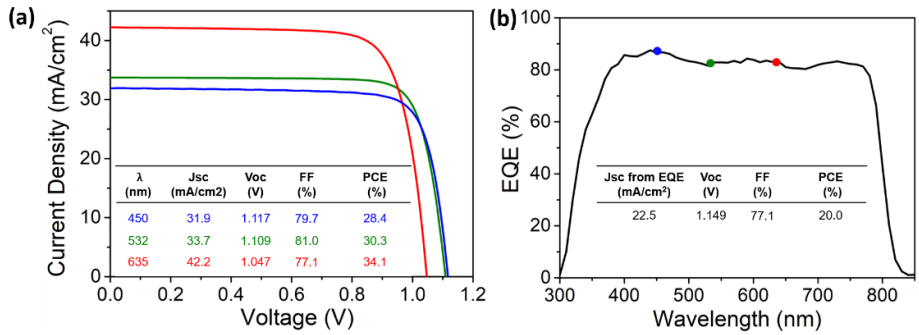

Figure 3.14 (a) J-V curves together with the PV parameters of a perovskite solar cell under RGB direct illumination. (b) EQE and PV parameters of the solar cell under sunlight illumination. The coloured dots represent the point in the EQE for the RGB wavelengths.

The next step was to confirm the polarisation effect of the structure by observing the relative amount of light recycled into electricity depending on the light polarisation. To do so, the different elements (polarising h-CPP, silver

reflector and perovskite solar cell) were mounted together and the light was directed into the ensemble through a small light window on the reflector, as shown in Figure 3.15. Polarised light (far enough from the edge to ensure ergodic light propagated conditions) entered the ensemble, and the electrical current generated by the different light sources and polarisation modes in the solar cell was measured. Given the low power of the light sources tested, we decided to consider the current ratio (Is/Ip), which is included in Table 3.4, to analyse the light recycling capability regarding the polarisation dependence of the ensemble. The intensity ratio provided by the three different chromatic illumination sources confirms that our design is able to guide the non-transmitted light, which is predominantly composed of s-polarisation light, to the edges where solar cells are placed.

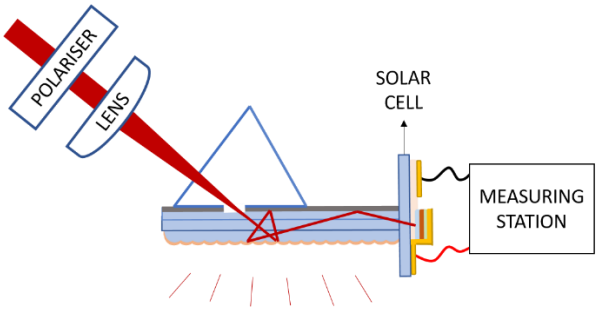

Figure 3.15 Diagram of the light recycling ensemble and the set-up for its PV characterisation.

Table 3.4 Intensity ratio of the current provided by the perovskite solar cell when polarised light enters the ensemble

	450 nm	**532 nm**	**635 nm**
Is/Ip	1.93	2.92	1.99

Due to the high performance of a perovskite solar cell when it is illuminated by chromatic light, the recycling of light into electricity is expected to be very efficient once the light is collected by the PV devices. To confirm this, we measured the PV parameters through the J-V curves using a high-power green source when the s- and p-polarised light had been inserted (Figure 3.16). Here, we again introduced sufficient light to study the perovskite solar cells under the equivalent of approximately 1 sun of irradiance. This is in the order of the minimum light intensity that would reach the solar cells when taking into consideration the hypothetical illumination area once they were applied to common LCDs for mobile phone applications.[14,143] As demonstrated in Figure 3.16, the ratio for the J_{sc} between the s- and p-polarisation (2.85) is very similar to that obtained for the low intensity light source presented in Table 3.4, which confirms that such a parameter is independent of the light intensity reaching the cell. Also, the solar cell performance in a light recycling design is very similar to that obtained under normal incidence monochromatic illumination. Slightly lower V_{oc} and FF were observed, which could be explained by the inhomogeneity in the illumination intensity on the solar cell illuminated area caused by the projection of the beam from the laser on the cell surface. However, the V_{oc} in real applications may be increased due to the higher illumination intensity on the perovskite solar cell.

These results prove that our design has the ability to effectively guide the non-transmitted light to the sides of the light guiding ensemble, where the perovskite solar cells would efficiently collect and recycle it into electricity.

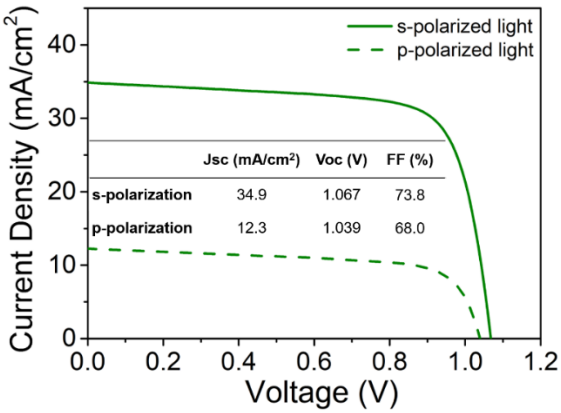

Figure 3.16 J-V curves and parameters of the perovskite solar cell after integration on the ensemble for s- and p-polarised green light.

3.4 Conclusions

In order to create energy efficient devices, the correct management of light in opto-electronic designs must always be considered so as to avoid unnecessary losses and energy wastage during usage. To this end, perovskite solar cells can act as light recycling elements and, in combination with an appropriate optical design, collect the light that enters the device but does not contribute to its operation, and would otherwise be wasted.

In this chapter, we have presented the design and application of a modified h-CPP, in which RGB unpolarised light, when properly directed into the device, is evenly dispersed in the photonic plate and selectively emitted, in order that polarised light is transmitted through its top surface. The device allows the non-transmitted light to be collected by lateral perovskite solar cells, which then recycle it into electricity thanks to the reflective broadband type of polarising mechanism and the negligible absorption of the reflector. Given the amount of light that is often wasted in LCDs, such a design seems to be perfectly suited to

such applications, to reduce their energy consumption and make them more energy efficient.

The fabrication of a similar structure was carried out to experimentally demonstrate the polarisation and recycling of light. In order to match the simulated results with higher fidelity, further work is required to optimise the deposition of the polarising structure. Nevertheless, the fabricated device demonstrated a positive polarisation effect and the ability to generate electricity with a light polarisation dependency, as expected. In fact, the perovskite PV devices performed extremely well under monochromatic illumination, which confirms their suitability for the proposed application. Furthermore, the efficient recycling of light into electricity could potentially be improved by adjusting the bandgap of the perovskite material towards the lowest energy level of the chromatic light that it would absorb during operation, i.e., in the red spectrum.

The proposed design could be used to enhance the performance of LCDs by decreasing the losses that currently occur in standard device designs. In addition, this type of light management system may attract industrial interest when applying PV devices to opto-electronic applications, by helping to avoid light dissipation and increasing energy efficiency during operation.

Chapter 4

Fabrication of Low Temperature Perovskite Solar Cells Using a Bi-Layered Nanoparticle Electron Transport Structure

As indicated in Chapter 1, energy efficiency during operation must also be complemented by energy efficient fabrication processes. To increase the energy efficiency during the fabrication of perovskite solar cells of any kind, it is essential to avoid high temperature processes. However, the ability to do this is typically limited by the application of high-temperature compact and mesoporous TiO_2. In order to find compatible materials involving low temperature processes that perform similarly to high temperature TiO_2 structures, the employment of dispersed nanoparticles has been studied. Unfortunately, this type of ETL may sometimes not perform as well as expected and needs to be functionalised or passivated.[157–159] When band alignment is correctly applied, the combination of an ETL with an extra n-type material has proven to be a good strategy to enhance the performance of a single ETM. [160–163] However, many of these combinations still require high temperature annealing or other processing techniques, such as acidic post-treatment procedures, which limit their application for cost-effective and large-scale manufacture, particularly when considering energy efficient fabrication.

In this chapter, we present an improved strategy for the fabrication of low temperature perovskite devices, thereby increasing their energy efficiency. We study SnO_2 and TiO_2 nanoparticles as the ETMs for this type of solar cells, and together with the characterisation of the layers and their effect on the perovskite film, we analyse the performance of the devices when a TiO_2 layer, an SnO_2 layer and an SnO_2/TiO_2 bilayer are applied. Combining these two materials is shown to be key in enhancing the performance of low temperature devices with extra thin active films, as in energy efficient semi-transparent perovskite solar cells.

4.1 SnO_2/TiO_2 nanoparticulated bi-layer as an efficient ETM

4.1.1 ETL and perovskite morphological study

We start by analysing the morphology corresponding to the different ETL configurations studied, namely SnO_2 and TiO_2 monolayers and SnO_2/TiO_2 bilayers (all made of nanoparticles), and their possible impact on the subsequent active layer growth. Atomic force microscopy (AFM) images corresponding to the different thin nanoparticulated layers, as well as top view SEM images of perovskite films deposited on top, are presented in Figure 4.1. From the AFM images (Figures 4.1a-c) it seems clear that, although SnO_2 and TiO_2 suspensions of about the same particle sizes were used, the former yielded a more uniform and compact film when compared to the more porous sponge-like texture of the latter. Interestingly, the structural characteristics of the perovskite layers (Figures 4.1d-f) were also quite dissimilar in both cases. Whereas the formation of a polycrystalline material with clear individual grains could be inferred in the case of SnO_2, when differentiating the grain boundaries of the perovskite material with

a TiO_2 underneath layer, the results were less evident. Nonetheless, when we considered the SnO_2/TiO_2 bilayer, the perovskite morphology showed remarkably similar features to those exhibited by the single TiO_2 coating. These results suggest that the interface underlying the perovskite material may have a significant influence on its morphological characteristics. It is important to mention that exactly the same procedure was carried out for the perovskite deposition in order to avoid any undesired variation due to experimental conditions. Also, to ensure a good coverage of the perovskite layer, a mixed halide perovskite solution with a high concentration (35 wt%) was prepared following the recipe reported by M. Lee et al.[164]

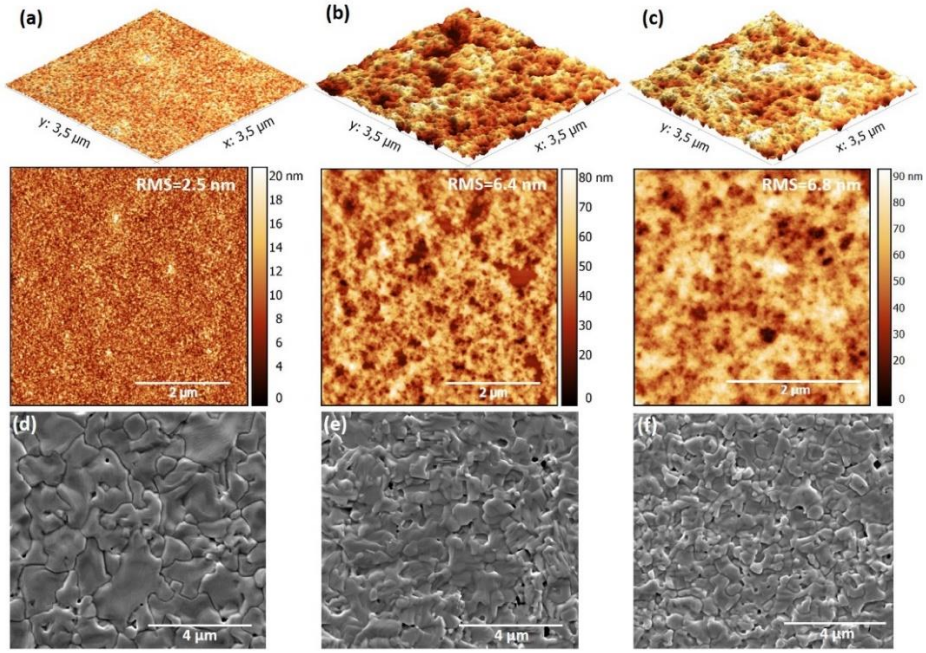

Figure 4.1 (a-c) AFM images corresponding to SnO_2, TiO_2 and SnO_2/TiO_2 nanoparticle layers, respectively. The sizes of the SnO_2 and TiO_2 nanoparticles are 10 nm and 4-8 nm, respectively. (d-f) Top view SEM images displaying the different morphologies of perovskite layers when deposited on top of SnO_2, TiO_2 and SnO_2/TiO_2 nanoparticle layers, respectively.

4.1.2 Photovoltaic performance of perovskite solar cells

Planar perovskite solar cells containing the different ETL combinations, either in monolayer or bilayer form, were then fabricated following the schematic diagram depicted in Figure 4.2a. Note that we only considered an SnO_2/TiO_2 bilayer due to the favourable energy band alignment between the corresponding conduction band of the inorganic oxides and the perovskite. In all cases, poly[bis(4-phenyl)(2,4,6-trimethylphenyl)amine] (PTAA) polymer was chosen as the p-type material. The thicknesses measured for the fully spin-coated n-i-p stack displaying the best PV characteristics were 25 nm, 40 nm, 280 nm and 70 nm for the SnO_2, TiO_2, perovskite and PTAA layers, respectively. When the single ETL alternatives were considered, the optimal thicknesses after experimental analysis were found to correspond to the values indicated above, i.e., 25 nm for SnO_2 and 40 nm for TiO_2.

Figure 4.2b shows the typical J-V curves measured for perovskite solar cells, integrating the different ETL combinations and displaying their PV parameters among the attained average values. As it can be seen, the double ETL exhibited slightly higher J_{sc} and FF values when compared to the single TiO_2 layer, thus giving rise to the best PV behaviour. Conversely, the SnO_2 ETL-based cells showed the worst performance, mainly due to their lower FF values. The PV parameters extracted from the different J-V curves, which are also summarised in Table 4.1 for comparison purposes, yielded overall efficiencies of 14.9%, 14.2% and 8.6% for the SnO_2/TiO_2, TiO_2 and SnO_2 nanoparticle ETLs, respectively. The experimental details employed for the measurements can be found in Appendix B. The results obtained for the double ETL architecture might be explained as a consequence of the more effective charge transport and extraction processes caused by the more suitable energy band matching and the

higher electron mobility of SnO_2, as suggested elsewhere.[160,165,166] Besides, charge recombination taking place at the SnO_2/perovskite interface or at the grain boundaries of the absorbing material might be responsible for the lower performance of solar cells with only SnO_2 as ETL, which is in good agreement with previous works.[167] Studying charge transport dynamics of the proposed device configuration in order to clarify the origin of the obtained results remains as one of the major challenges for future work.

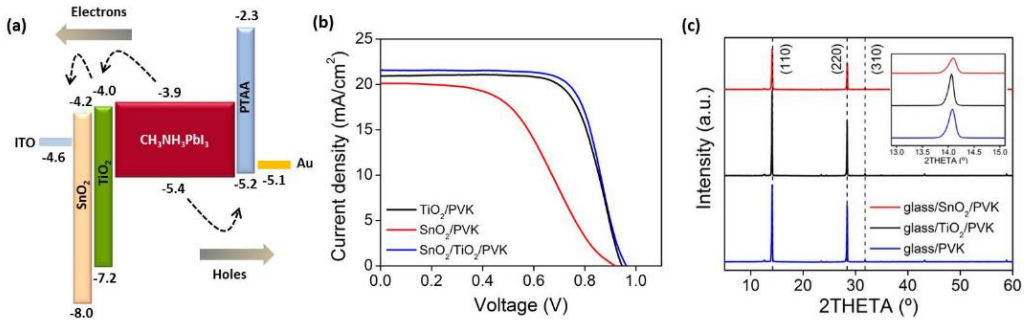

Figure 4.2 (a) Scheme of energy levels for the different layers constituting the fabricated device. (b) J-V curves corresponding to perovskite solar cells, displaying their PV parameters among the attained average values for the different ETL combinations: SnO_2, TiO_2, and SnO_2/TiO_2. (c) XRD patterns for a 280 nm thick perovskite layer deposited on a bare glass substrate, TiO_2 and SnO_2 nanoparticles.

Table 4.1 PV parameters of the perovskite solar cells selected as representative of the average values integrating the single and double nanoparticle ETLs.

ETL Configuration	J_{sc} (mA/cm^2)	V_{oc} (V)	FF (%)	PCE (%)
TiO_2	20.9	0.95	71	14.2
SnO_2	20.1	0.93	46	8.6
SnO_2/TiO_2	21.7	0.97	71	14.9

The X ray diffraction (XRD) patterns of perovskite layers grown on different types of substrates, mainly bare glass and SnO_2 or TiO_2 coated glass, are depicted

in Figure 4.2c. Although almost the same diffraction pattern is observed for the whole set, the different peak intensity may evidence a preferred orientation in the case of the underlying nanoparticle TiO_2 layer when compared to that of the nanoparticle SnO_2. From the inset graph in Figure 4.2c, a slight shift in the diffraction peak is also detected for the perovskite grown on SnO_2 nanoparticles, with a concomitant broadening of the peak that may be attributed, in principle, to the presence of smaller crystal sizes. These results support the conclusion that both the nature and the morphological features of the ETL play a crucial role in determining the characteristics of the perovskite material and, hence, the cell performance.

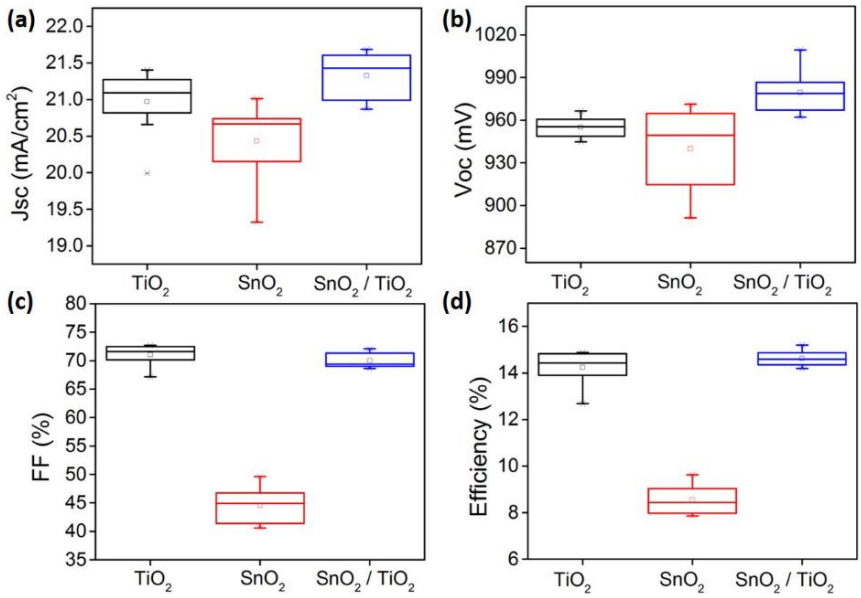

Figure 4.3 (a) Jsc, (b) Voc, (c) FF and (d) efficiency statistical analysis of perovskite solar cells fabricated using different ETL combinations, namely SnO_2 and TiO_2 monolayers and SnO_2/TiO_2 bilayer.

In order to statistically analyse the results obtained for the set of fabricated devices, box plot diagrams of the PV parameter distribution are presented in Figures 4.3a-d. In general, narrower dispersions in the parameters were obtained

for the devices that included TiO_2 and SnO_2/TiO_2 as the ETLs. In the latter case, we also identified both a slightly higher J_{sc} and a significantly larger V_{oc} relative to the single ETL designs. In fact, the maximum values of J_{sc} and V_{oc} reached for the double ETL architecture were about 0.3-0.7 mA/cm^2 and 40-50 mV higher than those obtained for the single ETLs. Moreover, the maximum efficiency was boosted to 15.2% for the SnO_2/TiO_2 ETL, as opposed to only around 14.9% and 9.6% for the single TiO_2 and SnO_2 layers, respectively. Beyond these findings, these results suggest that completely nanoparticulated systems processed at low temperatures may offer an easy and low-cost and energy efficient route for ETL engineering in perovskite solar cells.

4.2 SnO_2/TiO_2 bilayer suitability for thin film and semi-transparent perovskite solar cells

4.2.1 Thickness dependence on perovskite film continuity

To evaluate the influence of the extent of ITO coverage provided by the TiO_2 and the SnO_2/TiO_2 ETLs due to the different levels of compactness of the nanoparticle coatings, we also prepared a set of semi-transparent perovskite solar cells with the device configuration shown in Figure 4.4a. Non-continuous active layer morphology with a large absorber-free area is usually attained as the perovskite thickness is reduced. This aspect is fundamental to modifying the transparency of the cell at will, but can also lead to shunting paths that will reduce its performance.[168–171] Sometimes, in order to increase transparency, incomplete coverage of the buffer layer by the perovskite material is employed, while still ensuring fair performance and reliability.[172–174] Studies based on the application of low-temperature processes compatible with semi-transparent architectures

have been reported, most of them employing p-i-n structures with PEDOT:PSS and PCBM used as the HTL and ETL, respectively.[175–177] Some other studies were based on similar structures, but including an extra layer[65,178] or replacing one of the buffer layers[179,180] to enhance performance. Surprisingly, however, it is rarely found in the bibliography studies that employ the n-i-p device structure for the fabrication of visible range semi-transparent perovskite solar cells and, in those reported, their overall performance seems to be somehow limited.[181]

In our case, as well as varying the thickness of the perovskite absorber, an ultrathin Au contact covered with a protective MoO_3 layer was deposited by thermal evaporation as the top electrode. Although alternative semi-transparent top contact layers have been reported, ranging from silver nanowires[182–184] and dielectric-metal-dielectric architectures[185,186] to metallic grids[169] and sputtered conductive oxides,[187–189] this combination ensures a reasonably good semitransparency over the visible without compromising the processing, performance and stability of the resulting devices.[190,191] The thickness of the active layer was then changed from 390 nm to 70 nm by modifying the concentration of the mixed halide perovskite solution while keeping the same deposition parameters. Even though special care was taken during the crystallisation process, the removal of excess material during the thermal annealing led to void spaces to the order of a few hundred nanometres for active layer thicknesses below 280 nm. Top view SEM images displayed in Figures 4.4c-f show the morphology of such perovskite layers, with thicknesses of 390 nm, 280 nm, 160 nm and 90 nm, respectively. Further analysis using an image processing program (ImageJ) allowed us to quantify both the extent of coverage of the perovskite films and the average size of the open voids, as presented in Figure 4.4b.

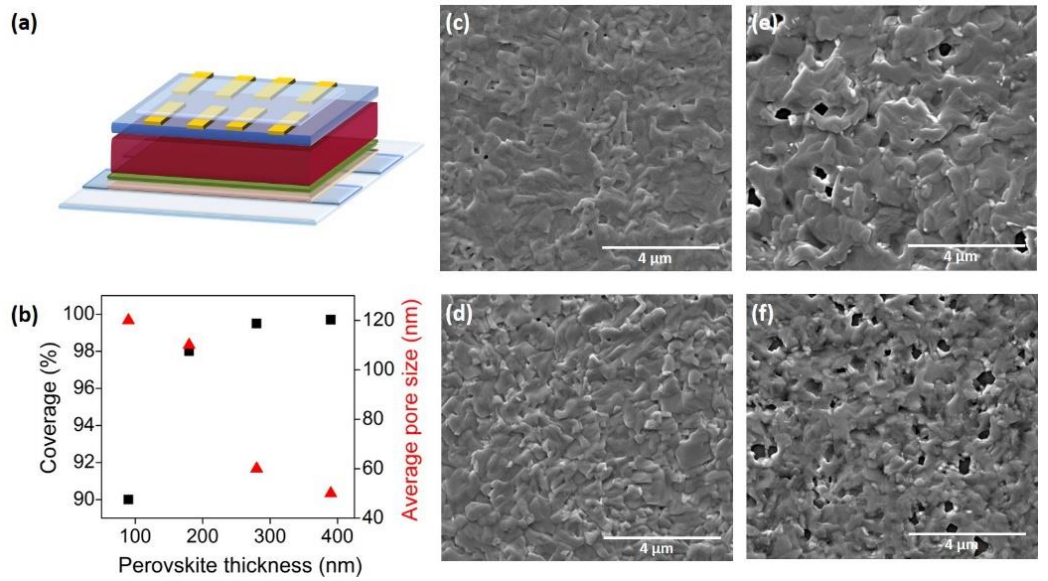

Figure 4.4 (a) Scheme of the proposed semi-transparent perovskite solar cell configuration. (b) Extent of coverage (black) and average pore size (red) estimated for the deposited perovskite layers with different thicknesses. (c-f) Top view SEM images corresponding to perovskite layers with thicknesses of 390 nm, 280 nm, 160 nm and 90 nm, respectively.

4.2.2 Photovoltaic and optical performance of semi-transparent perovskite solar cells

Figures 4.5a-b display the J-V and the EQE curves measured for the best performing semi-transparent devices based on the double layer architecture. For comparison, in Figure 4.5a we also plotted the data corresponding to solar cells based on a single TiO_2 ETL (dashed lines). We observed that, in both cases, the J_{sc} systematically increased with the active layer thickness, as expected. However, those values were higher for the double ETL architecture and, this time, the increase in the V_{oc} when compared to the single TiO_2 layer was superior as the perovskite thickness was reduced. This is good evidence of the positive properties of SnO_2 nanoparticle coatings to effectively prevent shunting paths at

the frontal ITO/perovskite interface, thus significantly suppressing charge recombination paths. Such a conclusion is also supported by the difficulty in fabricating devices with only the TiO_2 ETL and active layer thicknesses below 90 nm. In addition, the remarkable FF values preserved for the thin absorber layers allowed us to obtain efficiencies of up to 7% for a perovskite layer of 90 nm in thickness. On the other hand, cells fabricated using the highest concentration precursor led to lower FF and V_{oc} values, which may be explained by a poorer control on the homogeneity of the films when a certain thickness is exceeded for this particular perovskite composition. To verify the fact that the thickness of the nanoparticle TiO_2 layer was not limiting the cell performance, we also prepared devices with a TiO_2 thickness comparable to that of the double ETL. The overall efficiency measured in devices with a perovskite layer of 90 nm (whose representative J-V curves are also plotted in Figure 4.5c) show that a thicker TiO_2 single layer performs even worse than the standard (40 nm) TiO_2 alternative. These results support the fact that the superior performance of the double layer devices is not caused by an increase in the thickness of the ETL.

From the EQE graph shown in Figure 4.5b, we can see that maximum values close to 90% were reached for the solar cells employing perovskite layers with thicknesses of between 390 nm and 160nm. However, both the reduced perovskite thicknesses and the presence of large void spaces predominantly affected the cell responses over the longer wavelength range (500-800 nm), as easily be observed for the 160 nm thick active layer. When even thinner films with a larger distribution of non-covered surface were employed, the maximum EQE stood at around 60%, with an average at longer wavelengths of just 30%. Figure 4.6a displays the transmittance spectra measured over the visible and the NIR ranges for the multi-layered ITO/SnO_2/TiO_2/perovskite/PTAA configurations with different active layer thicknesses, together with a photo of a

complete semi-transparent cell made of a 70 nm thick perovskite layer. In order to check there was no significant optical difference in the device when the SnO_2 layer was incorporated, two different devices with the different ETL systems were analysed, as shown in Figure 4.6b.

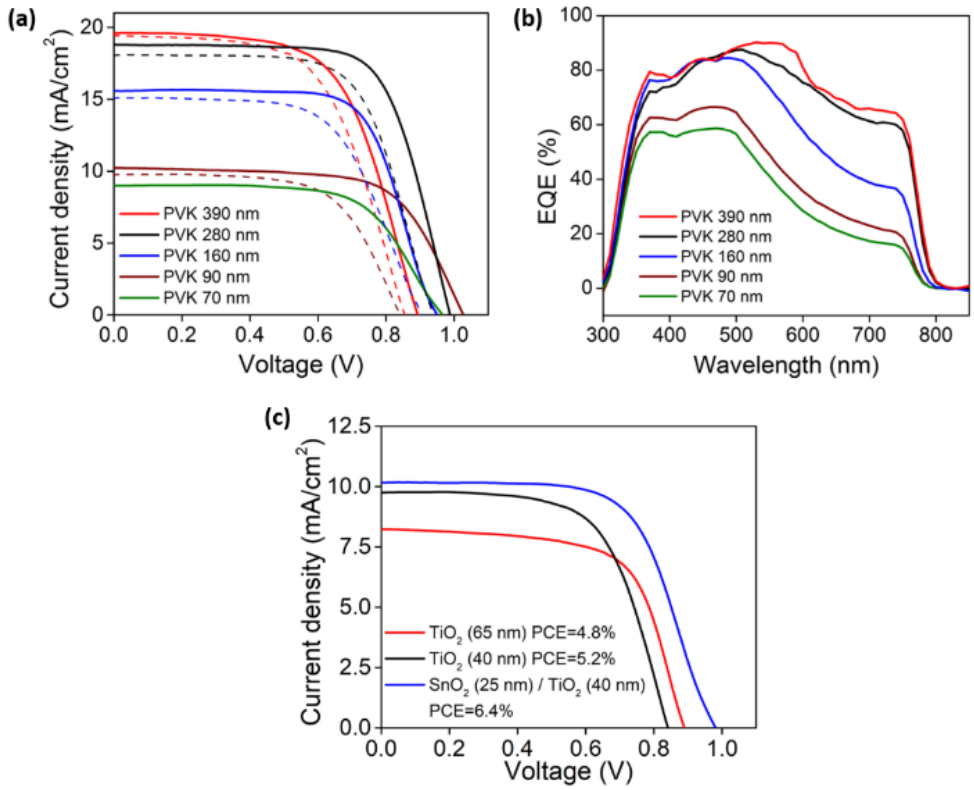

Figure 4.5 (a) J-V and (b) EQE curves corresponding to the best performing semi-transparent solar cells using different perovskite layer thicknesses. Data displayed as dashed and solid lines correspond to TiO_2 and SnO_2/TiO_2 based ETLs, respectively. (c) J-V curves corresponding to average efficiency solar cells for semi-transparent devices fabricated with a perovskite layer of 90 nm and different ETL configurations.

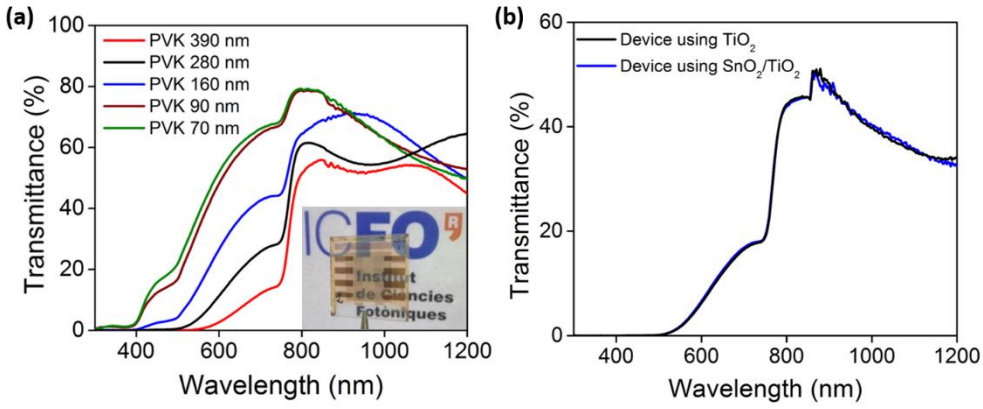

Figure 4.6. (a) Transmittance spectra acquired for the ITO/SnO_2/TiO_2/perovskite/PTAA stacks with active layers of different thicknesses. The inset shows a photo of a complete semi-transparent perovskite cell made of a 70 nm thick active layer. (b) Comparison between the transmittance of a complete device (including the electrode) using TiO_2 nanoparticles and SnO_2/TiO_2 nanoparticles as ETLs.

Table 4.2 summarises the PV parameters extracted from the J-V curves corresponding to the best performing devices, both opaque and semi-transparent. In the latter case, the resulting average transmittance (AVT) values for the visible and NIR spectrum have also been included. This is particularly relevant for applications in building integrated PV systems or silicon/perovskite tandem cells. Since, as previously demonstrated, the effect of using the double layer architecture revealed no significant influence on the optical properties when compared to the single TiO_2 ETL, the same AVT value was obtained for both configurations. As the solar cells prepared with active layer thicknesses below 90 nm and containing only the TiO_2 ETL did not work properly, the corresponding parameters are not included in Table 4.2. More detailed information related to the statistical distribution of the PV parameters obtained for the semi-transparent solar cells integrating the double ETL can be found in Figure 4.7.

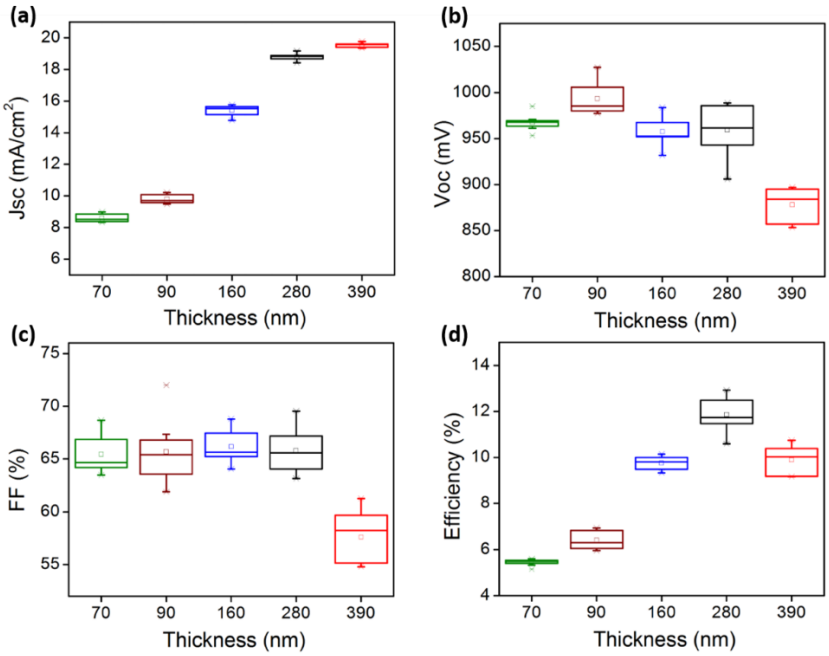

Figure 4.7 (a) Jsc, (b) Voc, (c) FF and (d) efficiency statistical analysis of semi-transparent perovskite solar cells fabricated using different perovskite layer thicknesses. All of these incorporate the SnO_2/TiO_2 bilayer configuration.

The semi-transparent solar cells were also measured when illuminated from the thin metal contact side. When compared to the results obtained when illuminated from the ITO, the decrease in the J_{sc} is less than 24% for devices of 280 nm thick perovskite layers. This decrease is similar to or even lower than that of other bifacial perovskite solar cells whose semi-transparent contact electrode is made of gold[186,192] or a different material.[193,194] Such a performance shows that devices fabricated with the configuration proposed in this chapter have a potential application as bifacial solar cells, although more work may be needed to further optimise the optoelectronic properties of the metal-dielectric contact. These results can be found in Figure 4.8 and Table 4.3.

Table 4.2 PV parameters extracted from the analysis of the J-V curves for the complete set of best fabricated devices.

ETL configuration	Active layer thickness (nm)	J_{sc} (mA/cm^2)	V_{oc} (V)	FF (%)	Efficiency (%)	AVT-vis (%)*	AVT-NIR (%)*
TiO_2	280	21.4	0.96	72.7	14.9		
SnO_2	280	20.58	0.97	48.1	9.6	OPAQUE	OPAQUE
SnO_2/TiO_2	280	21.7	0.98	71.3	15.2		
TiO_2	390	19.4	0.86	59.2	9.8	6 (5.2)	52.4 (35)
SnO_2/TiO_2	390	19.6	0.90	61.2	10.7		
TiO_2	280	18.1	0.94	65.8	11.2	12.6 (8.2)	62 (40.5)
SnO_2/TiO_2	280	18.8	0.99	69.5	12.9		
TiO_2	160	15	0.91	65.3	8.9	22.6 (12.3)	65 (40)
SnO_2/TiO_2	160	15.6	0.98	67.7	10.3		
TiO_2	90	9.7	0.85	65.5	5.4	40 (20)	64.5 (36)
SnO_2/TiO_2	90	10.2	1.03	66	6.9		
SnO_2/TiO_2	70	9	0.97	64.4	5.6	42.1 (27)	64 (39.3)

*Values in brackets correspond to the AVT data obtained for complete devices.

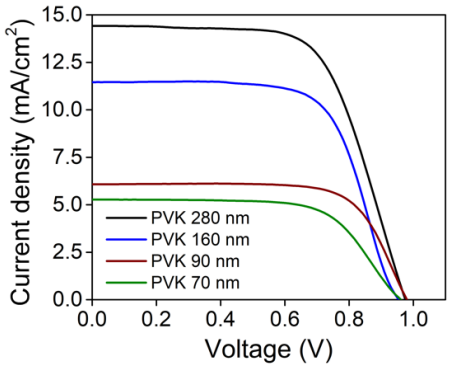

Figure 4.8 J-V curves corresponding to the best performing devices illuminated from the thin metal contact electrode.

Table 4.3 PV parameters of different active layer devices illuminated from the metal-dielectric and from the transparent (ITO) electrode.

Active Layer Thickness (nm)	Illumination side	J_{sc} (mA/cm^2)	V_{oc} (V)	FF (%)	Efficiency (%)
280	Metal-dielectric	14.4	0.98	65	9.1
	ITO	18.8	0.99	69.5	12.9
160	Metal-dielectric	11.5	0.96	66	7.3
	ITO	15.6	0.98	67.7	10.3
90	Metal-dielectric	6.1	0.98	71	4.3
	ITO	10.2	1.03	66	6.9
70	Metal-dielectric	5.3	0.96	65	3.3
	ITO	9	0.97	64.4	5.6

4.3 Conclusions

With the aim of approaching energy efficiency during the fabrication of perovskite solar cells, in this chapter we have demonstrated the application of two different nanoparticle layers processed at 150 °C, both of which act as an efficient ETM for perovskite solar cells, especially in devices with extra thin active films. The nanoparticles bilayer is made of a first layer of SnO_2 nanoparticles and a second of TiO_2 nanoparticles, which function as an improved electron transport structure for low temperature perovskite solar cells. Thanks to this strategy, a fabrication route for better-performing perovskite solar cells using low energy intensive manufacture process has been demonstrated. The application of this strategy in semi-transparent perovskite solar cells, where the

active layer is thinner than in standard opaque solar cells, was established to be more reliable than in the fabrication of devices containing only TiO_2 nanoparticles, achieving an increase of up to a 30% in the PCE for the bilayer configuration. By avoiding the creation of shunting paths and improving charge extraction, the application of the SnO_2/TiO_2 nanoparticles bilayer is a proven effective approach in the fabrication of energy efficient n-i-p semi-transparent perovskite solar cells that also present good bifacial performance.

Conclusions

In this thesis, we have studied paths to achieve an optimal light harvesting in perovskite solar cells, as well as to approach energy efficiency during fabrication and through their application. Experimental work and optical simulations have been combined to support these types of solar cells as cutting-edge PVs suitable for natural and artificial light applications. The results prove that perovskites combined with specific optical and material strategies provide effective light to electricity conversion while improving energy efficiency.

In Chapter 2, we introduced a simple periodic structure able to disperse light similarly to a randomly textured surface, obtaining ergodic light propagation within its boundaries. This pattern was effectively used experimentally as a light trapping structure, and when applied to the light entering surface of a perovskite solar cell, it enhanced the light harvesting ability of the cell to values close to the relative maximum achievable when employing a corrugated surface on a solar cell. This strategy could act as a mechanism to considerably reduce the Pb necessary in perovskite solar cells, since 30% less material can be employed to fabricate a solar cell with equal electrical performance.

The same periodic configuration was used in Chapter 3 to act as a light guiding structure in an innovative design able to emit polarised light, while avoiding the wasteful dissipation of the non-transmitted light. The design is able to achieve an optimal energy efficiency for polarised light at three different wavelengths corresponding to the blue, green and red spectra. The incorporation of a reflective polarising structure on the top corrugated surface, together with two perovskite solar cells on the sides of the periodic array, allow for the

recycling of non-transmitted light into electricity. After providing the optimal design for the polarising structure, a similar design was fabricated, experimentally proving the polarising effect, and the ability to recycle light into electricity. This novel design to polarise light is particularly interesting with regard to increasing the energy efficiency in optoelectronic devices such as LCDs.

Finally, in Chapter 4, the concept of energy efficiency was approached with regard to the fabrication of the perovskite solar cells. Using SnO_2 and TiO_2 nanoparticles as electron transport materials, it was possible to employ low temperatures for the fabrication of the electron transport layer, and, therefore, for the entire device. The deposition of a TiO_2 nanoparticle layer on top of one made of SnO_2 nanoparticles acted as an efficient electron transport structure, especially in thin perovskite solar cells such as those used in semi-transparent devices. The efficiency of such solar cells was enhanced by up to 30% compared to those using only TiO_2 nanoparticles. These results confirm that such a strategy could be employed for the low temperature fabrication process of these cells, thereby increasing energy efficiency during the fabrication of enhanced perovskite devices.

Appendix A Refractive index and multilayers configuration

A.1 Refractive index for perovskite solar cell layers

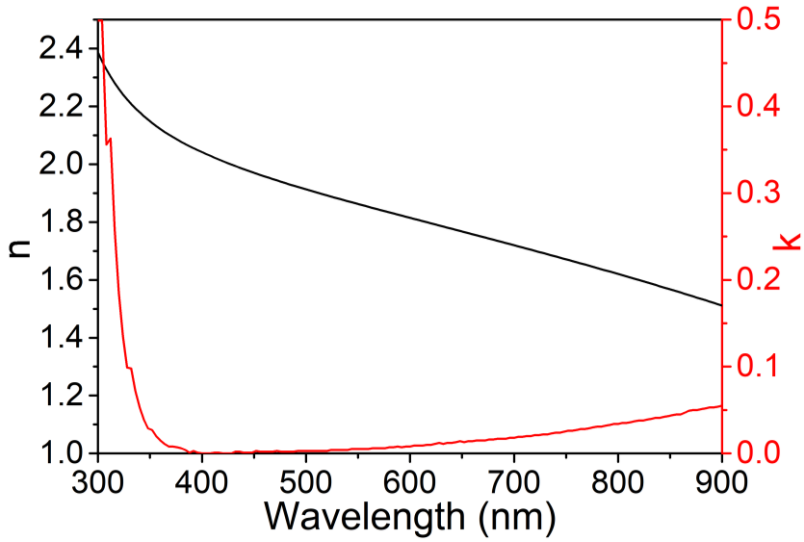

Figure A.1 n and k coefficients of ITO.

A.1 Refractive index for perovskite solar cell layers

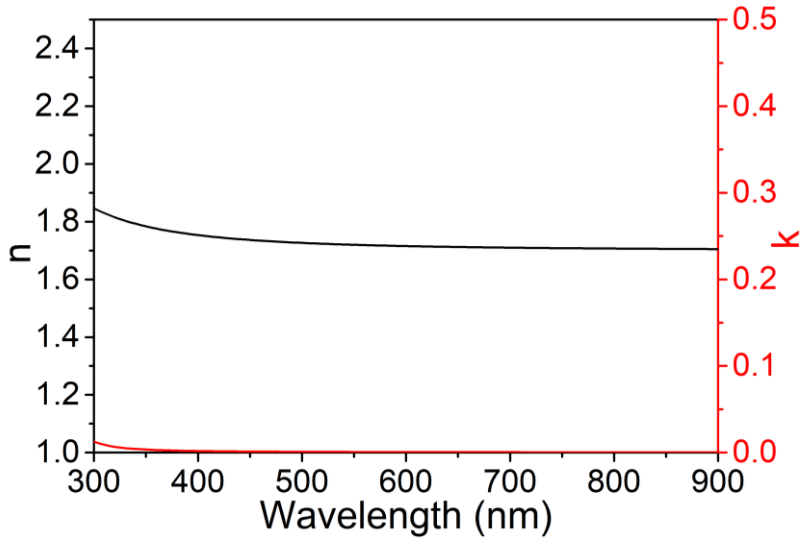

Figure A.2 n and k coefficients of SnO_2 nanoparticles.

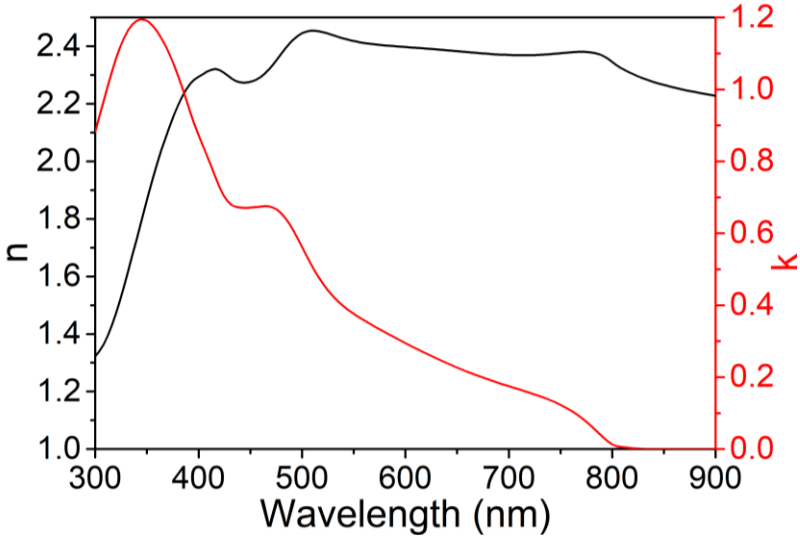

Figure A.3 n and k coefficients of perovskite $(FAI)_x(MABr)_{1-x}PbI_2$.

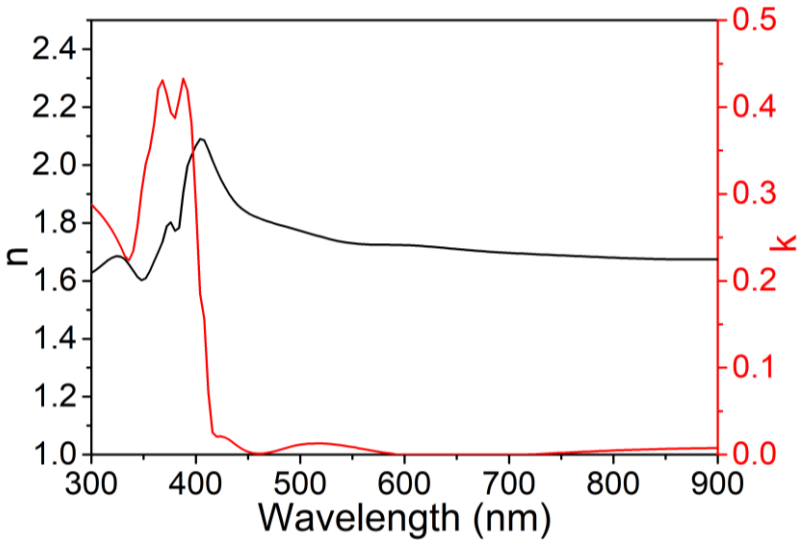

Figure A.4 n and k coefficients of Spiro-OMeTAD.

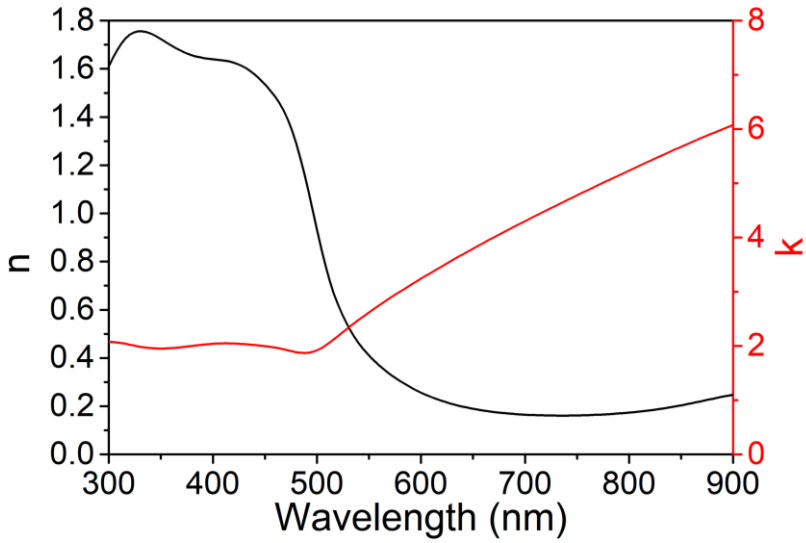

Figure A.5 n and k coefficients of evaporated Au.

A.2 Refractive index for the polarising and reflective structures

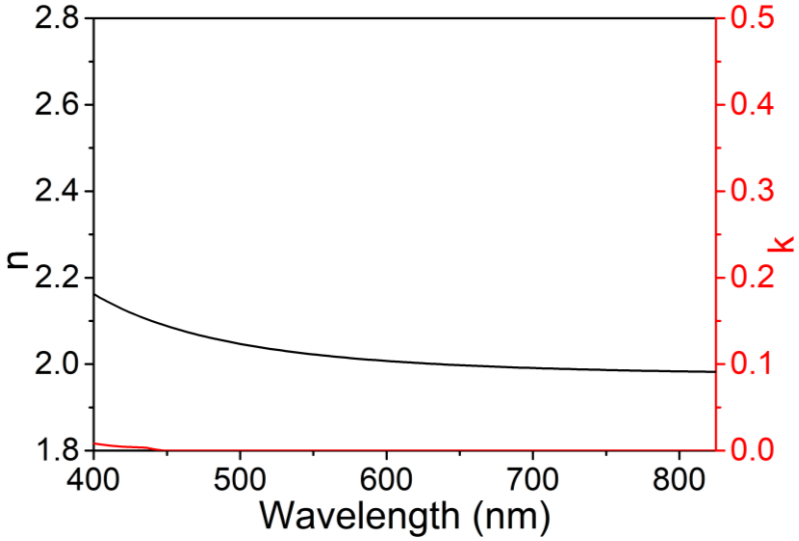

Figure A.6 n and k coefficients of evaporated WO_3.

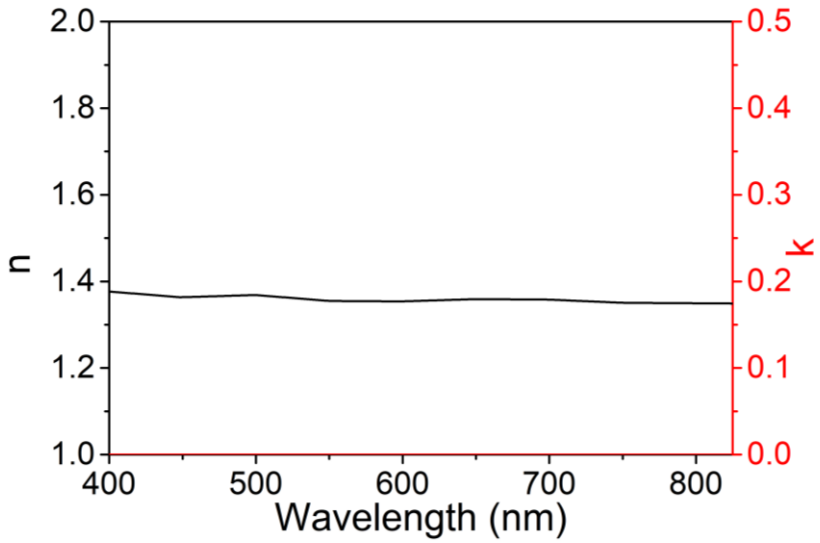

Figure A.7 n and k coefficients of evaporated LiF

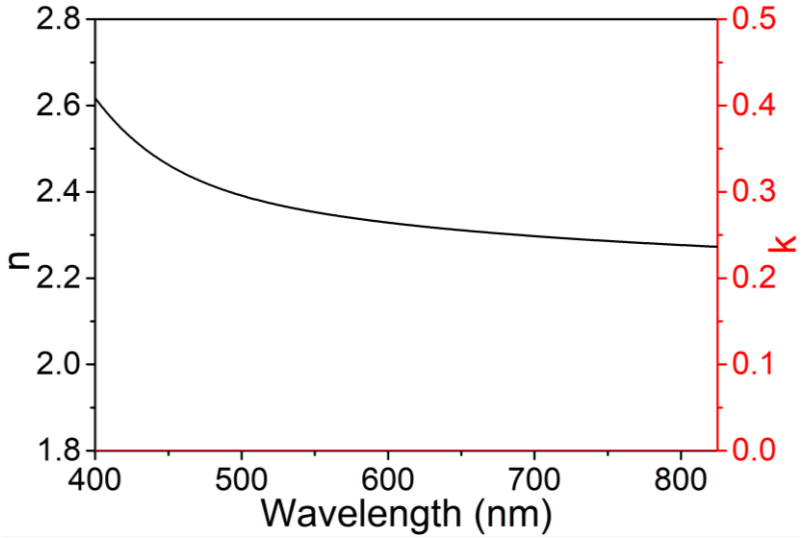

Figure A.8 n and k coefficients of sputtered TiO_2.

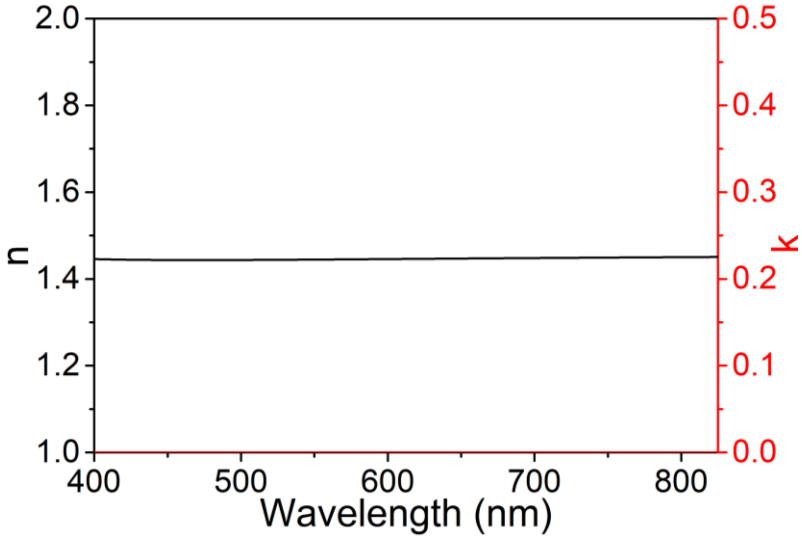

Figure A.9 n and k coefficients of sputtered SiO_2.

A.2 Refractive index for the polarising and reflective structures

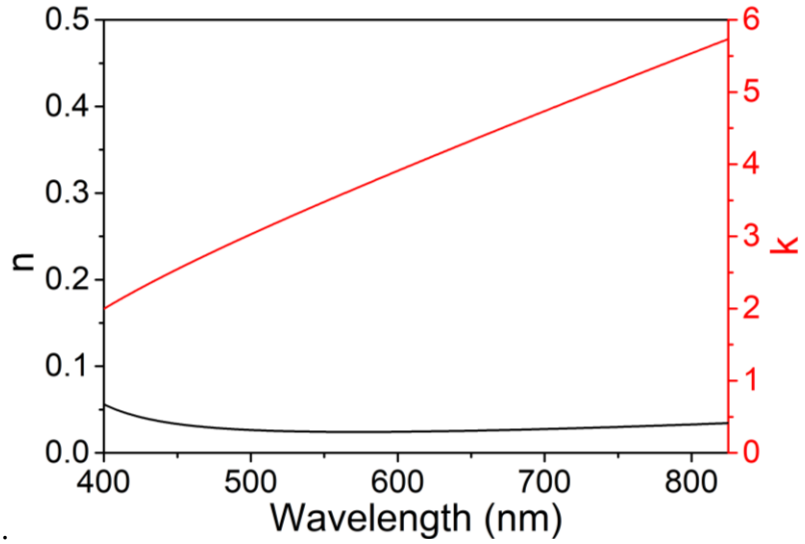

Figure A.10 n and k coefficients of evaporated Ag

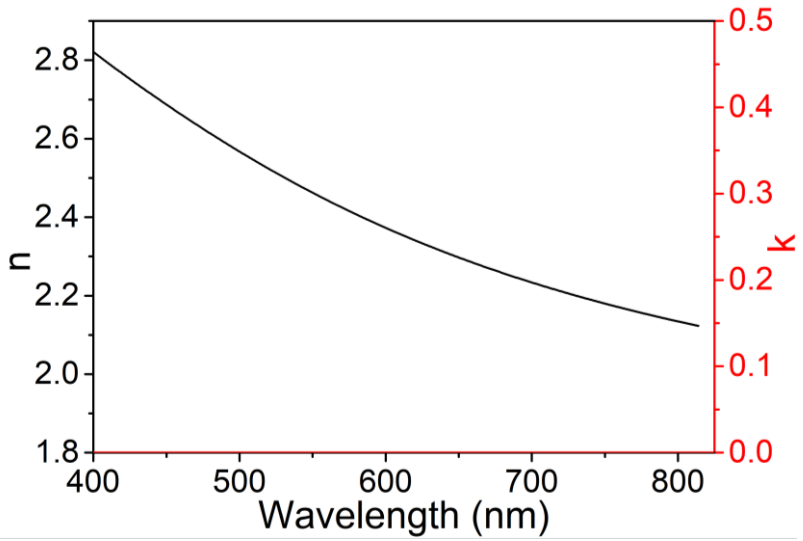

Figure A.11 n and k coefficients of TiO_2 last layer on the multilayer stack

A.3 Configuration of the multilayer structures.

Table A.1 Configuration of the low loss reflecting structure (Bragg reflector + Ag layer).

Layer #	Material	Thickness (nm)
Substrate		
1	TiO_2	64
2	SiO_2	231
3	TiO_2	166
4	SiO_2	70
5	TiO_2	116
6	SiO_2	108
7	TiO_2	57
8	SiO_2	71
9	Ag	150

Table A.2 Configuration of the polarising structure made of 29 alternating layers of WO_3 and LiF.

Layer #	Material	Thickness (nm)
Substrate		
1	WO_3	59
2	LiF	125
3	WO_3	216
4	LiF	105
5	WO_3	73

A.3 Configuration of the multilayer structures.

6	LiF	95
7	WO_3	200
8	LiF	74
9	WO_3	232
10	LiF	90
11	WO_3	69
12	LiF	105
13	WO_3	53
14	LiF	126
15	WO_3	250
16	LiF	114
17	WO_3	66
18	LiF	113
19	WO_3	149
20	LiF	97
21	WO_3	73
22	LiF	88
23	WO_3	88
24	LiF	85
25	WO_3	137
26	LiF	87
27	WO_3	73
28	LiF	143
29	WO_3	250
Air		

Table A.3 Configuration of the fabricated polarising structure made of 15 alternating layers of TiO_2 and SiO_2.

Layer #	Material	Thickness (nm)
Substrate		
1	TiO_2	60
2	SiO_2	91
3	TiO_2	63
4	SiO_2	71
5	TiO_2	144
6	SiO_2	50
7	TiO_2	127
8	SiO_2	77
9	TiO_2	56
10	SiO_2	91
11	TiO_2	59
12	SiO_2	99
13	TiO_2	78
14	SiO_2	117
15	TiO_2*	56
Air		

*In order to compensate the optical effect caused by the deposition of many dielectric layers on top of each other, the refractive index used for this layer is the one corresponding to TiO_2 last layer as described in Figure A.11.

Appendix B Experimental procedures and characterization

B.1 $(FAI)_x(MABr)_{1-x}PbI_2$ perovskite solar cells

All commercially available chemicals were employed without any further purification. To get the SnO2 nanoparticle precursor, 134 µL of SnO2 nanoparticle suspension (Alfa Aesar (tin(IV) oxide, 15% in H_2O colloidal dispersion) were mixed with 866 µL of methanol (Scharlau, 99.5%). Perovskite precursors were prepared inside a N_2 glovebox by dissolving 1.2 M PbI_2 (Sigma Aldrich, 99%) solution in dimethylformamide (Sigma-Aldrich, 99.8%) and dimethylsulfoxide (VWR, 99.5%) with a 4:1 volume ratio and adding 2.5 wt% of $PbBr_2$ (Sigma Aldrich, 99.999%). The solution was kept at 80 ºC and under stirring overnight. The second precursor was prepared by mixing 60 mg of formamidinium iodide (Sigma Aldrich, 98%), 6 mg of methylammonium bromide (Sigma Aldrich, 98%) and 6 mg of methylammonium chlorine (Sigma Aldrich) in 1 ml of 2-propanol (Scharlau, 99.5%). A 72.3 mg/ml 2,2',7,7'-Tetrakis[N,N-di(4-methoxyphenyl)amino]-9,9'-spirobifluorene (Spiro-OMeTAD, Merck) solution was prepared in chlorobenzene (Sigma-Aldrich, 99.8%). For the doping of the hole transporting material, 17 µL of a 520 mg/mL bis(trifluoromethylsulfonyl)amine lithium salt (Li-TFSI, Sigma-Aldrich, 99.95%) solution in acetonitrile (Sigma-Aldrich, 99.8%) and 29 µL of 4-tert-butylpyridine (TBP, Sigma-Aldrich 96%) were added to the solution. The polydimethylsiloxane (PDMS, Sylgrad 184, Dow Corning) was prepared in an 8:1 weight ratio of base and curing agents.

For the deposition of the different layers, full-covered ITO substrates (100 nm, 15 Ωsq^{-1}, Stuttgart) were employed as substrate for the perovskite solar cell, previously cleaned in 10 minutes cycles of soap solution, water, acetone, water and ethanol. After an ultraviolet-ozone (UVO) treatment of 15 minutes, the SnO_2 nanoparticle solution was spin-coated onto the cleaned ITO substrates at 3500 rpm, followed by a thermal annealing at 150 ºC during 30 minutes in air. The samples were then transferred into a glovebox for next fabrication steps. The lead solution was spin-coated at 60 ºC on top of the electron transporting layer at 2000 rpm. Then, the organic solution was deposited at 2000 rpm for 30 seconds. After some minutes of drying inside the glovebox, the samples were transferred to a fumehood to perform an annealing at 150 ºC during 20 minutes in ambient air. After that, the Spiro-OMeTAD solution was deposited at 2000 rpm on top of the perovskite layer. The following day, a 60 nm thick gold top contact layer was evaporated in a high vacuum chamber (Lesker). The deposition rate was adjusted to 0.55 Å/s and a metal mask was place to define an active area of 0.096 cm^2.

B.2 High Voc perovskite solar cells

The planar perovskite solar cells used as light recycling elements were fabricated with the following architecture: glass/ITO/(2-(9H-carbazol-9-yl)ethyl)phosphonic acid (2PACz) /$Cs_{0.18}FA_{0.82}PbI_3$ /C_{60} /bathocuproine (BCP) /Ag. For the preparation of the HTL precursor, 2PACz was dissolved in anhydrous ethanol obtaining a solution of 1 mmol/l. The double cation perovskite precursor solution was prepared by mixing PbI_2 (507 mg: 10% excess of PbI_2), CsCl (30 mg) and FAI (172 mg) in 1 mL solvent mixture of DMF:DMSO 4:1 volume ratio. To prepare the passivating solution, phenyl ethylammonium chloride (PEACl) dissolved in IPA with a concentration of 1.5 mg/ml.

ITO substrates (sheet resistance 15 Ω/sq, Luminescence Technology) were cut in 0.30 cm × 0.30 cm and cleaned with acetone and isopropanol in ultrasonic bath for 10 minutes each. Then, the substrates were further treated with oxygen plasma for 3 min before the deposition of the 2PACz. After putting the 2PACz solution 15 min in an ultrasonic bath for 15 mins, a thin layer of this material was deposited on the ITO substrate by spin-coating at 3000 rpm for 30 s and subsequently annealed at 100 °C for 10 min. The perovskite film was deposited on the substrate at 1000 rpm for 10 s and 5000 rpm for 30 s. 20 s after the start of the second step spin-coating, 150 µL chlorobenzene was quickly dropped on the spinning substrate. The samples were then annealed at 150 °C for 30 min in an inert atmosphere. The perovskite layer was passivated by dynamically spin coating the PEACl solution on top of the reference perovskite film at 5000 rpm for 30 s, followed by annealing at 100 °C for 5 min. The C60/BCP respective layers were thermally evaporated and, finally, an Ag layer was deposited by thermal evaporation, being the masked area of 0.145 mm^2.

B.3 $MAPbI_3$ perovskite solar cells

To get the TiO_2 nanoparticle precursor, 75 µL of TiO_2 nanoparticle suspension (Plasmachem, 20 wt% suspension in water, 4-8 nm) were mixed with 905 µL of methanol (Scharlau, 99.5%) and 20 µL of titanium diisopropoxidebis(acetylacetonate) ($Ti(acac)_2OiPr_2$, Sigma-Aldrich, 75 wt%). Based on previous reports,[159,195] the $Ti(acac)_2OiPr_2$ acts as a bridge between the surrounding nanoparticles, which thanks to a possible chelation of the acetylacetonate to the TiO_2 creates a coordinate ligand between them. A similar procedure was followed to obtain the SnO_2 nanoparticle precursor but, this time, 486.6 µL of SnO_2 nanoparticle suspension (Avantama AG, 2.5 wt% suspension in ethanol, 10 nm) were mixed with 500 µL of ethanol (Scharlau, 99.5%) and

13.4 µL of the organic titanate solution. Both suspensions were kept under stirring overnight before being used. Perovskite precursors were prepared inside a N_2 glovebox by dissolving methylammonium iodide (CH_3NH_3I, 1-Material, 99.5%) and lead (II) chloride ($PbCl_2$, Sigma-Aldrich, 98%) with a 3:1 molar ratio in dimethylformamide (Sigma-Aldrich, 99.8%) and using different weight concentrations depending on the desired film thickness (Supplementary Information, Figure S1). A 15 mg/ml poly[bis(4-phenyl)(2,4,6-trimethylphenyl)amine] (PTAA, Ossila) solution was prepared in toluene (Sigma-Aldrich, 99.8%) by keeping the mixture under stirring overnight at 60 °C. For the doping of the hole transporting material, 10 µL of a 170 mg/mL bis(trifluoromethylsulfonyl)amine lithium salt (Li-TFSI, Sigma-Aldrich, 99.95%) solution in acetonitrile (Sigma-Aldrich, 99.8%) and 5 µL of 4-tert-butylpyridine (TBP, Sigma-Aldrich, 96%) were added to the solution.

For the deposition of the solar cell precursors, two different types of ITO coated glass substrates were used depending on the final device configuration. For semi-transparent solar cells, two-stripe patterned ITO substrates (140 nm, 15 Ωsq^{-1}, Lumtec) were used, whereas for opaque ones full-covered ITO substrates (100 nm, 15 Ωsq^{-1}, Stuttgart) were employed. The electron transporting material, either as a single or as a double layer, was obtained by subsequently spin-coating the corresponding nanoparticle suspensions onto the cleaned ITO substrates at 6000 rpm, followed by a thermal annealing at 150 ºC during 30 minutes in air. The samples were then transferred into a glovebox for next fabrication steps. The perovskite solution was spin-coated on top of the electron transporting layer at 2500 rpm and the resulting films were annealed for 2 hours at 90 °C plus 20 minutes at 125 °C. After that, the PTAA solution was deposited at 2500 rpm on top of the perovskite layer. An 80 nm thick gold top contact layer was then evaporated in a high vacuum chamber (Lesker) for opaque cells. The deposition

rate was adjusted to 0.6 Å/s and a metal mask was place to define an active area of 0.096 cm^2. For the semi-transparent devices, 12 nm of gold were deposited at a rate of 0.75 Å/s, followed by 40 nm of MoO_3 using an evaporation rate of 0.6 Å/s. This time a metal mask that conferred an active area of 0.06 cm^2 was used.

B.4 Characterization of materials and devices

The surface morphology of the h-CPP and perovskite films, as well as the cross section of the devices, were evaluated by field emission scanning electron microscopy (FEG-SEM, FEI Inspect F-EBL). The X-ray diffraction (XRD) patterns were recorded with a Bruker D8 Advance diffractometer (Bruker, Cu-Kα source). Film thicknesses of the different layers included on PV devices values were determined employing a surface profilometer (Alpha-Step IQ Surface Profiler, KLA-Tencor) and contrasted by the image obtained of the complete cell cross section with the FEG-SEM. The wavelength-dependent refractive index n and extinction coefficient k of the materials were determined by spectroscopic ellipsometry. For the perovskite, ellipsometric measurements were done with a UV-Vis-NIR Woollam VASE ellipsometer, where n and k were modelled as a sum of Kramers-Kronig consistent oscillators. For the other materials, ellipsometric measurements were done with a UV-Vis-NIR SOPRA GESP5 ellipsometer at angles of incidence between 50º and 70º, and n and k were modelled using a Cauchy law plus Kramers-Kronig consistent oscillators when needed. The optical transmission of the different samples was measured over the wavelength range of interest using a UV-vis-NIR spectrometer (Lambda 950, PerkinElmer).

The PV performance of the fabricated solar cells under sunlight was determined using an AM 1.5G solar simulator (Sun 3000, Abet Technologies).

B.4 Characterization of materials and devices

The illumination intensity corresponding to 100 $mWcm^{-2}$ was adjusted with a monocrystalline silicon reference cell (Hamamatsu) calibrated at the Fraunhofer Institute for Solar Energy Systems. For RGB chromatic illumination, low intensity light sources from Thorlabs (CPS635R, CPS532 and CPS450) were employed using an optical lens to focus the beam when necessary. The high intensity illumination was performed by a continuous wave Nd:YAG Coherent Compass power tuneable laser (wavelength: 532 nm). In this case, a quarter wave and a polariser were used to analyse the effect of each type of light polarisation on the electrical current generation by the solar cell. When polarised light was introduced in the ensemble, the same light intensity was used for both characterisations in order to compare the effect. The current voltage (J-V) curves were then recorded by scanning from positive to negative voltages (1.2 V to -0.2 V) using a Keithley 2400 SourceMeter and a scan speed of 350 mV/s. External quantum efficiency (EQE) analysis was performed using a quantum efficiency measurement system (QEX10, PV Measurements). In this case, the devices were illuminated using a monochromatic light coming from a xenon lamp. The spectral response of the calibrated silicon cell was used as a reference. All set of devices were tested under ambient conditions.

Bibliography

1 V. Smil, *Energy transitions: global and national perspectives*, ABC-CLIO, 2016.

2 BP, *Statistical Review of World Energy*, 2020.

3 C. for G. Development, Electricity Consumption and Development Indicators, https://www.cgdev.org/media/electricity-consumption-and-development-indicators, (accessed 23 March 2021).

4 J. Chontanawat, L. C. Hunt and R. Pierse, *J. Policy Model.*, 2008, **30**, 209–220.

5 K. H. Ghali and M. I. T. El-Sakka, *Energy Econ.*, 2004, **26**, 225–238.

6 M. A. Toman and B. Jemelkova, *Energy J.*, 2003, **24**, 93–112.

7 A. Caillé, M. Al-Moneef, F. Bernés de Castro, A. Bundgaard-Jensen, A. Fall, N. Franco de Medeiros, C. P. Jain, Y. D. Kim, M.-J. Nadeau, C. Test, J. Teyssen, E. Velasco García, R. Wood, Z. Guobao and G. Doucet, *Energy Efficiency Policies around the World: Review and Evaluation*, 2008.

8 N. A. Madlool, R. Saidur, M. S. Hossain and N. A. Rahim, *Renew. Sustain. Energy Rev.*, 2011, **15**, 2042–2060.

9 K. Kermeli, E. Worrell and E. Masanet, *Energy Efficiency Improvement and Cost Saving Opportunities for the Concrete Industry*, 2011.

10 A. Carroll and G. Heiser, in *USENIX annual technical conference*, 2010, p. 21.

11 H. Kawamoto, *Proc. IEEE*, 2002, **90**, 460–500.

12 J. Kimmel, *J. Soc. Inf. Disp.*, 2012, **20**, 245.

13 H. W. Chen, J. H. Lee, B. Y. Lin, S. Chen and S. T. Wu, *Light Sci. Appl.*, 2018, **7**, 17168.

14 A. K. Bhowmik, Z. Li and P. J. Bos, *Mobile Displays*, 2008.

15 C. Gu, P. Yeh, X. Yang and G. Jin, in *Mobile displays technology and applications*, 2008, pp. 133–210.

16 M. F. Weber, C. A. Stover, L. R. Gilbert, T. J. Nevitt and A. J. Ouderkirk, *Science*, 2000, **287**, 2451–2456.

17 M. Suzuki, *J. Soc. Inf. Disp.*, 1999, **7**, 157–161.

18 Y. Li, S. T. Wu and T. X. Wu, *IEEE/OSA J. Disp. Technol.*, 2009, **5**, 335–340.

19 K. W. Chien and H. P. D. Shieh, *Appl. Opt.*, 2004, **43**, 1830–1834.

20 X. Yang, Y. Yan and G. Jin, *Opt. Express*, 2005, **13**, 8349.

21 *Key World Energy Statistics*, 2017.

22 Brilliant, https://brilliant.org/practice/essential-energy-sunlight/, (accessed 12 March 2021).

23 A. Kojima, K. Teshima, Y. Shirai and T. Miyasaka, *J. Am. Chem. Soc.*, 2009, **131**, 6050–6051.

24 H. S. Kim, C. R. Lee, J. H. Im, K. B. Lee, T. Moehl, A. Marchioro, S. J. Moon, R. Humphry-Baker, J. H. Yum, J. E. Moser, M. Grätzel and N. G. Park, *Sci. Rep.*, 2012, **2**, 1–7.

25 M. M. Lee, J. Teuscher, M. Tsutomu, T. N. Murakami and H. J. Snaith, *Science*, 2012, **338**, 643–647.

26 J. H. Heo, S. H. Im, J. H. Noh, T. N. Mandal, C. S. Lim, J. A. Chang, Y. H. Lee, H. J. Kim, A. Sarkar, M. K. Nazeeruddin, M. Grätzel and S. Il Seok, *Nat. Photonics*, 2013, **7**, 486–491.

27 M. Liu, M. B. Johnston and H. J. Snaith, *Nature*, 2013, **501**, 395–398.

28 S. D. Stranks, G. E. Eperon, G. Grancini, C. Menelaou, M. J. P. Alcocer, T. Leijtens, L. M. Herz, A. Petrozza and H. J. Snaith, *Science*, 2013, **342**, 341–344.

29 J. Burschka, N. Pellet, S. J. Moon, R. Humphry-Baker, P. Gao, M. K. Nazeeruddin and M. Grätzel, *Nature*, 2013, **499**, 316–319.

30 J. H. Noh, S. H. Im, J. H. Heo, T. N. Mandal and S. Il Seok, *Nano Lett.*, 2013, **13**, 1764–1769.

31 H. Chen, Q. Wei, M. I. Saidaminov, F. Wang, A. Johnston, Y. Hou, Z. Peng, K. Xu, W. Zhou, Z. Liu, L. Qiao, X. Wang, S. Xu, J. Li, R. Long, Y. Ke, E. H. Sargent and Z. Ning, *Adv. Mater.*, 2019, **31**, 1903559.

32 X. Zheng, Y. Hou, C. Bao, J. Yin, F. Yuan, Z. Huang, K. Song, J. Liu, J. Troughton, N. Gasparini, C. Zhou, Y. Lin, D. J. Xue, B. Chen, A. K. Johnston, N. Wei, M. N. Hedhili, M. Wei, A. Y. Alsalloum, P. Maity, B. Turedi, C. Yang, D. Baran, T. D. Anthopoulos, Y. Han, Z. H. Lu, O. F. Mohammed, F. Gao, E. H. Sargent and O. M. Bakr, *Nat. Energy*, 2020, **5**, 131–140.

33 L. Xie, K. Lin, J. Lu, W. Feng, P. Song, C. Yan, K. Liu, L. Shen, C. Tian and Z. Wei, *J. Am. Chem. Soc.*, 2019, **141**, 20537–20546.

34 H. Min, M. Kim, S. U. Lee, H. Kim, G. Kim, K. Choi, J. H. Lee and S. Il Seok, *Science*, 2019, **366**, 749–753.

35 M. Jeong, I. W. Choi, E. M. Go, Y. Cho, M. Kim, B. Lee, S. Jeong, Y. Jo, H. W. Choi, J. Lee, J. H. Bae, S. K. Kwak, D. S. Kim and C. Yang, *Science*, 2020, **369**, 1615–1620.

36 W. S. Yang, B.-W. Park, E. H. Jung, N. J. Jeon, Y. C. Kim, D. U. Lee, S. S. Shin, J. Seo, E. K. Kim, J. H. Noh and S. Il Seok, *Science*, 2017, **356**, 1376–1379.

37 Y. Li, J. Shi, J. Zheng, J. Bing, J. Yuan, Y. Cho, S. Tang, M. Zhang, Y. Yao, C. F. J. Lau, D. S. Lee, C. Liao, M. A. Green, S. Huang, W. Ma and A. W. Y. Ho-Baillie, *Adv. Sci.*, 2020, **7**, 1903368.

38 Y. Zhao, P. Zhu, M. Wang, S. Huang, Z. Zhao, S. Tan, T. H. Han, J. W. Lee, T. Huang, R. Wang, J. Xue, D. Meng, Y. Huang, J. Marian, J. Zhu and Y. Yang, *Adv. Mater.*, 2020, **32**, 1907769.

39 Q. Jiang, Y. Zhao, X. Zhang, X. Yang, Y. Chen, Z. Chu, Q. Ye, X. Li, Z. Yin and J. You, *Nat. Photonics*, 2019, **13**, 460–466.

40 M. A. Mahmud, T. Duong, Y. Yin, H. T. Pham, D. Walter, J. Peng, Y. Wu, L. Li, H. Shen, N. Wu, N. Mozaffari, G. Andersson, K. R. Catchpole, K. J. Weber and T. P. White, *Adv. Funct. Mater.*, 2020, **30**, 1907962.

41 S. Gharibzadeh, I. M. Hossain, P. Fassl, B. A. Nejand, T. Abzieher, M. Schultes, E. Ahlswede, P. Jackson, M. Powalla, S. Schäfer, M. Rienäcker, T. Wietler, R. Peibst, U. Lemmer, B. S. Richards and U. W. Paetzold, *Adv. Funct. Mater.*, 2020, **30**, 1909919.

42 J. Cao, B. Wu, R. Chen, Y. Wu, Y. Hui, B. W. Mao and N. Zheng, *Adv. Mater.*, 2018, **30**, 1705596.

43 T. Wang, D. Ding, H. Zheng, X. Wang, J. Wang, H. Liu and W. Shen, *Sol. RRL*, 2019, **3**, 1900045.

44 W. Hui, Y. Yang, Q. Xu, H. Gu, S. Feng, Z. Su, M. Zhang, J. Wang, X. Li, J. Fang, F. Xia, Y. Xia, Y. Chen, X. Gao and W. Huang, *Adv. Mater.*, 2020, **32**, 1906374.

45 P. Wang, R. Li, B. Chen, F. Hou, J. Zhang, Y. Zhao and X. Zhang, *Adv. Mater.*, 2020, **32**, 1905766.

46 Y. Kim, E. H. Jung, G. Kim, D. Kim, B. J. Kim and J. Seo, *Adv. Energy Mater.*, 2018, **8**, 1801668.

47 S. Akin, *ACS Appl. Mater. Interfaces*, 2019, **11**, 39998–40005.

48 L. Wang, H. Zhou, N. Li, Y. Zhang, L. Chen, X. Ke, Z. Chen, Z. Wang, M. Sui, Y. Chen, Y. Huang, L. Li, Z. Xu, Q. Chen, L. D. Sun and C. H. Yan, *J. Mater. Chem. A*, 2020, **8**, 14106–14113.

49 X. J. Ma, X. D. Zhu, K. L. Wang, F. Igbari, Y. Yuan, Y. Zhang, C. H. Gao, Z. Q. Jiang, Z. K. Wang and L. S. Liao, *Nano Energy*, 2019, **63**, 103865.

50 B. Ding, S. Y. Huang, Q. Q. Chu, Y. Li, C. X. Li, C. J. Li and G. J. Yang, *J. Mater. Chem. A*, 2018, **6**, 10233–10242.

51 NREL, https://www.nrel.gov/pv/cell-efficiency.html.

52 N. Li, X. Niu and H. Zhou, *Chem. Soc. Rev.*, 2020, **49**, 8235–8286.

53 Q. Wali, F. Jan, M. Ejaz, A. Ullah, Y. Iqbal and R. Jose, *Org. Electron.*, 2020, **78**, 105590.

54 M. Kim, J. M. Figueroa-Tapia, M. Prato and A. Petrozza, *Adv. Energy Mater.*, 2020, **10**, 1903221.

55 H.-H. Huang, Y.-C. Shih, L. Wang and K. Lin, *Energy Environ. Sci.*, 2019, **12**, 1265.

56 F. Bella, G. Griffini, G. Saracco, M. Grätzel, A. Hagfeldt, S. Turri and C. Gerbaldi, *Science*, 2016, **354**, 203–206.

57 W. Tress, K. Domanski, B. Carlsen, A. Agarwalla, E. A. Alharbi, M. Graetzel and A. Hagfeldt, *Nat. Energy*, 2019, **5**, 568–574.

58 Z. Li, T. R. Klein, D. H. Kim, M. Yang, J. J. Berry and K. Zhu, *Nat. Rev. Mater.*, 2018, **3**, 1–20.

59 J. H. Heo, M. H. Lee, M. H. Jang and S. H. Im, *J. Mater. Chem. A*, 2016, **4**, 17636–17642.

60 E. Bi, W. Tang, X. Yang, E. Bi, W. Tang, H. Chen, Y. Wang, J. Barbaud, T. Wu, W. Kong, P. Tu, H. Zhu, X. Zeng, J. He, S. Kan, X. Yang, M. Grätzel and L. Han, *Joule*, 2019, **3**, 2748–2760.

61 P. Li, C. Liang, B. Bao, Y. Li, X. Hu, Y. Wang, Y. Zhang, F. Li, G. Shao and Y. Son, *Nano Energy*, 2018, **46**, 203–211.

62 Z. Xu, R. Chen, Y. Wu, R. He, J. Yin, W. Lin, B. Wu, J. Li and N. Zheng, *J. Mater. Chem. A*, 2019, **7**, 26849–26857.

63 C. Li, J. Yin, R. Chen, X. Lv, X. Feng, Y. Wu and J. Cao, *J. Am. Chem. Soc.*, 2019, **141**, 6351.

64 W. Wu, Z. Yang, P. N. Rudd, Y. Shao, X. Dai, H. Wei, J. Zhao, Y. Fang, Q. Wang, Y. Liu, Y. Deng, X. Xiao, Y. Feng and J. Huang, *Sci. Adv.*, 2019, **5**, 1–9.

65 C. Roldán-Carmona, O. Malinkiewicz, R. Betancur, G. Longo, C. Momblona, F. Jaramillo, L. Camacho and H. J. Bolink, *Energy Environ. Sci.*, 2014, **7**, 2968–2973.

66 A. Babayigit, A. Ethirajan, M. Muller and B. Conings, *Nat. Mater.*, 2016, **15**, 247–251.

67 Q. Zhang, F. Hao, J. Li, Y. Zhou, Y. Wei and H. Lin, *Sci. Technol. Adv. Mater.*, 2018, **19**, 452–442.

68 M. Wang, W. Wang, B. Ma, W. Shen, L. Liu, K. Cao, S. Chen and W. Huang, *Nano-Micro Lett.*, 2021, **13**, 1–36.

69 A. Abate, *Joule*, 2017, **1**, 659–664.

70 E. Yablonovitch, *J. Opt. Soc. Am.*, 1982, **72**, 899–907.

71 Z. Yu, A. Raman and S. Fan, *Opt. Express*, 2010, **18**, A366.

72 E. A. Schiff, *J. Appl. Phys.*, 2011, **110**, 104501.

73 H. R. Stuart and D. G. Hall, *Opt. Soc. Am. A*, 1997, **14**, 3001–3008.

74 Z. Yu, A. Raman and S. Fan, *Proc. Natl. Acad. Sci. U. S. A.*, 2010, **107**, 17491–17496.

75 D. M. Callahan, J. N. Munday and H. A. Atwater, *Nano Lett.*, 2012, **12**, 214–218.

76 M. A. Green, *Prog. Photovoltaics Res. Appl.*, 2002, **10**, 235–241.

77 S. Fahr, C. Rockstuhl and F. Lederer, *Appl. Phys. Lett.*, 2008, **92**, 171114.

78 F. Arabpour Roghabadi, N. Ahmadi, V. Ahmadi, A. Di Carlo, K. Oniy Aghmiuni, A. Shokrolahzadeh Tehrani, F. S. Ghoreishi, M. Payandeh and N. Mansour Rezaei Fumani, *Sol. Energy*, 2018, **173**, 407–424.

79 T. D. Lee and A. U. Ebong, *Renew. Sustain. Energy Rev.*, 2017, **70**, 1286–1297.

80 P. A. Troshin, H. Hoppe, A. S. Peregudov, M. Egginger, S. Shokhovets, G. Gobsch, N. S. Sariciftci and V. F. Razumov, *ChemSusChem*, 2011, **4**, 119–124.

81 C. Wang, W. Zhang, X. Meng, J. Bergqvist, X. Liu, Z. Genene, X. Xu, A. Yartsev, O. Inganäs, W. Ma, E. Wang and M. Fahlman, *Adv. Energy Mater.*, 2017, **7**, 1700390.

82 H. Fujiwara, M. Kato, M. Tamakoshi, T. Miyadera and M. Chikamatsu, *Phys. Status Solidi Appl. Mater. Sci.*, 2018, **215**, 1700730.

83 Q. Liu, J. Toudert, T. Li, M. Kramarenko, G. Martínez-Denegri, L. Ciammaruchi, X. Zhan and J. Martorell, *Adv. Energy Mater.*, 2019, **9**, 1900463.

84 M. A. Green, *Prog. Photovoltaics Res. Appl.*, 2011, **19**, 473–477.

85 J. Müller, B. Rech, J. Springer and M. Vanecek, *Sol. Energy*, 2004, **77**, 917–930.

86 L. Zhu, Y. Hazama, A. Reddy, K. Watanabe, Y. Nakano, M. Sugiyama and H. Akiyama, *Prog. Photovoltaics Res. Appl.*, 2020, **28**, 251–265.

87 C. Heine and R. H. Morf, *Appl. Opt.*, 1995, **34**, 2476.

88 S. Esiner, T. Bus, M. M. Wienk, K. Hermans and R. A. J. Janssen, *Adv. Energy Mater.*, 2013, **3**, 1013–1017.

89 K. Tvingstedt, Z. Tang and O. Inganäs, *Appl. Phys. Lett.*, 2012, **101**, 163902.

90 H. Sai, Y. Kanamori, K. Arafune, Y. Ohshita and M. Yamaguchi, *Prog. Photovoltaics Res. Appl.*, 2007, **15**, 415–423.

91 F. Hou, C. Han, O. Isabella, L. Yan, B. Shi, J. Chen, S. An, Z. Zhou, W. Huang, H. Ren, Q. Huang, G. Hou, X. Chen, Y. Li, Y. Ding, G. Wang, C. Wei, D. Zhang, M. Zeman, Y. Zhao and X. Zhang, *Nano Energy*, 2019, **56**, 234–240.

92 S. Manzoor, Z. J. Yu, A. Ali, W. Ali, K. A. Bush, A. F. Palmstrom, S. F. Bent, M. D. McGehee and Z. C. Holman, *Sol. Energy Mater. Sol. Cells*, 2017, **173**, 59–65.

93 R. T. Ginting, E. B. Jeon, J. M. Kim, W. Y. Jin and J. W. Kang, *ACS Appl. Mater. Interfaces*, 2018, **10**, 31291–31299.

94 H. Zhang, M. Kramarenko, J. Osmond, J. Toudert and J. Martorell, *ACS Photonics*, 2018, **5**, 2243–2250.

95 B. Shi, B. Liu, J. Luo, Y. Li, C. Zheng, X. Yao, L. Fan, J. Liang, Y. Ding, C. Wei, D. Zhang, Y. Zhao and X. Zhang, *Sol. Energy Mater. Sol. Cells*, 2017, **168**, 214–220.

96 Y. Wang, P. Wang, X. Zhou, C. Li, H. Li, X. Hu, F. Li, X. Liu, M. Li and Y. Song, *Adv. Energy Mater.*, 2018, **8**, 1702960.

97 D. L. Wang, H. J. Cui, G. J. Hou, Z. G. Zhu, Q. B. Yan and G. Su, *Sci. Rep.*, 2016, **6**, 1–10.

98 U. W. Paetzold, W. Qiu, F. Finger, J. Poortmans and D. Cheyns, *Appl. Phys. Lett.*, 2015, **106**, 173101.

99 W. Qarony, M. I. Hossain, A. Salleo, D. Knipp and Y. H. Tsang, *Mater. Today Energy*, 2019, **11**, 106–113.

100 M. Jošt, S. Albrecht, L. Kegelmann, C. M. Wolff, F. Lang, B. Lipovšek, J. Krč, L. Korte, D. Neher, B. Rech and M. Topič, *ACS Photonics*, 2017, **4**, 1232–1239.

101 M. H. Ann, J. Kim, M. Kim, G. Alosaimi, D. Kim, N. Y. Ha, J. Seidel, N. Park, J. S. Yun and J. H. Kim, *Nano Energy*, 2020, **68**, 104321.

102 C. Y. Chen, J. H. Chang, K. M. Chiang, H. L. Lin, S. Y. Hsiao and H. W. Lin, *Adv. Funct. Mater.*, 2015, **25**, 7064–7070.

103 J. Dagar, S. Castro-Hermosa, G. Lucarelli, F. Cacialli and T. M. Brown, *Nano Energy*, 2018, **49**, 290–299.

104 H. Sun, K. Deng, Y. Jiang, J. Ni, J. Xiong and L. Li, *Small*, 2020, **16**, 1906681.

105 R. Zhu, A. Kumar and Y. Yang, *Adv. Mater.*, 2011, **23**, 4193–4198.

106 B. Park, Y. H. Huh and J. C. Shin, *Sol. Energy Mater. Sol. Cells*, 2011, **95**, 3543–3549.

107 A. Menéndez-Velázquez, C. L. Mulder, N. J. Thompson, T. L. Andrew, P. D. Reusswig, C. Rotschild and M. A. Baldo, *Energy Environ. Sci.*, 2013, **6**, 72–75.

108 M. Saliba, T. Matsui, K. Domanski, J.-Y. Seo, A. Ummadisingu, S. M. Zakeeruddin, J.-P. Correa-Baena, W. R. Tress, A. Abate, A. Hagfeldt and M. Gratzel, *Science*, 2016, **354**, 206–209.

109 D. Bi, C. Yi, J. Luo, J.-D. Décoppet, F. Zhang, S. M. Zakeeruddin, X. Li, A. Hagfeldt and M. Grätzel, *Nat. Energy*, 2016, **1**, 16142.

110 W. S. Yang, J. H. Noh, N. J. Jeon, Y. C. Kim, S. Ryu, J. Seo and S. Il Seok, *Science.*, 2015, **348**, 1234–1237.

111 E. H. Jung, N. J. Jeon, E. Y. Park, C. S. Moon, T. J. Shin, T. Y. Yang, J. H. Noh and J. Seo, *Nature*, 2019, **567**, 511–515.

112 H. Tan, A. Jain, O. Voznyy, X. Lan, F. P. G. De Arquer, J. Z. Fan, R. Quintero-Bermudez, M. Yuan, B. Zhang, Y. Zhao, F. Fan, P. Li, L. N. Quan, Y. Zhao, Z. H. Lu, Z. Yang, S. Hoogland and E. H. Sargent, *Science*, 2017, **355**, 722–726.

113 P. Qin, M. Paulose, M. I. Dar, T. Moehl, N. Arora, P. Gao, O. K. Varghese, M. Grätzel and M. K. Nazeeruddin, *Small*, 2015, **11**, 5533–5539.

114 W. Q. Wu, J. F. Liao, Y. Jiang, L. Wang and D. Bin Kuang, *Small*, 2019, **15**, 1900606.

115 A. Alberti, E. Smecca, S. Sanzaro, C. Bongiorno, F. Giannazzo, G. Mannino, A. La Magna, M. Liu, P. Vivo, A. Listorti, E. Calabrò, F. Matteocci and A. Di Carlo, *ACS Appl. Energy Mater.*, 2019, **2**, 6218–6229.

116 C. Chen, D. Liu, Y. Wu, W. Bi, X. Sun, X. Chen, W. Liu, L. Xu, H. Song and Q. Dai, *Nano Energy*, 2018, **53**, 849–862.

117 V. Zardetto, F. di Giacomo, H. Lifka, M. A. Verheijen, C. H. L. Weijtens, L. E. Black, S. Veenstra, W. M. M. Kessels, R. Andriessen and M. Creatore, *Adv. Mater. Interfaces*, 2018, **5**, 2–7.

118 S. Yuan, Y. Cai, S. Yang, H. Zhao, F. Qian, Y. Han, J. Sun, Z. Liu and S. Liu, *Sol. RRL*, 2019, **3**, 1900220.

119 N. Ahn, K. Kwak, M. S. Jang, H. Yoon, B. Y. Lee, J.-K. Lee, P. V. Pikhitsa, J. Byun and M. Choi, *Nat. Commun.*, 2016, **7**, 13422.

120 S. H. Turren-Cruz, M. Saliba, M. T. Mayer, H. Juárez-Santiesteban, X. Mathew, L. Nienhaus, W. Tress, M. P. Erodici, M. J. Sher, M. G. Bawendi, M. Grätzel, A. Abate, A. Hagfeldt and J. P. Correa-Baena, *Energy Environ. Sci.*, 2018, **11**, 78–86.

121 H. R. Liu, S. H. Li, L. L. Deng, Z. Y. Wang, Z. Xing, X. Rong, H. R. Tian, X. Li, S. Y. Xie, R. Bin Huang and L. S. Zheng, *ACS Appl. Mater. Interfaces*, 2019, **11**, 23982–23989.

122 J. Zou, W. Liu, W. Deng, G. Lei, S. Zeng, J. Xiong, H. Gu, Z. Hu, X. Wang and J. Li, *Electrochim. Acta*, 2018, **291**, 297–303.

123 Y. Sanehira, N. Shibayama, Y. Numata, M. Ikegami and T. Miyasaka, *ACS Appl. Mater. Interfaces*, 2020, **12**, 15175–15182.

124 M. He, B. Li, X. Cui, B. Jiang, Y. He, Y. Chen, D. O'Neil, P. Szymanski, M. A. Ei-Sayed, J. Huang and Z. Lin, *Nat. Commun.*, 2017, **8**, 1–10.

125 R. Singh, I. Ryu, H. Yadav, J. Park, J. W. Jo, S. Yim and J. J. Lee, *Sol. Energy*, 2019, **185**, 307–314.

126 J. Song, L. Liu, X. F. Wang, G. Chen, W. Tian and T. Miyasaka, *J. Mater. Chem. A*, 2017, **5**, 13439–13447.

127 A. Gheno, T. T. Thu Pham, C. Di Bin, J. Bouclé, B. Ratier and S. Vedraine, *Sol. Energy Mater. Sol. Cells*, 2017, **161**, 347–354.

128 Q. Dong, C. H. Y. Ho, H. Yu, A. Salehi and F. So, *Chem. Mater.*, 2019, **31**, 6833–6840.

129 Q. Jiang, L. Zhang, H. Wang, X. Yang, J. Meng, H. Liu, Z. Yin, J. Wu, X. Zhang and J. You, *Nat. Energy*, 2016, **2**, 16177.

130 R. Wang, J. Xue, K. L. Wang, Z. K. Wang, Y. Luo, D. Fenning, G. Xu, S. Nuryyeva, T. Huang, Y. Zhao, J. L. Yang, J. Zhu, M. Wang, S. Tan, I. Yavuz, K. N. Houk and Y. Yang, *Science*, 2019, **366**, 1509–1513.

131 H. Zhang, M. Kramarenko, J. Osmond, J. Toudert and J. Martorell, *ACS Photonics*, 2018, **5**, 2243–2250.

132 L. Zheng, Y. Ma, S. Chu, S. Wang, B. Qu, L. Xiao, Z. Chen, Q. Gong, Z. Wu and X. Hou, *Nanoscale*, 2014, **6**, 8171–8176.

133 D. Liu and T. L. Kelly, *Nat. Photonics*, 2014, **8**, 133–138.

134 M. Mariano, G. Kozyreff, L. G. Gerling, P. Romero-Gomez, J. Puigdollers, J. Bravo-Abad and J. Martorell, *Light Sci. Appl.*, 2016, **5**, 1–7.

135 D.-L. Wang, H.-J. Cui, G.-J. Hou, Z.-G. Zhu, Q.-B. Yan and G. Su, *Sci. Rep.*, 2016, **6**, 18922.

136 R. T. Ginting, E. B. Jeon, J. M. Kim, W. Y. Jin and J. W. Kang, *ACS Appl. Mater. Interfaces*, 2018, **10**, 31291–31299.

137 M. M. Tavakoli, K.-H. Tsui, Q. Zhang, J. He, Y. Yao, D. Li and Z. Fan, *ACS Nano*, 2015, **9**, 10287–10295.

138 N. J. Jeon, J. H. Noh, W. S. Yang, Y. C. Kim, S. Ryu, J. Seo and S. Il Seok, *Nature*, 2015, **517**, 476–480.

139 N. Pellet, P. Gao, G. Gregori, T. Y. Yang, M. K. Nazeeruddin, J. Maier and M. Gr??tzel, *Angew. Chemie - Int. Ed.*, 2014, **53**, 3151–3157.

140 M. A. Kats, R. Blanchard, P. Genevet and F. Capasso, *Nat. Mater.*, 2013, **12**, 20–24.

141 M. A. Kats, R. Blanchard, S. Ramanathan and F. Capasoo, *Opt. Photonics News*, 2014, **25**, 40–47.

142 S. Russell, *The architecture of light: architectural lighting design concepts and techniques: a textbook of procedures and practices for the architect, interior designer and lighting designer*, Conceptnine, 2012.

143 S. Kobayashi, S. Mikoshiba and S. Lim, *LCD Backligths*, John Wiley & Sons, 2009.

144 T. Q. Khan, P. Bodrogi, Q. T. Vinh and H. Winkler, *LED lighting: Technology and perception*, John Wiley & Sons, 2015.

145 D. L. Perry, *Appl. Opt.*, 1965, **4**, 987.

146 J. Lekner, *J. Opt. A Pure Appl. Opt.*, 2000, **2**, 349–352.

147 G. Kedawat, S. Srivastava, V. K. Jain, P. Kumar, V. Kataria, Y. Agrawal, B. K. Gupta and Y. K. Vijay, *ACS Appl. Mater. Interfaces*, 2013, **5**, 4872–4877.

148 M. K. Tilsch, R. B. Sargent and C. A. Hulse, in *Wavelength Filters in Fibre Optics*, 2006, vol. 123, pp. 289–340.

149 H. F. Mahlein, *Opt. Commun.*, 1976, **16**, 420–424.

150 A. Ranjbar and A. Grbic, *Phys. Rev. Appl.*, 2019, **11**, 1.

151 D. Aspnes and E. Palik, *Handbook of optical constants of solids*, Academic, New York, 1985.

152 P. Chen, Y. Bai and L. Wang, *Small Struct.*, 2021, **2**, 2000050.

153 N. Yaghoobi Nia, D. Saranin, A. L. Palma and A. Di Carlo, *Semicond. Sci. Technol.*, 2019, **34**, 163–228.

154 J. Werner, B. Niesen and C. Ballif, *Adv. Mater. Interfaces*, 2018, **5**, 1700731.

155 M. Ohring, *Materials Science of Thin Films: Deposition & Structure*, Elsevier, New Jersey, 2nd edn., 2006.

156 D. Kiermasch, L. Gil-Escrig, H. J. Bolink and K. Tvingstedt, *Joule*, 2019, **3**, 16–26.

157 W. Hu, W. Zhou, X. Lei, P. Zhou, M. Zhang, T. Chen, H. Zeng, J. Zhu, S. Dai, S. Yang and S. Yang, *Adv. Mater.*, 2019, **31**, 1806095.

158 G. Xiao, C. Shi, K. Lv, C. Ying and Y. Wang, *ACS Appl. Energy Mater.*, 2018, **1**, 2576–2581.

159 K. Wojciechowski, M. Saliba, T. Leijtens, A. Abate and H. J. Snaith, *Energy Environ. Sci.*, 2014, **7**, 1142–1147.

160 X. Xu, H. Zhang, J. Shi, J. Dong, Y. Luo, D. Li and Q. Meng, *J. Mater. Chem. A*, 2015, **3**, 19288–19293.

161 Y. Okamoto and Y. Suzuki, *J. Phys. Chem. C*, 2016, **120**, 13995–14000.

162 D. Wang, C. Wu, W. Luo, X. Guo, B. Qu, L. Xiao and Z. Chen, *ACS Appl. Energy Mater.*, 2018, **1**, 2215–2221.

163 H. Xie, X. Yin, J. Liu, Y. Guo, P. Chen, W. Que, G. Wang and B. Gao, *Appl. Surf. Sci.*, 2019, **464**, 700–707.

164 M. M. Lee, J. Teuscher, T. Miyasaka, T. N. Murakami and H. J. Snaith, *Science.*, 2012, **338**, 643–647.

165 P. Tiwana, P. Docampo, M. B. Johnston, H. J. Snaith and L. M. Herz, *ACS Nano*, 2011, **5**, 5158–5166.

166 X. Huang, Z. Hu, J. Xu, P. Wang, L. Wang, J. Zhang and Y. Zhu, *Sol. Energy Mater. Sol. Cells*, 2017, **164**, 87–92.

167 W. Nie, H. Tsai, R. Asadpour, J.-C. Blancon, A. J. Neukirch, G. Gupta, J. J. Crochet, M. Chhowalla, S. Tretiak, M. A. Alam, H.-L. Wang and A. D. Mohite, *Science*, 2015, **347**, 522–525.

168 S. Aharon, M. Layani, B.-E. Cohen, E. Shukrun, S. Magdassi and L. Etgar, *Adv. Mater.*, 2015, **2**, 1500118.

169 M. T. Hörantner, P. K. Nayak, S. Mukhopadhyay, K. Wojciechowski, C. Beck, D. McMeekin, B. Kamino, G. E. Eperon and H. J. Snaith, *Adv. Mater. Interfaces*, 2016, **3**, 1500837.

170 G. E. Eperon, V. M. Burlakov, A. Goriely and H. J. Snaith, *ACS Nano*, 2014, **8**, 591–598.

171 P. You, Z. Liu, Q. Tai, S. Liu and F. Yan, *Adv. Mater.*, 2015, **27**, 3632–3638.

172 S. Rahmany, M. Layani, S. Magdassi and L. Etgar, *Sustain. Energy Fuels*, 2017, **1**, 2120–2127.

173 L. Zhang, M. T. Hörantner, W. Zhang, Q. Yan and H. J. Snaith, *Sol. Energy Mater. Sol. Cells*, 2017, **160**, 193–202.

174 S. Aharon, M. Layani, B. El Cohen, E. Shukrun, S. Magdassi and L. Etgar, *Adv. Mater. Interfaces*, 2015, **2**, 1500118.

175 J. H. Lu, Y. L. Yu, S. R. Chuang, C. H. Yeh and C. P. Chen, *J. Phys. Chem. C*, 2016, **120**, 4233–4239.

176 Y. Guo, K. Shoyama, W. Sato and E. Nakamura, *Adv. Energy Mater.*, 2016, **6**, 1502317.

177 J. Zhao, K. O. Brinkmann, T. Hu, N. Pourdavoud, T. Becker, T. Gahlmann, R. Heiderhoff, A. Polywka, P. Görrn, Y. Chen, B. Cheng and T. Riedl, *Adv. Energy Mater.*, 2017, **7**, 1602599.

178 F. Guo, H. Azimi, Y. Hou, T. Przybilla, M. Hu, C. Bronnbauer, S. Langner, E. Spiecker, K. Forberich and C. J. Brabec, *Nanoscale*, 2015, **7**, 1642–1649.

179 J. W. Jung, C. C. Chueh and A. K. Y. Jen, *Adv. Energy Mater.*, 2015, **5**, 1500486.

180 K. T. Lee, J. Y. Jang, S. J. Park, S. A. Ok and H. J. Park, *Nanoscale*, 2017, **9**, 13983–13989.

181 M. B. Upama, M. A. Mahmud, H. Yi, N. K. Elumalai, G. Conibeer, D. Wang, C. Xu and A. Uddin, *Org. Electron.*, 2019, **65**, 401–411.

182 C. D. Bailie, M. G. Christoforo, J. P. Mailoa, A. R. Bowring, E. L. Unger, W. H. Nguyen, J. Burschka, N. Pellet, J. Z. Lee, M. Grätzel, R. Noufi, T. Buonassisi, A. Salleo and M. D. McGehee, *Energy Environ. Sci.*, 2015, **8**, 956–963.

183 F. Guo, H. Azimi, Y. Hou, T. Przybilla, M. Hu, C. Bronnbauer, S. Langner, E. Spiecker, K. Forberich and C. J. Brabec, *Nanoscale*, 2015, **7**, 1642–1649.

184 C. O. R. Quiroz, L. Levchuk, C. Bronnbauer, M. Salvador, K. Forberich, T. Heumueller, Y. Hou, P. Schweizer, E. Spiecker and C. J. Brabec, *J. Mater. Chem. a*, 2015, **3**, 24071–24081.

185 Y. (Michael) Yang, Q. Chen, Y.-T. Hsieh, T.-B. Song, N. De Marco, H. Zhou and Y. Yang, *ACS Nano*, 2015, **9**, 7714–7721.

186 E. Della Gaspera, Y. Peng, Q. Hou, L. Spiccia, U. Bach, J. J. Jasieniak and Y. B. Cheng, *Nano Energy*, 2015, **13**, 249–257.

187 T. Duong, N. Lal, D. Grant, D. Jacobs, P. Zheng, S. Rahman, H. Shen, M. Stocks, A. Blakers, K. Weber, T. P. White and K. R. Catchpole, *IEEE J. Photovoltaics*, 2016, **6**, 679–687.

188 F. Fu, T. Feurer, T. P. Weiss, S. Pisoni, E. Avancini, C. Andres, S. Buecheler and A. N. Tiwari, *Nat. Energy*, 2016, **2**, 16190.

189 S. Albrecht, M. Saliba, J. P. Correa Baena, F. Lang, L. Kegelmann, M. Mews, L. Steier, A. Abate, J. Rappich, L. Korte, R. Schlatmann, M. K. Nazeeruddin, A. Hagfeldt, M. Grätzel and B. Rech, *Energy Environ. Sci.*, 2016, **9**, 81–88.

190 A. Guerrero, J. You, C. Aranda, Y. S. Kang, G. Garcia-Belmonte, H. Zhou, J. Bisquert and Y. Yang, *ACS Nano*, 2016, **10**, 218–224.

191 Y. Kato, L. K. Ono, M. V. Lee, S. Wang, S. R. Raga and Y. Qi, *Adv. Mater. Interfaces*, 2015, **2**, 2–7.

192 L. Gao, E. Zhao, S. Yang, L. Wang, Y. Li, Y. Zhao and T. Ma, *Opt. Eng.*, 2017, **56**, 117107.

193 F. Fu, T. Feurer, T. Jäger, E. Avancini, B. Bissig, S. Yoon, S. Buecheler and A. N. Tiwari, *Nat. Commun.*, 2015, **6**, 1–9.

194 C. Hanmandlu, C. Y. Chen, K. M. Boopathi, H. W. Lin, C. S. Lai and C. W. Chu, *ACS Appl. Mater. Interfaces*, 2017, **9**, 32635–32642.

195 H. J. Chen, L. Wang and W. Y. Chiu, *Mater. Chem. Phys.*, 2007, **101**, 12–19.